60 GHz photonic millimeter-wave communication systems

Von der Fakultät für Ingenieurwissenschaften der Universität Duisburg-Essen Abteilung Elektrotechnik und Informationstechnik zur Erlangung des akademischen Grades eines

Doktors der Ingenieurwissenschaften

genehmigte Dissertation

von

Dipl.-Ing. Mario Weiß
aus
Regensburg

1. Gutachter: Prof. Dr. rer. nat. Dieter Jäger
2. Gutachter: Prof. Dr.-Ing. Klaus Solbach
Tag der mündlichen Prüfung: 22.04.2010

Abstract

Currently available copper-based Internet access technologies like xDSL and DOCSIS cover data transmission speeds in the range of some 10 Mb/s. With new applications, an increase in bandwidth demand up to the Gb/s-range is expected for the next years. Therefore, an evolution of access networks by gradual replacement of copper-based by fiber-optic infrastructure is presently ongoing. A similar development can be predicted for wireless access technology operating within the classical microwave range. Due to regulatory requirements and a lack of bandwidth alternatives need to be developed in the millimeter-wave band. In this regard, the frequency range around 60 GHz has a special importance due to a worldwide available unlicensed spectrum of several GHz of bandwidth. In this context, the integration of wireless networks in fiber-optic networks by the fiber-optic transport of the radio signal (radio-over-fiber, RoF) is of particular importance. Besides the low-loss optical transport of a 60 GHz radio signal RoF technology furthermore allows to shift complexity from base stations to a central office by a centralized provision of the millimeter-wave carrier.

This work deals with the modeling, realization and characterization of 60 GHz RoF systems providing data rates within the multi-Gb/s range. On the theoretical side, a system model has been developed comprising relevant electrical and optical noise sources and the transmission properties of fiber-optic and wireless links as well. This allows for instance to make reliable predictions of the expected system performance in the run-up to RoF system planning and thus to identify optimization potential.

Using innovative approaches and technologies, 12.5 Gb/s data transmission has been realized via fiber and wirelessly for the first time over technical relevant distances. Also, if compared to conventional RoF systems the dispersion-limited fiber-optic range has been multiplied. Another RoF system in the frame of this work aimed for an uncompressed HDTV transmission, for instance for video conferencing with high resolution (1080p) and extremely low latency (telemedicine). The wireless transmission of an uncompressed HDTV signal has been successfully demonstrated. Including the previously achieved results and experiences, the system complexity has been significantly reduced.

Acknowledgments

This thesis was written during my time as a research assistant at the Center for Semiconductor Technology and Optoelectronics at the University of Duisburg-Essen. The work was funded by the European Commission within the integrated project IPHOBAC under grant number 35317.

First and foremost, I would like to thank Professor Dieter Jäger and Dr. Andreas Stöhr for their continuous support and guidance and for the opportunity to work at the institute. Moreover, I thank Professor Klaus Solbach for acting as co-referee, for his interest in my work and for his suggestions.

I thank Dr. Benoît Charbonnier and Dr. Mathieu Huchard (both from France Télécom), as well as Dr. Frédérik van Dijk (Alcatel-Thales III-V Lab) for the intensive collaboration within the research project. I owe them a debt of gratitude for always being helpful with technical questions and for many scientific discussions. Further on, I acknowledge Paul Lehmann for his strong support in technical matters.

I would like to thank all employees at the institute who contributed to a good atmosphere and for their cooperativeness. Especially, I would like to point out the engagement of Sebastian Babiel, Dr. Rüdiger Buß, Sascha Fedderwitz and Vitaly Rymanov for proofreading parts of the thesis. Further on, I acknowledge Karin Tempel for her strong organizational help, as well as Melanie Wachholz and Heinz Slomka for their help in technical matters.

Finally, I would like to express my sincere thanks to my parents and my brother for their support, patience and understanding during my dissertation.

Duisburg, June 2010 Mario Weiß

Contents

List of Figures

List of Tables

List of Acronyms

Mathematical Symbols

$B_{N,el}$	Noise-equivalent bandwidth
dB	Decibels
dBc	Decibels, relative to carrier
dBi	Decibels, isotropic
dBm	Decibels, milliwatt
DC	Direct current
D	Dispersion parameter
$DIPP_{DSB}$	DSB dispersion induced power penalty
$DIPP_{DSB,CS}$	DSB-CS dispersion induced power penalty
d_f	Fraunhofer distance
erf(z)	Gaussian error function
erfc(z)	Gaussian error function, complementary notation
E	Electrical field strength
E_B	Energy per bit
f_0	Center frequency
f_{IF}	Intermediate frequency
f_{LO}	Local oscillator frequency
f_{ML}	Mode-locking frequency
f_{RF}	Radio frequency
G_{el}	Electrical gain
G_{opt}	Optical gain
IL	Insertion loss
I_0	Static injection current
I_{ph}	Photocurrent, average
$i_{ph}(t)$	Photocurrent, general
$i_{ph,RF}(t)$	Photocurrent, RF

L	Length
L_{fs}	Free-space path loss
L_{gas}	Attenuation induced by atmospheric gases
L_{rain}	Attenuation induced by rain fall
L_{path}	Total path loss
n	Refractive index
N_0	Noise power spectral density
N_{el}	Electrical noise power
NF_{el}	Electrical noise figure
NF_{opt}	Optical noise figure
P_{el}	Electrical power
P_{opt}	Optical power
PSD_{NRZ}	Power spectral density of an NRZ-signal
R_{bit}	Bit rate
$R(f)$	Frequency response coefficient
S	Dispersion slope
SNR	Signal-to-noise ratio
T	Temperature
T_0	Reference temperature
T_B	Bit period
T_{EAM}	Electro-optic transfer function of an EAM
T_{MZM}	Electro-optic transfer function of an MZM
V_π	Half-wave voltage of an MZM, general
$V_{\pi,DC}$	Half-wave voltage of an MZM, DC-electrode
$V_{\pi,RF}$	Half-wave voltage of an MZM, RF-electrode
v_g	Group velocity
V_q	Quadrature voltage
Z_{in}	Input impedance
Z_{out}	Output impedance
Z_{ref}	Reference impedance
α	Optical fiber attenuation coefficient
$\alpha(V)$	Voltage-dependent attenuation coefficient
β_p	Propagation constant
β_n	Dispersion parameter of n-th order
β_L	Propagation constant, linear part
γ	Optical confinement factor
$\Delta\omega$	Angular frequency difference

$\Delta\phi$	Phase difference
$\Delta\phi_{int}$	Intrinsic phase difference
η	Quantum efficiency of a photodetector
$\eta_{EO,RF}$	Electro-optic conversion coefficient, slope efficiency
$\eta_{OE,ref}$	Opto-electronic conv. coefficient, ideal responsivity
$\eta_{OE,DC}$	Opto-electronic conv. coefficient, DC-responsivity
$\eta_{OE,RF}$	Opto-electronic conv. coefficient, RF-responsivity
λ	Wavelength
ρ_{sp}	Spontaneous power density
ϕ	Phase
ω	Angular frequency
ω_0	Angular center frequency

Constants

c	Speed of light in vacuum
e	Electron charge
h	Planck constant
k_B	Boltzmann constant

Abbreviations

1 GbE	1 Gb/s Ethernet
10 GbE	10 Gb/s Ethernet
ASE	Amplified spontaneous emission
ASK	Amplitude shift keying
ATM	Asynchronous transfer mode
AWGN	Additive white Gaussian noise
BER	Bit error rate
BBOF	Baseband-over-fiber
BS	Base station
BTB	Back-to-back
CD	Chromatic dispersion
CO	Central office
CW	Continuous wave
DCF	Dispersion compensating fiber
DOCSIS	Data over cable service interface specification

DSF	Dispersion shifted fiber
DSL	Digital subscriber line
DIPP	Dispersion-induced power penalty
DSB	Double sideband
DSB-CS	Double sideband with carrier suppression
DWDM	Dense wavelength division multiplexing
EDC	Electronic dispersion compensation
EML	External modulation
EIRP	Equivalent isotropic radiated power
ER	Extinction ratio
FEC	Forward error correction
FTTB	Fiber-to-the-building
FTTH	Fiber-to-the-home
FTTN	Fiber-to-the-neighborhood
FTTP	Fiber-to-the-premises
HDMI	High definition multimedia interface
HD-SDI	High definition serial data interface
HDTV	High definition television
LAN	Local area network
LOS	Line-of-sight
LTE	Long-term evolution
MAN	Metropolitan area network
MATP	Maximum transmission point
MIMO	Multiple-input multiple-output
MITP	Minimum transmission point
NRZ	Non return to zero
OFDM	Orthogonal frequency division multiplexing
OOK	On-off-keying
OPLL	Optical phase-locked loop
P2MP	Point to multi point
P2P	Point to point
PLL	Phase-locked loop
PON	Passive optical network
PSD	Power spectral density
PSK	Phase shift keying
PRBS	Pseudo-random binary sequence
QAM	Quadrature amplitude modulation

QP	Quadrature point
QPSK	Quadrature phase shift keying
RIN	Relative intensity noise
RoF	Radio-over-fiber
SMF	Single mode fiber
SSB	Single sideband
V-band	Frequency range of 50–75 GHz
WAN	Wide area networks
WiFi	Wireless fidelity
WIMAX	Worldwide interoperability for microwave access
WLAN	Wireless local area network
WPAN	Wireless personal area network

1 Introduction

1.1 Demand for broadband access

The worldwide demand for communication is growing with tremendous rates, and no end of this progress is in sight. A key element was the development

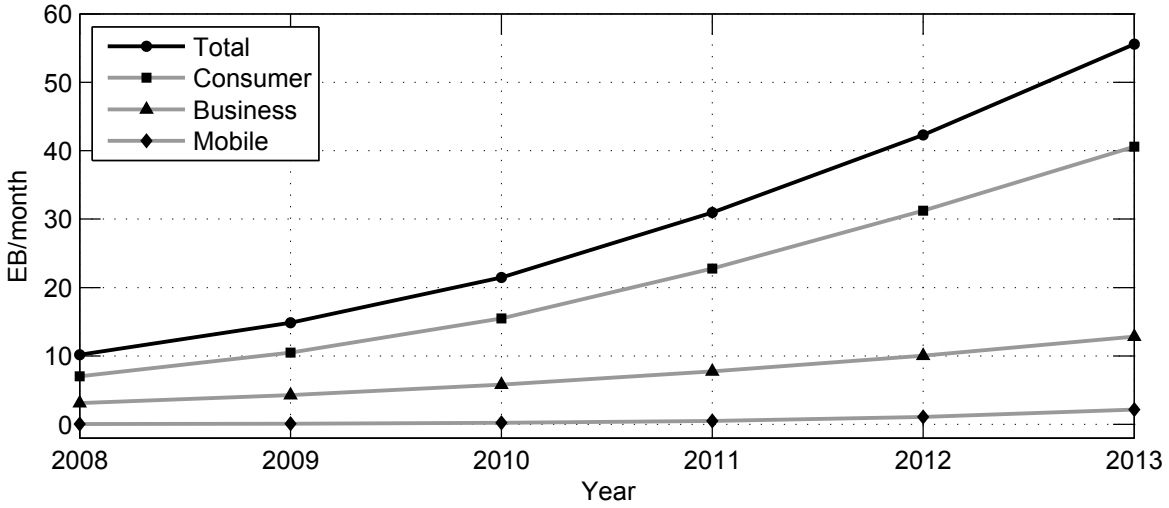

Figure 1.1: Global IP traffic growth within 2008–2013.

of the Internet, and during the years 2000–2009 the worldwide growth rate

of internet users was about 380 %. In 2009, the penetration of internet users within the population was as high as 52 and 74 % in Europe and North America, respectively [1]. Due to an increasing number of users and to the development of new "bandwidth-hungry" applications like peer-to-peer communication or video-over-IP, the global IP traffic is expected to rise from about 14 exabyte (EB, 10^{18} byte) per month in 2009 to more than 55 EB per month in 2013 [2]. The total estimated IP traffic by segment is exemplified in **Fig. 1.1**. The highest contingent is expected to be caused by consumers, comprising fixed IP traffic generated by households, university populations and internet cafés. Second segment is business IP traffic, i.e. fixed IP traffic within wide area networks (WANs) or internet traffic, generated by businesses as well as governments. The mobile segment includes mobile data and internet traffic caused by wireless cards for portable computers, wireless local area network (WLAN) hotspots and handset-based mobile Internet usage. An annual growth rate of about 131 % is expected here, compared to 42 % within the consumer field and 32 % in the business field, respectively.

In response to this expected need, metro as well as core networks of infrastructure providers have continuously been upgraded with respect to bandwidth. Typically, data rates per fiber channel within core networks are 10 Gb/s. Furthermore, an extension to 40 Gb/s is ongoing and even data rates of 100 Gb/s are under discussion and standardization [3]. Also, metro networks have been massively upgraded to meet the rising bandwidth demand, and component manufacturers are currently working on integrated low-cost solutions for the mass market [4, 5].

For the last mile, several mature technologies are currently in use to deliver a service to the destination access node, allowing Internet access as well as triple-play services (see **Fig. 1.2**). Currently, customer's access to high-speed networking is still predominated by copper-based technologies with a very limited bandwidth with respect to future communication demands. To overcome this future bottleneck, endeavors are ongoing to replace copper-based infrastructure with fibers in order to meet the rising requirements. For the future, fully fiber-based access is expected, from currently fiber-to-the-neighborhood (FTTN) over fiber-to-the-building (FTTB) to finally fiber-to-the-home (FTTH) while applying a step-by-step replacement of existing copper-based infrastructure by fibers [6]. On the other side, installing new fibers can be very expensive in metro areas with costs of up to 250,000 $

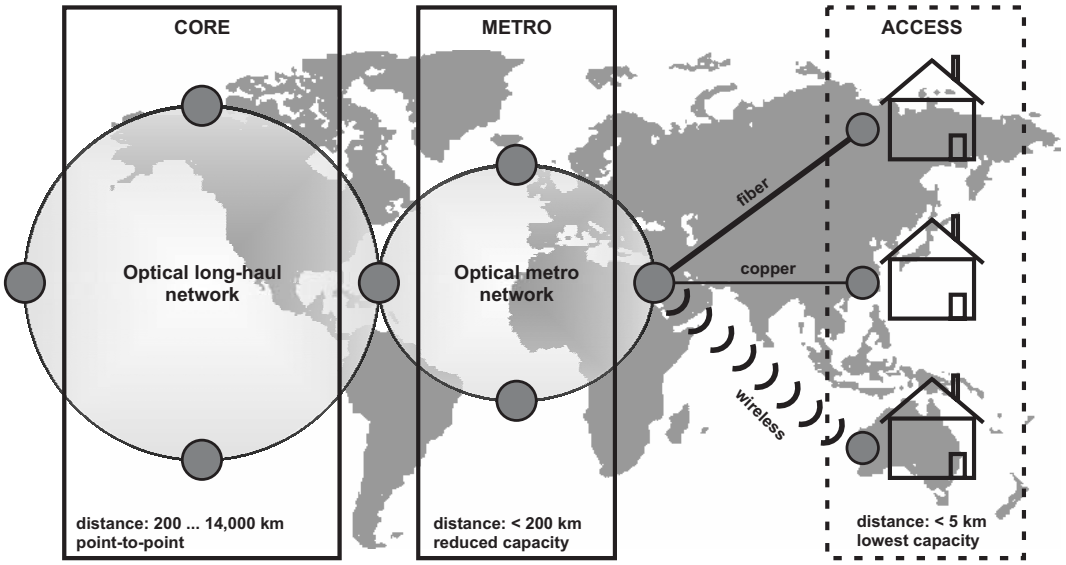

Figure 1.2: Classification of networks [5].

per mile [7]. In this case, wireless access could be an appropriate option, but currently available wireless technologies operate at data rates which are orders of magnitude lower than transmission speeds offered by fiber access.

This limitation is induced by a lack of bandwidth in conventional microwave-bands due to regulatory constraints and frequency congestion as well [8]. Alternatives need to be developed operating in the millimeter-wave band where more bandwidth is available. The frequency range around 60 GHz is here especially important due to a worldwide available unlicensed spectrum of several GHz of bandwidth. In conjunction with fiber-optic transmission, new standards and technologies are expected for the future, leading to photonic millimeter-wave technologies and transmission systems which are subject in this thesis.

1.2 Copper-based access technologies

The two dominant access technologies are digital subscriber line (DSL) utilizing twisted-pair infrastructure from telephone companies and the data over cable service interface specification (DOCSIS) based upon the networks of cable TV companies. Since 1999, different DSL standards have been developed and enhanced up to now. Besides symmetric DSL (SDSL) for

business customers [9], private customers on the other side have been considered to require more asymmetric connectivity (ADSL). The most widespread standard here is ADSL2+ which allows maximum down- and upstreams of 24 and 3.5 Mb/s, respectively [10]. Its successor is denoted as very high speed DSL (VDSL), allowing symmetrical up- and downstreams of up to 100 Mb/s by applying more efficient modulation techniques and by extending the consumed bandwidth of the copper infrastructure.

The main competitors of DSL service providers are cable TV companies with coaxial cables offering higher bandwidths and reduced losses compared to twisted pair infrastructure. Currently, DOCSIS3 supports down- and upstreams of 304 and 108 Mb/s which are, however, shared between many users [11]. For both DSL and DOCSIS, the mentioned data rates must be interpreted as theoretical maximum if excellent infrastructure is given. In addition, providers modify frequency allocations to support e.g. higher downstream but reduced upstream rates. As an example, currently available VDSL connections from Deutsche Telekom AG in Germany allow maximum down- and upstreams of 50 and 5 Mb/s [12]. With rising demand in terms of data rate, more bandwidth and sophisticated modulation techniques have been implemented in the corresponding standards. As the copper infrastructure remained the same, the transport range was reduced accordingly. In consequence, existing copper infrastructure was more and more replaced by fibers, thus the so-called last mile has been reduced to some 100 meters nowadays in densely populated areas. Future rising bandwidth demands let therefore predict an overall replacement of copper-based installation with fibers to FTTH infrastructures.

1.3 Fiber access

The two main topologies for FTTH infrastructures are point to multi point (P2MP) utilizing passive optical network (PON) technology, and point to point (P2P) mainly applying Ethernet technology [13]. For the case of P2MP, the main idea of a PON is to realize a network by passive optical components where signal distribution is achieved by passive optical splitters to each customer premises, starting with a single fiber at the central office (CO) which is shared and split among typically 64 customers. As a consequence,

no electrical power connection and only reduced maintenance is required. PONs in Europe are typically operated as Gigabit PON (GPON), allowing up- and downstreams of about 1.25 and 2.5 Gb/s, respectively [14]. GPON supports mixed traffic modes with different packet lengths and asynchronous transfer mode (ATM), among other benefits like centralized administration and maintenance. An alternative is the Ethernet PON (EPON) standard, supplying Ethernet-compatible framing with symmetric up- and downstreams of 1.25 Gb/s [15]. One aim of EPON is to combine the low costs of Ethernet technology with the comparatively low costs of a PON. Currently, work is also ongoing to specify and to standardize 10 Gb/s EPON for future broadband access networks [16, 17]. This is different for the case of P2P topology. Here, each subscriber is supplied with a dedicated fiber to a first aggregation point in the network. As transport technology, typically fast Ethernet supporting 100 Mb/s and 1 Gigabit Ethernet is utilized.

First FTTH field trials have already been accomplished in the year 1977 in Japan, supporting 168 customers with fiber access, and many years of research in conjunction with several field trials have been carried out [18]. However, costs were simply too high to enter mass market in the past, mainly due to the costs of the new technology at that time, as well as due to a lack of optoelectronic components in large amounts [19]. With the development of

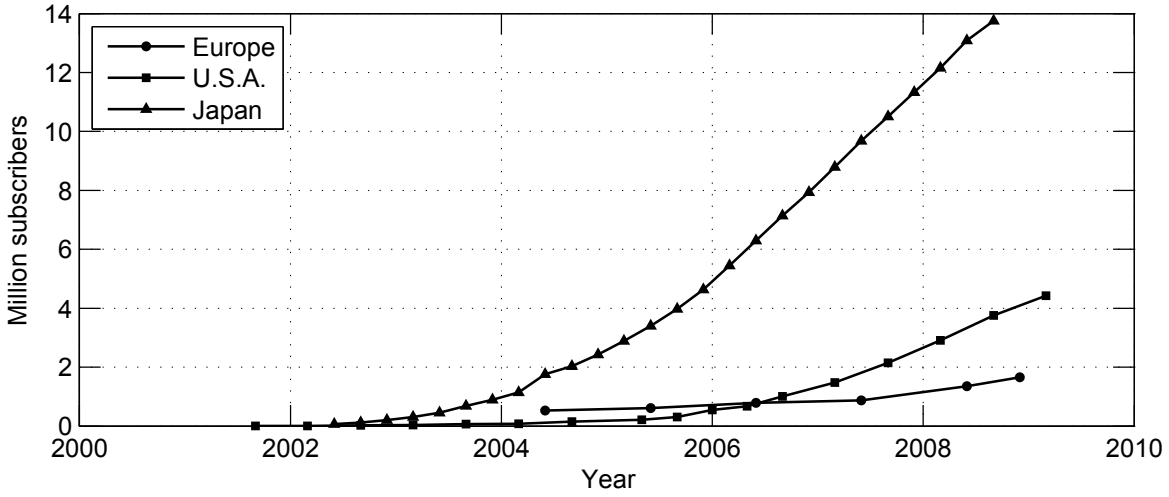

Figure 1.3: FTTH subscribers in Europe, U.S.A. and Japan.

low-cost optoelectronic components, like standardized transceivers for optical networks in conjunction with rising bandwidth demand, FTTH became more

and more attractive for infrastructure providers. For instance, Japan has started very early with FTTH pilot projects in 2002, aiming for about 3.5 million FTTH customers in the year 2006 [20]. In the end of 2008, the number of FTTH subscribers was as high as about 14 millions, exceeding the number of DSL subscribers for the first time [21]. On the contrary, the total number of FTTH/FTTB subscribers was only about 1.7 million within the whole European Union at the same time [22, 23]. The development of subscribers in Europe, Japan and the United States is shown in **Fig. 1.3**.

1.4 Wireless access

While access technologies are typically based upon wired technologies, broadband wireless technologies offer ubiquitous access to a user with no need for a wired access point. Different standards have been developed up to now, supporting various applications for fixed, nomadic and mobile access [7, 24].

Wireless Fidelity (WiFi) technology is deployed for short-range applications within home and business local area networks (WLAN), as well as for hotspot connectivity. The most prominent standard here is IEEE 802.11g, offering theoretical data transmission rates of up to 54 Mb/s per access point [25]. A recent upgrade, 802.11n, even supports transmission rates of 600 Mb/s, for instance by utilizing multiple-input multiple-output (MIMO) techniques [26]. However, the achievable transmission rate in practice is much lower, depending on distance and environment. Considering further the number of users sharing the capacity of the access point and the bandwidth of the access point connection, typical data rates per user within commercial hotspots are about 1–2 Mb/s [7].

The term fourth generation (4G) technology denotes recent approaches in wireless transmission with long-term evolution (LTE) technologies, as well as worldwide interoperability for microwave access (WIMAX) technology. LTE is provided as a substitute of existing 2G (GSM) and 3G (UMTS) technology with targeted theoretical data rates of up to 100 Mb/s. Standardization on LTE technology is currently under way. The main representative for WIMAX technology is IEEE 802.16, supporting fixed and mobile connectivity as well [27]. Similar standards have been launched by the ETSI, like HiperAccess [28] and HiperMAN [29]. Although theoretical data rates of several tens of

Mb/s have been standardized, currently available WIMAX-based networks are supporting around 2–4 Mb/s [7].

Wireless transmission within 6–38 GHz is often denoted as microwave radio [30], supporting fixed wireless point-to-point connectivity. Typical data transmission rates of commercial microwave links are 100 or 155 Mb/s. Application fields comprise campus connectivity or mobile backhauling, which will be discussed in **1.5**. Reason for not offering faster transmission speeds is given by a strict regulation of the microwave band and frequency congestion as well. As an example, allocated channel bandwidths depending on frequency and regulator in Europe are 28 MHz and sometimes 56 MHz whereas a maximum value of 50 MHz is given within the United States. In conjunction with economically reasonable modulation techniques, maximum data rate is limited to around 400 Mb/s [30].

A solution to this bottleneck is seen in the development of wireless systems operating at much higher carrier frequencies, namely in the millimeter-wave (mm-wave) range where more bandwidth is available. Especially around 60 GHz, a huge amount of bandwidth is allocated for unlicensed operation which will be detailed in **2.4**. Although regulations vary strongly by country and region, developments are in progress for a worldwide harmonized frequency band around 57–64 GHz. Main drawback of 60 GHz technology is a peaking atmospheric gaseous attenuation which clearly limits wireless path lengths. Alternative spectra with reduced atmospheric attenuation are located in the E-band, like 71–76 and 81–86 GHz, respectively. Nevertheless, the potential of 60 GHz for medium-range broadband wireless transmission has not been fully exploited yet. However, the rising interest in 60 GHz technology also induced by future broadband wireless personal area network (WPAN) solutions has already led to higher component availability and lower component cost. Also, future 60 GHz RF-CMOS technology predicts further cost reduction. Consequently, some companies are already offering first wireless millimeter-wave links operating within a range of 57–64, 71–76, or 81–86 GHz, supporting data rates of up to 1.25 Gb/s for 1 Gb/s Ethernet [31–37]. Most of the offered systems are equipped with high-gain antennas to allow wireless transmission of some 100 m. The transceivers of such links are either equipped with copper or fiber interface to be used directly within an Ethernet. Up- and downconversion are both performed electronically. An overview of the discussed technologies for wireless access

is given in **Tab. 1.1**, summarizing some important key parameters [7]. The indicated wireless distances are related to carrier class performance.

Table 1.1: Key parameters of important wireless access technologies.

Technology	Data rate	Distance	Bandwidth / licensing
WiFi	1–2 Mb/s	20 m	Free availability for unlicensed usage
4G	5–10 Mb/s	3 km	Very low bandwidth and strict regulation, licensed
Microwave	$\leq$ 400 Mb/s	5 km	Low bandwidth, strongly varying by country, difficult regulation, licensed
60 GHz	$\gg$ 1 Gb/s	400 m	Very high bandwidth, varying by country and region, unlicensed usage
70 & 80 GHz	$\gg$ 1 Gb/s	3 km	Very high bandwidth, worldwide availability, light license

1.5 Application scenarios for broadband fiber-wireless systems

Various application scenarios come along with an increased demand for broadband communication as shown in **Fig. 1.4**.

A first important scenario is given in **Fig. 1.4a** where a private household or an office is connected via fiber. The further signal distribution may be realized using a passive optical network with no use of any additional active components like optical amplifiers. Due to the high absorption of materials like concrete, wood or hard plaster, each individual room needs to be supplied with a wireless front-end to realize a WPAN. First prototypes addressing this scenario have already been realized within the research project [O16] discussed further in **1.6**.

Another major scenario is wireless corporate access or campus connectivity as shown in **Fig. 1.4b**. A prerequisite for this is that at least one building

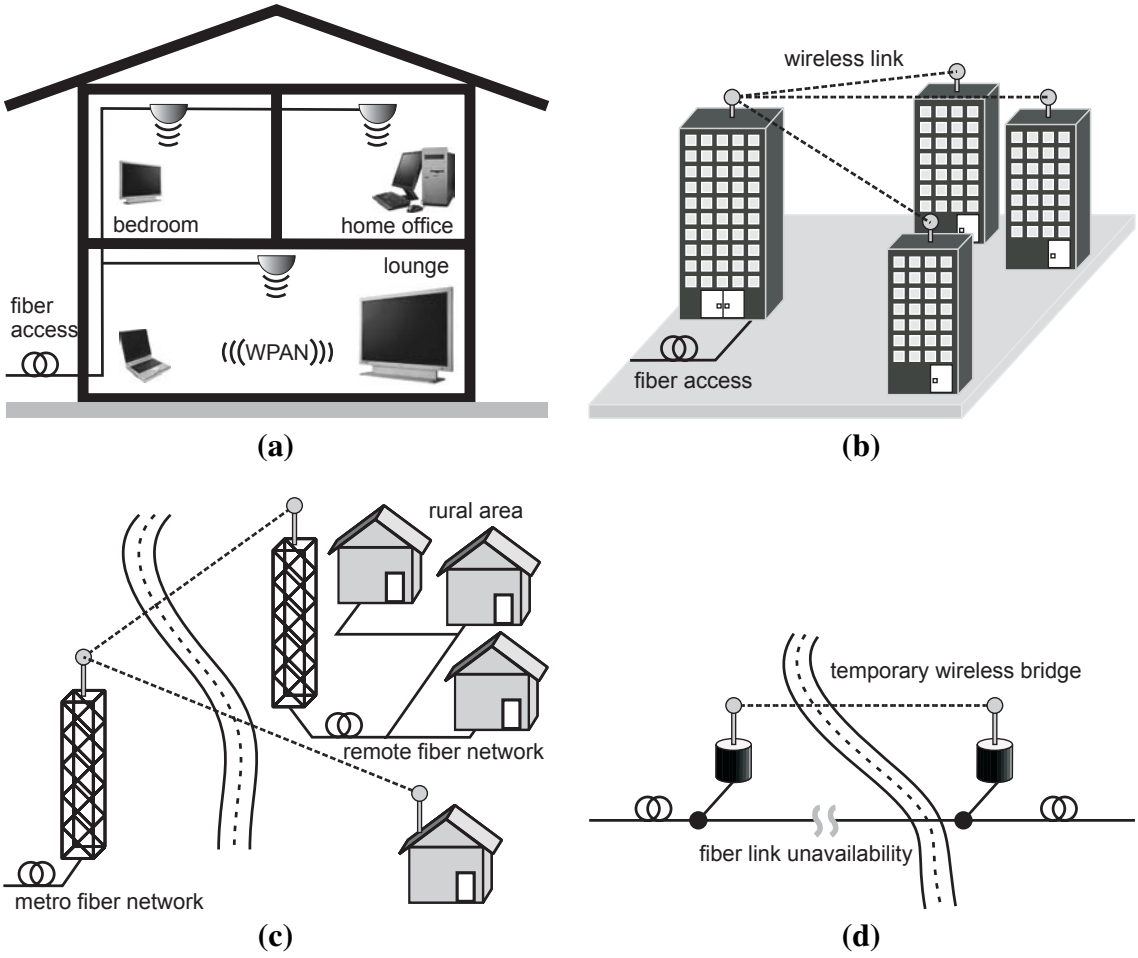

Figure 1.4: Application scenarios for photonic millimeter-wave communication.

is already equipped with fiber access. If additional buildings are erected on an existing campus or if buildings are separated by road, rail or river wired solutions may be very expensive to install. Laying new cables may be uneconomical, especially if a link is only required for a limited period of time.

Broadband wired access – now by DSL or TV cable and in the future by fiber – is mostly very economical within densely populated areas. However, within rural areas access speeds are limited to fractions as companies are not bound to offer broadband services everywhere since the replacement of the existing wired infrastructure is very costly. The scenario shown in **Fig. 1.4c** illustrates the case where a rural area is cut off from a high-speed metropolitan network. Depending on the number of households, the remote

location could be equipped with a local fiber-optic network fed by a central wireless transceiver and the last mile bridged wirelessly.

Construction work, flooding, earthquakes or other disturbances can cause unavailability of service within metro access networks, thus leading to high costs for the service provider, especially if business customers are affected. The intermittently installation of a wireless bridge often denoted as disaster recovery could quickly restore connectivity while technical personnel are repairing damaged fibers (see **Fig. 1.4d**). This is also of interest for standard maintenance work if no wired redundancy is available.

Mobile backhauling can be mentioned as a practical example, denoting the wireless connectivity of mobile base stations. In the past, GSM base stations have been connected by copper-infrastructure which was sufficient for voice and slow data services. Meanwhile, due to the migration from 2G to 3G technology with higher demands on bandwidth, infrastructure providers needed to upgrade their networks. In cases where fiber-based connectivity is too cost-intensive, microwave-based wireless solutions have been installed to support mobile base stations with sufficient data transmission speeds [38].

With future rising bandwidth demand, current commercially available wireless transmission technologies will not be capable to support sufficient data transmission speeds. Considering for example the case of disaster recovery and a required data rate of 10 Gb/s, millimeter-wave radios would be a practical solution.

1.6 The research project

The presented work is part of the IPHOBAC project (Integrated Photonic Millimeter-Wave Functions For Broadband Connectivity) which is funded by the European Commission under grant number 35317 during the period 06/2006–11/2009 [39]. The project is coordinated by Universität Duisburg-Essen and comprises eleven industrial and scientific European partners.

The aims of IPHOBAC are to develop photonic components, integrated functions and systems for millimeter-wave applications in the field of communications, instrumentation and security, which is shown in **Fig. 1.5** [O30]. Optical sources under development are quantum-dot mode-locked laser diodes

(MLLD) with locking frequencies around 60 GHz, as well as dual-mode distributed feedback and distributed Bragg reflector lasers (DFB / DBR) with tuning ranges of 30–300 GHz. For broadband optical modulation, IPHOBAC

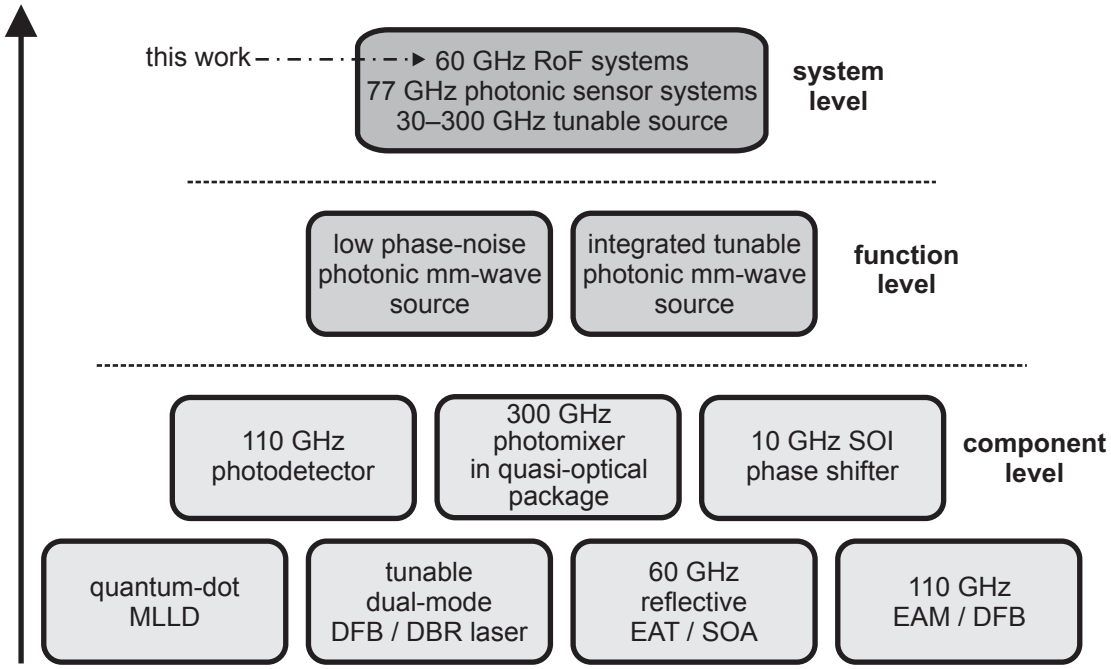

Figure 1.5: Technical objectives of the IPHOBAC project on component, function and system level.

further develops reflective 60 GHz electro-absorption transceivers (R-EAT) with integrated semiconductor optical amplifiers (SOA) and 110 GHz electro-absorption modulators (EAM) with integrated DFB lasers. On the detector side, 110 GHz photodetectors with coaxial output, as well as 30–300 GHz photodetectors with integrated quasi-optics are under research. The latter one allows a direct coupling of the converted optical mm-wave signal to free-space, e.g. for communication or sensing applications [O3, O16, O22, O24, O28].

Based upon the advances on component level, innovative photonic mm-wave functions are further developed within the project, like generating high-power mm-wave signals with low phase noise by optical means. Among photonic sensor systems and a fully-tunable 30–300 GHz source, another research aim on system level are 60 GHz radio-over-fiber (RoF) systems, which will be reported in this work. A general objective is to develop RoF systems with data rates of 1 Gb/s and above for future broadband fiber-wireless applications, utilizing advanced photonic components developed within IPHOBAC.

1.7 Organization and aims of the thesis

Basic concepts for photonic millimeter-wave related communication will be reported in **2**. Here, the concept of RoF is introduced and discussed. As the RF frequency in this work is located around 60 GHz, appropriate methods for optical mm-wave generation will be further discussed in this section, followed by optical modulation formats and methods for broadband optical data modulation. Unlike fiber-optic transmission with comparably low requirements on spectral efficiency, available spectrum around 60 GHz is limited to some GHz bandwidth (depending on the regulatory authority in a country), which will be furthermore discussed. Recent results on RoF related research activities will be summarized to a state-of-the-art especially aiming for high data transmission rate systems with speeds of 1 Gb/s and more.

In this thesis, different RoF systems have been studied and will be presented in chapters **5**–**7**. For developing a model to theoretically describe and analyze all the realized RoF systems, each system was divided into generic subsystems that can be found in each of the realized RoF systems such as photonic up-conversion, optical data modulation, photonic-wireless transmission as well as radio reception.

Those subsystems will be described, experimentally characterized and modeled in **3** in order to achieve a full system modeling for a theoretical study, as well as to optimize the system performance of the realized RoF systems. The chapter starts with the utilized photonic mm-wave generators, followed by subsystems for broadband photonic data modulation. In a next step, the fiber-optic channel with its impairments will be analyzed and considered. After fiber-optic transmission, the signal is converted back to electrical domain, amplified and transmitted in a wireless RoF transmitter. Besides the o/e-converted signal, several unwanted noise contributions are converted as well, whose influence will be considered accordingly. The wireless 60 GHz channel with its impairments and spectral attenuation properties will be further studied and modeled. The chapter is concluded with the applied wireless receiver architectures.

Based upon these theoretical and experimental results, a Matlab®-based simulation model will be developed in **4**, comprising optical and electrical noise sources besides the signal power to calculate signal and noise powers,

and thus the signal-to-noise ratio (SNR) of the realized RoF systems. A consideration of the applied digital modulation scheme and the error statistics of the utilized receiver architectures allows to predict the received SNR of the developed RoF systems in **5**–**7**.

A first experimental RoF system based upon external photonic millimeter-wave generation and a coherent wireless receiver architecture will be presented in **5**, aiming for data rates of up to 12.5 Gb/s to support the required gross data rate for 10 GbE. Such transmission rates are in the first place required for future broadband point-to-point access links or bridges.

For application cases with lower demand on data rate, like for in-house communication, a second system will be realized, based upon an incoherent receiver architecture allowing reduced complexity in **6**.

A third system in **7** applies a passively mode-locked laser diode for photonic millimeter-wave generation, which was developed within IPHOBAC. In conjunction with an incoherent wireless receiver, the system complexity is extremely low. This system is especially targeting at uncompressed photonic-wireless HDTV transmission, applicable for high-resolution video conferences or live broadcasting with low latency.

The thesis will be concluded with **8**, giving a summary of this work's results as well as an outlook.

2

60 GHz radio-over-fiber concepts and technologies

The general objective of this thesis was the development of ultra-broadband wireless systems with record capacities using RoF techniques. This chapter will at first introduce the general concept and properties of RoF in **2.1**. Various methods and techniques that have been reported in the literature previously for specific functions required in those RoF systems such as photonic millimeter-wave generation are discussed in **2.2**. A detailed exemplification will be accomplished to identify those methods used further in this thesis. For some functions, new concepts such as cascaded RF and data modulation have been developed to achieve ultra-high capacity. Those new concepts will be detailed in the sections **5**–**7**. In **2.3**, broadband photonic data transmission standards and protocols are discussed to deduce the requirements for the system demonstrations with respect to data rate and modulation technique. Compared to fiber-optic transmission systems with low demands on spectral efficiency, the available bandwidth for wireless transmission around 60 GHz – although much larger than for microwaves – is still rather limited. This is discussed in **2.4**. Recent results within the field of RoF systems especially discussing advances in data transmission rates are summarized to a state-of-the-art in **2.5**.

2.1 Concept of radio-over-fiber

For future broadband wireless communication, a key requirement is a reduced cell size thus a decreased number of participating users to increase the maximum available throughput per user. Further on, an extension of the carrier frequency to the mm-wave range is needed to achieve higher wireless data transmission rates while considering spectral regulation issues [40]. A

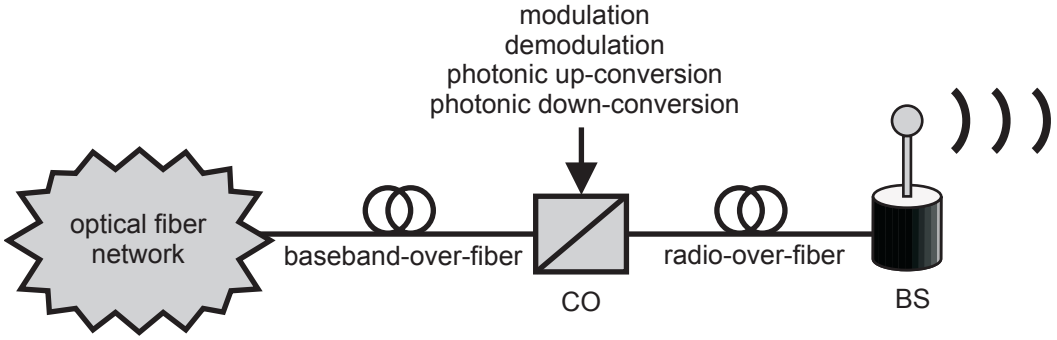

Figure 2.1: Concept of radio-over-fiber.

direct consequence is a high number of base stations (BS) which should be as cost-effective and simple as possible and which has to carry out central functions like signal routing & processing or frequency allocation at a central office (CO). Accordingly, by using optical fibers instead of copper, the maximum transmission range at a given data rate could be drastically extended. Appropriate techniques and approaches allow sharing equipment parts of the control station between a number of base stations. In addition, an RF carrier can be modulated on the optical carrier to distribute a radio signal instead of a baseband signal to each base station, which is denoted as radio-over-fiber, allowing for a complexity reduction within each base station, shown schematically in **Fig. 2.1**.

Typical advantages of such RoF approaches are for example an improved system reliability due to the simplified base station structure, allowing as well a simplified maintenance. However, transmitting radio signals over fiber instead of baseband data reduces the fiber-optic range due to dispersion effects, which will be discussed later in this work. The main objectives of a base station are limited to o/e- and e/o-conversion and signal amplification whereas tasks like frequency allocation, modulation and demodulation are performed within the central station [41].

2.2 Photonic mm-wave generation

Various applications such as radar, wireless communication, remote sensing or measuring technique require mm-wave signals with low phase noise and frequency tunability. This can be achieved in a conventional, purely-electronic way, thus requiring e.g. many stages of frequency multiplication, or by means of photonic mm-wave generation. Numerous papers have been published within this research field of optical microwave- and millimeter-wave generation previously, and especially the idea of transmitting radio signals over fiber for optical-wireless communication applications requires an appropriate method with sufficiently low noise and phase-noise, frequency stability as well as partial frequency tunability among other parameters [42, 43]. A detailed exemplification will be accomplished to identify appropriate methods and techniques used further in this thesis.

2.2.1 Dual laser sources

A comparatively simple approach is to couple two free running laser sources together with an optical coupler and to apply the dual-wavelength signal to a photodetector which is shown in **Fig. 2.2a**. If one of the lasers can be tuned in its wavelength, both optical modes can be adjusted in a way to generate a difference frequency of Δf. This signal is coupled to a photodetector and detected. Assuming a sufficiently high bandwidth of the photodetector, frequencies and tunabilities of 10 THz and above can be achieved. However, this method of optical heterodyning suffers from poor frequency stability and large phase noise for most application cases [42]. As an example, a frequency stability of about 10 MHz/hour and a phase noise level of −75 dBc/Hz at an offset level of 100 MHz was achieved while applying two DFB lasers [44]. An explanation of this method is e.g. given by [43], starting with the description of both optical laser sources:

$$E_1(t) = E_{01}\cos(\omega_1 t + \phi_1) \tag{2.1}$$

$$E_2(t) = E_{02}\cos(\omega_2 t + \phi_2) \tag{2.2}$$

$$E_{tot}(t) = E_1(t) + E_2(t) \tag{2.3}$$

with two optical waves $E_1(t)$ and $E_2(t)$ which are represented by their amplitudes E_{01} and E_{02}, their angular frequencies ω_1 and ω_2 and their phase terms

ϕ_1 and ϕ_2. Coupling both terms together results in $E_{tot}(t)$. Considering the dependency between photocurrent $i_{ph}(t)$ and $|E_{tot}(t)|^2$, neglecting the phase information for simplification and applying some transformation, the intensity is described as [43, 45]:

$$\begin{aligned} |E_{tot}(t)|^2 &= \frac{1}{2}E_{01}^2\left[1+\cos(2\omega_1 t)\right] + \frac{1}{2}E_{02}^2\left[1+\cos(2\omega_2 t)\right] + \\ &+ E_{01}E_{02}\left\{\left[\cos(\omega_1+\omega_2)t\right] + \left[\cos(\omega_1-\omega_2)t\right]\right\}. \end{aligned} \tag{2.4}$$

Assuming that the cut-off frequency of the photodetector is much lower than ω_1 and ω_2, solely a corresponding average power is o/e-converted. The incident total power to the photodetector can therefore be described as

$$P_{tot}(t) = P_{01} + P_{02} + 2\sqrt{P_{01}P_{02}}\cos\left[(\omega_1-\omega_2)t\right]. \tag{2.5}$$

Assuming further common polarization states and a photodetector with a responsivity of R, the generated photocurrent $i_{ph}(t)$ is finally described as [45, 46] [O5]

$$i_{ph}(t) = R\left\{P_{01} + P_{02} + 2\sqrt{P_{01}P_{02}}\cos\left[(\omega_1-\omega_2)t\right]\right\}. \tag{2.6}$$

Besides a sufficient tunability of one of the laser sources, the maximum achievable frequency is solely limited by the bandwidth of the photodetector here. A way to improve the mentioned limitations with respect to frequency stability as well as phase noise is to use an integrated dual-laser source. Although independent, the two modes exhibit an improved correlation as they both use the same cavity on a chip [43]. A recent result using a twin DBR laser, here in conjunction with optical injection locking, exhibited a phase noise level of −72 dBc/Hz at an offset frequency of 100 kHz [47].

2.2.2 Optical phase-locked loop

For applications with demands on low phase noise levels within the field of communication using e.g. modulation techniques with multi-phase levels, but especially millimeter-wave radar systems, the phases of both modes need to be locked together. This can be done by extending the previously discussed option of two free-running lasers with an optical phase locked loop (OPLL). Phase coherence is realized by actively locking the phase of one laser to the

phase of the other laser. A typical OPLL is shown in **Fig. 2.2b**. Here, the phase of the beat signal and the phase of a reference RF source are compared in a mixer acting as a phase detector. Together with an amplifier and a low-pass filter, an error signal is generated which is proportional to the phase difference of the two signals. This signal is coupled back to a laser diode

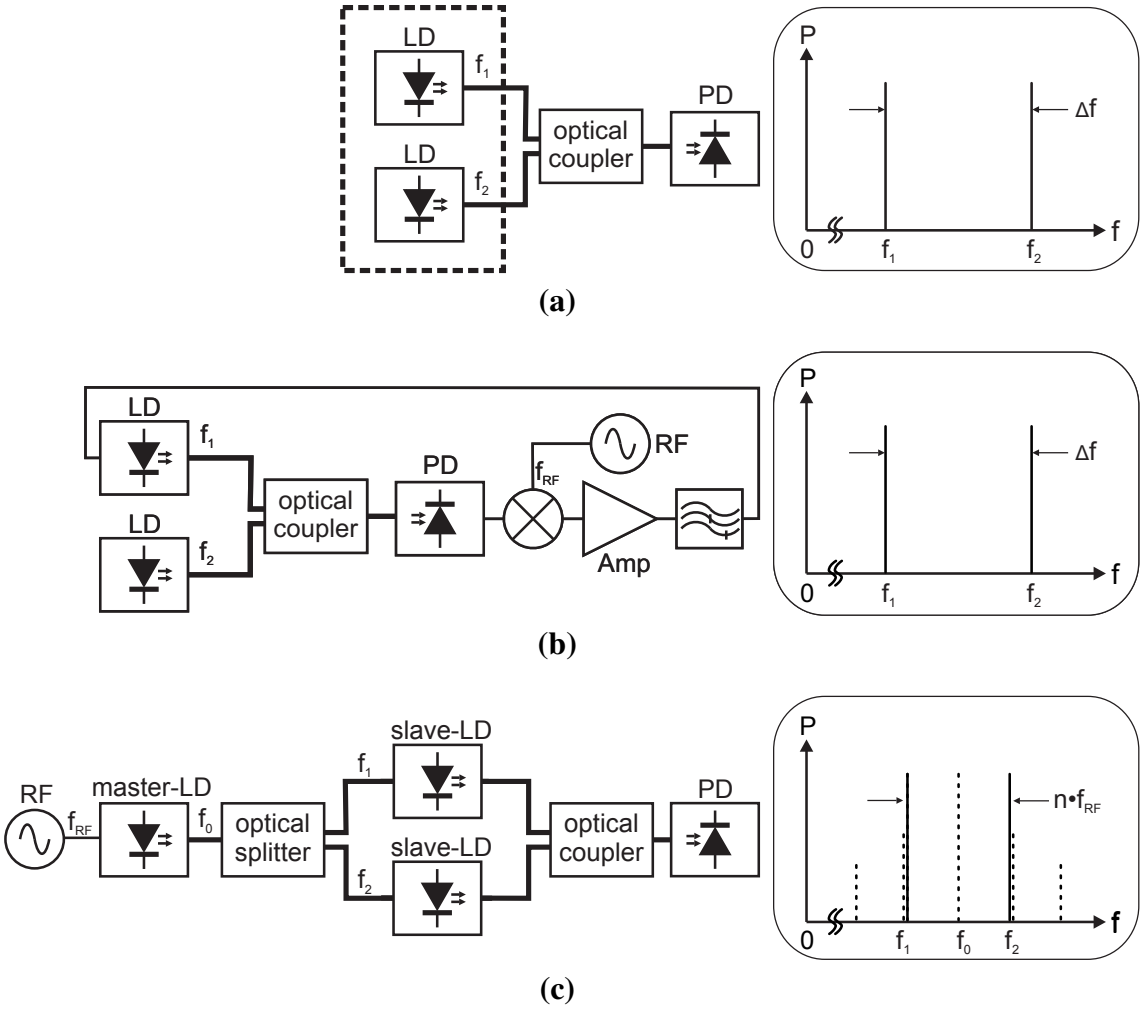

Figure 2.2: Dual-laser based techniques for photonic millimeter-wave generation, (a) free-running lasers, (b) optical phase locking and (c) optical injection locking.

and used to control the injection current or the cavity length. If loop gain and response time are designed appropriately, the phase fluctuations between both signals are reduced and the phase of the beat signal is locked to the phase of the RF reference. Various different methods and techniques have been developed for optical phase locking within the last years, reported for example in [48–54]. Main advantage of an optical phase locked loop is

a good temperature tracking capability and a wide locking range. Further on, comparatively cheap DFB lasers may be applied for an OPLL, which is e.g. reported in [55, 56]. A disadvantage is a high complexity of the whole setup. While using semiconductor lasers, a large feedback bandwidth is necessary due to the relatively high phase noise of a semiconductor laser compared to other alternatives. Moreover, the bandwidths of the microwave and mm-wave components in conjunction with the response of the slave laser have to be large and also uniform, making the fulfillment of these requirements difficult [57].

2.2.3 Optical injection locking

A further way to phase-lock two free-running lasers is the optical injection locking (OIL), where a typical setup is shown in **Fig. 2.2c** [58, 59]. An additional master laser is implemented in the system which is directly modulated with a frequency f_{RF}. The applied frequency modulation creates several sidebands with different orders around the central wavelength of the master laser. This signal is further injected into the two slave lasers. Now the wavelength of the two slave lasers is chosen to be located near the n-th order sidebands. Considering as an example the 2nd-order sidebands, the wavelength of the first slave lasers is located near $f_0 + 2f_{RF}$ and the wavelength of the second slave laser at $f_0 - 2f_{RF}$, thus locking the two slave lasers at the mentioned frequencies. After o/e-conversion in the photodetector an RF signal with a frequency of $4f_{RF}$ is generated here as an example. A further example of optical injection locking is given in [60]. Here, an 8.66 GHz signal (fourth subharmonic) was injected to create an RF signal of 34.64 GHz with a phase noise level of −77.5 dBc/Hz at an offset of 10 kHz. Optical injection locking offers a good phase noise suppression and allows to use low-frequency signals as a reference source. Another advantage is that also cheaper broad-linewidth lasers can be used. However, OIL offers only a small frequency detuning range and exhibits a comparatively high complexity [56].

2.2.4 Direct modulated laser

Another way of photonic mm-wave generation is to directly modulate the bias current of a semiconductor laser, thus generating two optical sidebands with phases locked together (see **Fig. 2.3a**).

Applying a direct modulated laser (DML) with a central frequency f_0 and an RF source with a frequency f_{RF}, the generated first-order sidebands are located at a frequency $f_0 + f_{RF}$ and $f_0 - f_{RF}$, respectively. Signal quality, especially with respect to phase noise, is directly related to the quality of the applied RF source. The direct modulation can be modeled in a simplified way with the injection current $i_{DML}(t)$

$$i_{DML}(t) = I_0 + i_{mod}(t), \tag{2.7}$$

where I_0 is a static injection current to operate within the lasing regime and $i_{mod}(t)$ represents the modulating signal. The corresponding output power of the laser $P_{DML}(t)$ can therefore be described as

$$P_{DML}(t) = P_0 + p_{mod}(t). \tag{2.8}$$

Electro-optical bandwidths with direct modulation of up to several tens of GHz have been achieved experimentally [61–63]. However, limiting key factors for high-speed modulation are an increasing frequency chirp for faster modulation, as well as relaxation resonances while the laser is switched on and off, respectively. If the modulation frequency is within the same order of magnitude like the relaxation resonance frequency, the data-modulated signal gets severely distorted together with an increase of relative intensity noise [64, 65]. Currently, commercially available direct-modulated lasers exhibit typical bandwidths of about 10 GHz at the maximum.

2.2.5 External modulation

To increase the modulation frequency, external modulation (EML) of a continuous-wave laser can be applied (see **Fig. 2.3b**), also requiring a mm-wave source delivering the desired mm-wave frequency [66–69]. The phase noise of the generated photonic mm-wave signal is directly related to the phase noise of the electrical mm-wave source. Another benefit compared to the DML is the increased extinction ratio which describes the power ratio between off-state (RF modulation off) and on-state (RF modulation on). Achievable values for a DML are within a range of 10 dB compared to about 30 dB while performing external modulation. Although suitable mm-wave sources up to several 100s of GHz are available, maximum frequency achievable with external modulation is limited to a value of 110 GHz. Limitations are given

by the bandwidth of the modulator mainly due to its RF electrode design and the RF driver amplifiers for increasing the modulation power to achieve a high modulation efficiency as well [70]. The two most relevant external modula-

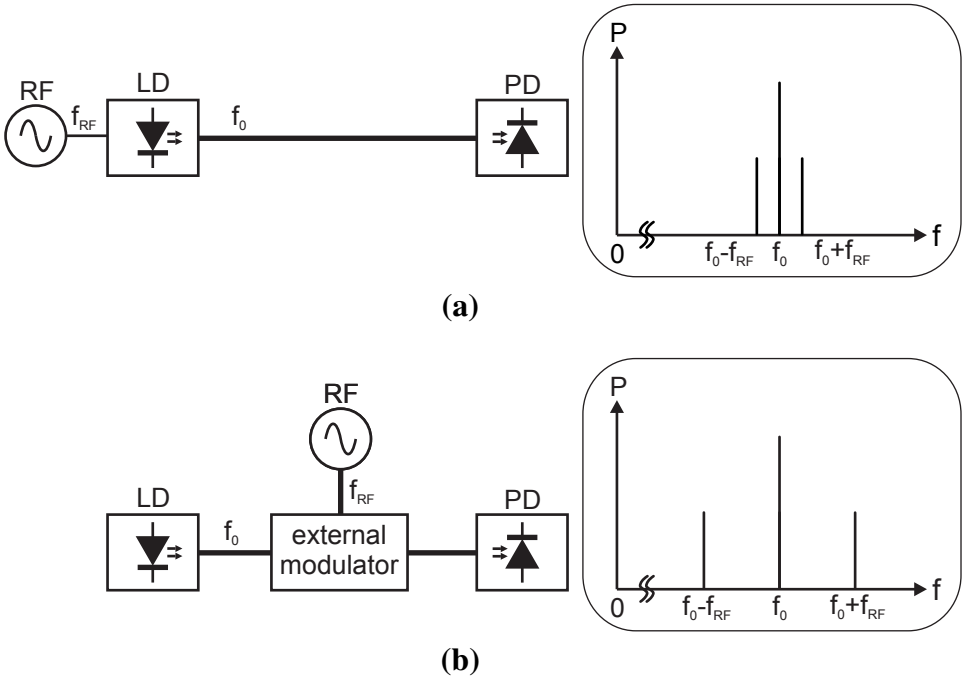

Figure 2.3: Techniques for photonic millimeter-wave generation based upon e/o-modulation, (a) DML and (b) external modulator.

tors are the electro-absorption modulator and the Mach-Zehnder modulator, allowing a broadband intensity modulation. Electro-absorption modulators are semiconductor devices where modulation is achieved by controlling an applied electrical field. The operation principle is based on the Franz-Keldysh effect, where the applied field alters the absorption spectrum causing a change in the bandgap energy and therefore in the absorption edge [71, 72]. The Mach-Zehnder modulator operation principle is based upon intensity modulation utilizing the linear electro-optic effect, also known as Pockels effect. Using a nonlinear crystal, an applied electric field modifies the refractive index of the utilized crystal proportionally to the field strength, which allows modulating the phase of the incident light [73]. By splitting, modulating and combining the optical signal the phase modulation can be transformed to intensity modulation. Compared to electro-absorption modulators, numerous specific advantages of the Mach-Zehnder modulator like an increased electro-optic bandwidth, a comparatively low insertion loss, zero-chirp or

a specific engineered pre-chirp to compensate dispersion effects justify an application within optical communication systems. Typical material systems used for Mach-Zehnder modulators are Lithiumniobat ($LiNbO_3$) or polymer materials [74]. On the other hand, Mach-Zehnder modulators exhibit larger geometries than electro-absorption modulators. Therefore, electro-absorption modulators are especially utilized for small-scale applications where integration is highly desired.

2.2.6 Mode-locked laser diode

A purely optical technique for photonic millimeter-wave generation is based upon passively mode-locked laser diodes (passive MLLD, see **Fig. 2.4**), where the mode locking frequency of a multimodal emitting laser is determined by the length of the cavity [75, 76]. Mode locking can be achieved e.g. by

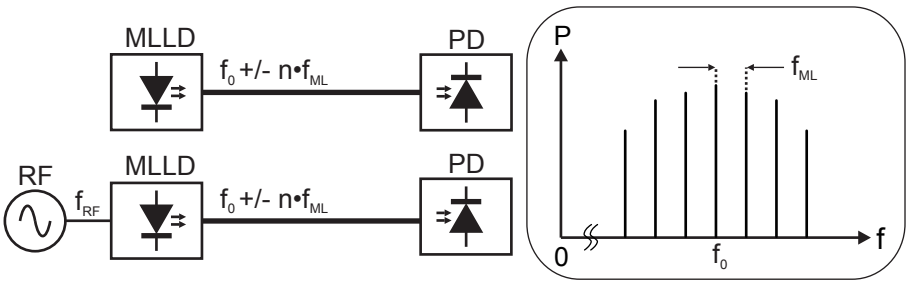

Figure 2.4: Photonic millimeter-wave generation based upon a passively and actively MLLD.

integrating a saturable absorber in the resonator which is typically placed at the end of a cavity. Recent results without applying a saturable absorber are reported in [77, 78], where passive mode-locking is realized due to four-wave mixing by strong gain as well as index modulation due to mode beating. Mode-locking frequencies of up to 1 THz have been achieved, exhibiting a frequency drift of less than 200 kHz/hour and a linewidth of less than 200 kHz [44]. The optical field of a mode-locked laser can be described as [79]

$$E(t) = \exp\left(2\pi j f_0 t\right) \sum_n E_n \exp\left[j\left(2\pi n f_{ML} t + \phi_n\right)\right], \tag{2.9}$$

where E_n is the amplitude of the n-th optical mode and f_{ML} the mode-locking frequency. At the photodetector, the photocurrent at the fundamental beating

frequency given by f_{ML} can be described as [79]

$$i_{ph,RF}(t) = \eta_{OE,RF} \sum_{n} E_n E_{n-1} \exp\left[j(2\pi n f_{ML} t + \phi_n - \phi_{n-1})\right], \qquad (2.10)$$

where $\eta_{OE,RF}$ denotes the opto-electrical RF-conversion efficiency of the photodetector. A way to improve phase noise and frequency stability of a mode-locked laser is to perform active mode-locking, i.e. by applying an RF signal to the laser in order to synchronize the output frequency of the MLLD with the RF source (see **Fig. 2.4**). This can be realized e.g. by integrating an optical modulator in the laser – either an electroabsorption modulator or an additional gain section where the pump current is modulated. The actively mode-locked laser is typically locked with a subharmonic RF-signal. Recent experimental results demonstrate an active MLLD with a mode-locking frequency of up to 240 GHz. Here, the laser was equipped with an integrated electroabsorption-modulator operated at a subharmonic frequency of 80 GHz [75].

2.2.7 Summary

Relevant state-of-the-art techniques for photonic mm-wave generation have been reviewed and discussed. All mentioned techniques and approaches exhibit several advantages and disadvantages, the key properties are summarized in **Tab. 2.1**. This work aims for photonic mm-wave generation concepts allowing RoF systems with low complexity. However, as data transmission rates within the multi-Gb/s range are targeted, a compromise between complexity and performance needs to be found.

The first approach of using two free-running lasers would offer a very simple solution, but phase noise and frequency stability make this approach unsuitable for broadband communication applications. Improving the performance with respect to phase noise and stability by OIL or an OPLL would be applicable, however adding severe complexity to the system. The DML would be very interesting in terms of complexity but is not suitable for creating a photonic 60 GHz signal due to its limited modulation bandwidth of around 10 GHz for the case of commercially available components. The necessary electro-optic bandwidth in this work is about 30 GHz which is further discussed in **3.1**.

This requirement can be fulfilled by applying external modulation while maintaining a satisfying complexity. A passive MLLD is also applicable and avoids furthermore the use of an external mm-wave source. In conclusion, the EML and the passive MLLD are further used in this work allowing photonic mm-wave generation with low complexity.

Table 2.1: Comparison of different techniques for photonic mm-wave generation.

Technique	Tunability (GHz)	Frequency (GHz)	Stability and noise
Dual-LD	>10,000	>10,000	Poor Large frequency drift High amount of phase noise
OPLL	>10	>100	Excellent Determined by electronics
OIL	<1	>100	Excellent Determined by electronics
DM-LD	>10	>10	Good Determined by electronics
EML	<100	<100	Excellent Determined by electronics
MLLD active	<1	>100	Excellent Determined by electronics
MLLD passive	<1	>1,000	Fair

2.3 Broadband photonic data transmission and modulation

Various digital modulation schemes are available; fundamental modulation techniques comprise phase shift keying (PSK), frequency shift keying (FSK) or amplitude shift keying (ASK) with two or more levels for increasing spectral efficiency. A prominent representative of combined modulation schemes is quadrature amplitude modulation (QAM) where both phase and amplitude carry information for further increasing spectral efficiency. Recent

developments within the field of digital signal processing allow a cost-efficient application of multi-carrier modulation schemes like orthogonal frequency division multiplexing (OFDM). This allows for example the compensation of spectral impairments while treating each subcarrier independently.

In this work, broadband data is transported within the optical and the wireless domain. While considering wireless communication, transmission standards and protocols are aiming to achieve a high spectral efficiency due to very limited available bandwidths. This is contrary to fiber-optic communication with huge amounts of available bandwidth and therefore relaxed requirements for spectral efficiency on the one side and high requirements to receiver sensitivity on the other side. Several options are available to modulate light with data, comprising techniques like phase-, intensity-, frequency- and polarization-modulation. However, for optical fiber communication, intensity modulation is the most popular and mature method due to its overall simplicity on the one hand and its robustness against distortions on the other hand. Due to the huge amount of available fiber-optic bandwidth, mainly binary amplitude modulation techniques (on-off-keying, OOK) are applied in commercial fiber-optic networks like non-return-to-zero (NRZ) or return-to-zero (RZ) on-off-keying. Nevertheless, with evolving fiber infrastructure advances in the field of digital signal processing as well as rising bandwidth demand, higher-level optical modulation schemes are currently under research like e.g. quadrature phase shift keying (QPSK) [80]. In addition, endeavors are going on to standardize ODFM for short-range optical transmission [81].

Most (optical) transmission standards like Ethernet and Synchronous Optical Networking (SONET) support NRZ-coding, which is exemplified in **Tab. 2.2**, especially indicating the gross data transmission rates. Considering overhead, actual payload rates are significantly lower due to coding format and due to forward error correction code if applicable. SONET is a widely-used protocol for carrying many signals with varying data transmission speeds through a flexible optical hierarchy while offering a synchronous transmission, classifying transmission speed in multiples of 51.8 Mb/s which is denoted as optical carrier level 1 (OC-1). Many fiber-optic networks are based upon OC-24 and OC-192, and currently fiber-optic networks are evolving to OC-768, offering transmission speeds of about 40 Gb/s. Ethernet was introduced for LANs in the past using copper transmission but was extended and more and more adapted to fiber-optic communication over larger distances. As an example,

extended-range 10 Gb/s Ethernet (10GBASE-ER) is specified for fiber-optic transmission of up to 40 km. A detailed study on existing fiber-optic standards and regulations is beyond the scope of this work, but the mentioned protocols shall indicate which data rates are state-of-the-art. Later on, transmission

Table 2.2: Comparison of broadband optical communication / transport protocols exhibiting transmission rates of larger than 1 Gb/s.

Type	Standard	Line Rate (Gb/s)	
Ethernet	1000BASE-PX	1.25	[82]
Ethernet	10GBASE-ER	10.3125	[82]
Ethernet	10GBASE-LX4	12.5	[82]
SONET	OC-24	1.2	[83]
SONET	OC-48	2.4	[83]
SONET	OC-96	4.8	[83]
SONET	OC-192	9.6	[83]

experiments are carried out in accordance to these transmission speeds not only for fiber-optic but also for wireless transmission. Maintaining the modulation format during fiber-optic and wireless transmission offers a transparent approach which would be highly desirable to reduce system complexity. The other major reason for applying fiber-optic standard related data rates and modulation formats is given by the simple fact that no wireless standard is available for fixed point-to-point outdoor connections offering transmission speeds of 1 Gb/s and more.

As a conclusion, the targeted data transmission speed in this work is as high as 12.5 Gb/s to fully support 10 Gb/s Ethernet. For digital modulation, NRZ-OOK is applied to achieve compliancy with the above mentioned standards. Further on, it allows simple and reliable system architectures with reduced complexity and low requirements on signal quality.

2.4 60 GHz frequency allocation and regulation

Within the conventional microwave spectrum, bandwidth allocations are strongly varying by country and region. Further on, only small amounts of

the spectrum are foreseen for unlicensed operation. Acquiring a license on the other side is typically time-consuming and expensive. This is different for the frequency range around 60 GHz. Many countries have already allocated several GHz of bandwidth in the 60 GHz band for unlicensed usage and even extended in the recent years, making this spectral allocation extremely attractive for broadband wireless communication [84, 85].

The responsible authority in Australia is the Australian Communications and Media Authority (ACMA) which has allocated a frequency range of 57–66 GHz for unlicensed indoor-operation with a maximum transmit power of 20 mW and an equivalent isotropic radiated power (EIRP) of 20 W. For outdoor operation (land and maritime deployments) the frequency range is limited to 59–63 GHz with a maximum EIRP of 150 W [86].

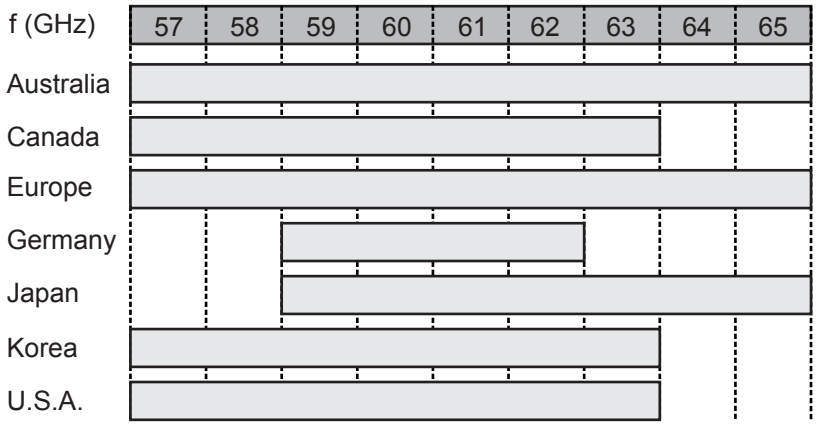

Figure 2.5: Unlicensed bandwidth around 60 GHz for different countries and regions.

In Canada, the regulation is done by the Industry Canada Spectrum Management and Telecommunications (IC-SMT) and is harmonized with the regulations valid in the U.S.A. allocating a range of 57.05–64 GHz for unlicensed operation while reserving the range of 57.00–57.05 GHz exclusively for a publicly available coordination channel. The EIRP is limited to a maximum value of 43 dBm while the maximum power to the antenna is limited to 27 dBm. Radiation exposure regulations further limit the peak power density measured at a distance of 3 m from the antenna to a value of 18 μW/cm^2 leading to a maximum power to the antenna within a range of 10 dBm depending on the antenna directivity [87].

The situation in Europe is significantly more complex as many countries are involved in standardization issues and have already published some own

preliminary standards in the past, as e.g. the below discussed regulation for Germany. A recent standard published by the Electronic Communications Committee (ECC) which is part of the the European Conference of Postal and Telecommunications Administrations (CEPT) defines a bandwidth of 57–64 GHz for unlicensed operation while specifying a maximum transmitter output power of 10 dBm, a minimum antenna gain of 30 dBi and a maximum EIRP of 55 dBm. The detailed frequency assignation is not included within the standard but shall be performed by the corresponding national administration [88]. The frequency range of 64–66 GHz is further regulated by the ECC [89]. These ECC standards define the limits for outdoor fixed wireless access.

Table 2.3: Emission power specifications around 60 GHz for different countries and regions.

Region	Max. TX power (dBm)	Max. EIRP (dBm)	Gain (dBi)	Citation
Australia	13	51.76	n.s.	[86]
Australia (indoor)	13	43	n.s.	[86]
Canada	27	43	n.s.	[87]
Europe	10	55	30 (min.)	[88, 89]
Europe (indoor)	n.s.	40	n.s.	[90, 91]
Germany	n.s.	40	35 (min.)	[92]
Japan	10	n.s.	47 (max.)	[93]
Korea	n.s.	10	n.s.	[94]
U.S.A.	27	43	n.s.	[95]

For indoor applications, a further standard was published by the European Telecommunications Standards Institute (ETSI), waiting for approval by the EC [90]. Here, the unlicensed frequency range is specified to 57–66 GHz with a maximum EIRP of 40 dBm in total and a power spectral density of 13 dBm/MHz. Another standard suggested for indoor applications was published in 2008 by the European Computer Manufacturers Association (ECMA), aiming for short-range communication over 10 m at the maximum especially targeting HDMI based upon the unlicensed bandwidth within the 60 GHz range. This standard defines for the first time details on the physical layer, suggesting single carrier block transmission (SCBT) and orthogonal frequency division multiplexing (OFDM) [91]. As an example of local EU member country regulations, a recent published German standard from the

Bundesnetzagentur limits the bandwidth to 59–63 GHz for outdoor point-to-point links while specifying a maximum power of 40 dBm (EIRP) and a minimum antenna gain of 35 dBi [92].

Japan was the first country worldwide with a standardized 60 GHz band, which was introduced in the year 2000 by the Ministry of Public Management, Home Affairs, Posts and Telecommunication (MPHPT). The unlicensed bandwidth was defined within 59–66 GHz. Output power and antenna gain are limited to 10 dBm and 47 dBi, respectively. Japanese law further limits the occupied bandwidth for a signal to 2.5 GHz [93]. In Korea, a frequency range of 57–64 GHz is scheduled for unlicensed operation by the Ministry of Information and Communication. A maximum transmit power of 10 dBm is foreseen while maximum antenna gain and EIRP are under discussion [94].

In the U.S.A., spectrum management is done by the Federal Communications Commission (FCC) which allocated 57.05–64 GHz for unlicensed usage. The EIRP and the maximum power to the antenna are limited to values of 43 and 27 dBm, respectively. Radiation exposure regulations further limit the peak power density measured at a distance of 3 m from the antenna to a value of 18 μW/cm^2 leading to a maximum power to the antenna within a range of 10 dBm depending on the antenna directivity [95].

The allocated spectra are summarized in **Fig. 2.5**, whereas **Tab. 2.3** shows emission power requirements about the corresponding region. As a conclusion, a huge amount of up to 9 GHz of unlicensed bandwidth is available for broadband wireless communication depending on country and region. In addition, the mentioned spectra are foreseen for unlicensed usage, making the exploitation of the 60 GHz band extremely attractive.

2.5 RoF systems state-of-the-art

Distributing optical radio signals instead of baseband signals has been attracting researchers for nearly two decades, taking advantage of the low fiber-optic loss and the option to transmit very broadband RF signals over significant fiber-optic distances [43].

A first experimental RoF system was developed in 1990, demonstrating the transmission of a 4-channel cordless telephony signal over single mode

fiber using subcarrier multiplexing [96]. After that, numerous other papers have been published within the frame of RoF utilizing wavelength-division multiplexing or subcarrier multiplexing and different network topologies [97–99]. Among other methods for photonic mm-wave generation previously discussed in **2.2**, a majority of the published RoF systems utilize intensity modulation based upon external modulation or by directly modulating a laser due to a high reliability, maturity and simplicity [100]. In this field, researchers have applied three different analogue modulation schemes, beginning with double-sideband transmission (DSB) where data is modulated onto an optical RF-carrier, thus creating the data-modulated carrier, a data-modulated lower optical sideband and a data-modulated upper optical sideband [101–106].

Although this method is comparatively easy to realize, DSB-systems are drastically limited due to chromatic dispersion in standard optical fibers. To reduce these power fading effects, various systems have been published with suppressed optical carrier, thus allowing increased fiber-optic transmission distances [107–113]. For some applications it may be useful to further improve the tolerance to chromatic dispersion of a RoF system which can be realized by optical single-sideband (SSB) transmission for the price of an increased system complexity as reported e.g. in [114–117]. A more detailed discussion of dispersion effects and fiber-optic range is given in **3.3**, especially comparing the conventional double-sideband system with the case of optical carrier suppression.

Advances in component technology, especially within the field of modulators and detectors, have continuously increased the RF frequency to more than 100 GHz [99, 118–120], however, broadband wireless data transmission was still difficult to realize due to a lack of suitable millimeter-wave amplifiers. Going along with improved component availability, RoF systems evolved in terms of achievable data rates and RF carrier frequency. However, only some of the experiments applied a real wireless distance but most of the experiments were carried out back-to-back due to a lack of appropriate RF components or an insufficient signal quality after fiber-optic transmission. **Tab. 2.4** summarizes major achievements within the field of RoF systems with respect to carrier frequency, data rate, wireless range and modulation format. A full description including e.g. fiber-optic-range, duplex capability or multi-user capability would go beyond the scope of this comparison.

Table 2.4: Broadband data transmission advances of RoF systems.

Year	Data rate	f_{RF} (GHz)	$d_{wireless}$ (m)	Modulation	Citation
1990	72 kb/s · 4	0.86	-	BFSK	[96]
1995	2.5 Mb/s · 2	41	-	BPSK	[121]
1998	140 Mb/s	70	-	FSK	[122]
1999	156 Mb/s · 2	60	5	DPSK	[105]
2000	400 Mb/s	60	-	BPSK	[123]
2003	622 Mb/s · 2	60	3	OOK	[124]
2003	1.25 Gb/s	120	2.5	OOK	[125]
2005	2.5 Gb/s	40	-	OOK	[108]
2005	3.0 Gb/s	240	0.1	OOK	[126]
2006	622 Mb/s	10	-	OOK	[113]
2006	10.3125 Gb/s	125	300	OOK	[127]
2006	2.5 Gb/s	40	-	OOK	[110]
2008	16 Gb/s	24	6	OFDM QPSK	[128]
2008	1.25 Gb/s	20	-	DPSK	[129]
2008	10 Gb/s	42	-	16-QAM	[80]
2008	10.6 Gb/s	94	800	OOK	[130]
2008	1.0 Gb/s	60	-	OOK	[131]
2009	500 kb/s	80	0.05	BPSK	[132]
2009	1.0 Gb/s	400	0.50	OOK	[133]
2009	10.0 Gb/s	30	1.5	OOK	[134]
2009	13.875 Gb/s	60	-	OFDM 4-QAM	[135]
2009	28.0 Gb/s	60	-	OFDM 16-QAM	[136]
2009	27.04 Gb/s	60	2.5	OFDM 16-QAM	[O33]
2008	12.5 Gb/s	60	50	OOK	this work [O7, O9, O13, O17, O23, O30]

Starting with [96], where 4 CT-2 channels have been transmitted at an RF frequency of below 1 GHz, the transmission capacity rose to 400 Mb/s in [123], applying optical injection locking for optical 60 GHz carrier generation. Further noticeable are the results in [108], where a 2.5 Gb/s data transmission is achieved using an RF carrier of 40 GHz. A really remarkable result

is presented in [127], were researchers demonstrated data transmission of 10.3125 Gb/s at an RF carrier frequency of 125 GHz, using antennas with very high directivity. Here, a high efficient photodetector was developed, able to generate o/e-converted electrical powers of up to 10 dBm without the need of an additional amplifier. This system was further qualified in 2008 within a long-term test trial reported in [137].

Systems with higher spectral efficiency are e.g. discussed in [128] and [80]. In [128], the authors report on a broadband transmission link using optical single-sideband techniques with improved dispersion tolerance and OFDM with QPSK subcarrier modulation, allowing 16 Gb/s data transmission. A photonic vector modulation approach by using several cascaded Mach-Zehnder modulators to create a 16-QAM signal is presented in [80]. At an RF carrier frequency of 42 GHz, data rates of up to 10 Gb/s have been transmitted with this approach. In [130], 10.6 Gb/s were transmitted wirelessly over a distance of 800 m. The optical carrier frequency of 94 GHz was here created by utilizing external modulation and by optical filtering the third-order sidebands created by a 15.67 GHz microwave source. A further 60 GHz RoF system is reported in [42]. Optical polarization multiplexing allowed here a simplified architecture for full-duplex capability.

The results shown in [132] are also impressive as the receiver consists of a photodetector used as an optoelectronic mixer. However, the extremely high conversion loss while performing optoelectronic downconversion limits the transmission distance to currently 5 cm. Broadband RoF transmission within the THz-range is reported in [133]. The authors furthermore presented a full carrier tunability within 300–400 GHz. A very compact RoF system operating at 30 GHz is reported in [134]. The authors have utilized two uncorrelated lasers with a frequency difference of 30 GHz, where one of the lasers was externally modulated with data rates of up to 10 Gb/s. However, as such a dual mode laser setup exhibits a large phase noise level, the system sensitivity was very low. The achieved wireless path length was 1.5 m. The systems reported in [136] and [O33] both utilize OFDM with 16-QAM subcarrier modulation. The consumed bandwidth was about 7 GHz in both cases according to spectral regulation issues previously discussed in **2.4**, allowing data transmission rates of 28.0 and 27.04 Gb/s, respectively. In [136], complexity was shifted to the optical link utilizing frequency quintupling of a 12 GHz LO signal requiring a total number of four Mach-Zehnder modulators besides further optical

components. In contrary, the system in [O33] applies frequency doubling for photonic millimeter-wave generation and exhibits an overall reduced complexity.

An impressive advance in terms of bandwidth can be observed from the tabular. However, a detailed comparison is difficult as different channel characterization methods have been used within these publications. Experimental results with single carrier and binary modulation schemes are mainly based upon real BER measurements where signal evaluation is performed on-line. Measurements on systems with multilevel modulation schemes are accomplished with sampling oscilloscopes by acquiring short snapshots of the received signal and performing signal analysis off-line. In some publications, solely eye diagrams are shown for a qualitative comparison. Further on, most publications do not consist of wireless experiments, use different carrier frequencies and target different application scenarios which makes a detailed performance comparison challenging.

However, only few publications demonstrate data transmission rates of 10 Gb/s and above as motivated in **2.3**. In addition, such reported multi-Gb/s RoF systems operating at 60 GHz (motivated in **2.4**) do not comprise any wireless transmission experiments [135, 136]. Therefore, aim in this thesis is to develop 60 GHz RoF systems which support such capacities and allow furthermore wireless transmission over technical relevant distances.

3

System description, theoretical and experimental evaluation

Different RoF systems have been studied and will be presented in chapters **5**–**7**. For developing a model to theoretically describe and analyze all the realized RoF systems, each system was divided into generic subsystems that can be found in each of the realized RoF systems. The aim of this chapter is to model and to describe these subsystems while considering signal power and noise contribution of each component to deduce a full system description. For an appropriate modeling, impairments during fiber-optic and wireless trans-

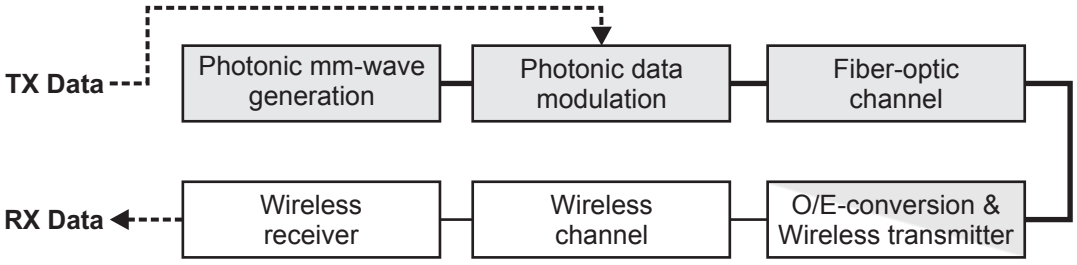

Figure 3.1: Overview of the subsystems in a radio-over-fiber link.

mission are further described in this chapter which is shown schematically in **Fig. 3.1**. The realized subsystems for photonic millimeter-wave generation are

detailed in **3.1**, followed by the applied broadband photonic data modulators in **3.2**. Channel impairments and transmission limitations while propagating through an optical fiber are given in **3.3**. After fiber-optic transmission, the data-modulated photonic mm-wave signal is back-converted to electrical domain and further wirelessly transmitted, which is described in **3.4**. Besides the o/e-converted signal, various different noise contributions are o/e-converted as well, a mathematical description of the optical and opto-electrical noise sources is performed in **3.5**. Wireless propagation impairments and an appropriate channel description are the subject of **3.6**. After wireless transmission the signal is finally received and post-processed for channel characterization in **3.7**. This chapter is concluded in **3.8**. The applied electrical and optical components are itemized in annex **A**.

3.1 Photonic mm-wave generation

This section describes the applied subsystems for photonic millimeter-wave generation based upon the study accomplished in **2.2**. The employed concepts utilize external modulation as well as a passively mode-locked laser diode developed within the IPHOBAC project (see **1.6**).

3.1.1 External modulation

A schematic of the photonic millimeter-wave generator based upon external modulation is shown in **Fig. 3.2**. A laser with a central wavelength f_0, an

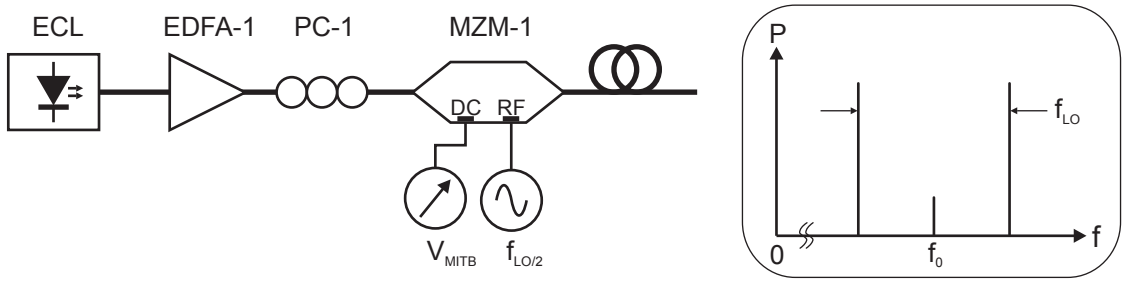

Figure 3.2: Photonic millimeter-wave generator based upon external modulation. The optical signal consists of two sidebands with a difference frequency of f_{LO} and a suppressed mode from the ECL at a frequency of f_0.

amplitude A_0 and an angular frequency ω_0 is amplified by an erbium-doped

fiber amplifier (EDFA), rising the amplitude to a level of B_0. The applied laser was an InGaAsP Fabry-Perot semiconductor laser system with external cavity (ECL) which is power- and wavelength-tunable. The utilized EDFA-1 was a power amplifier with tunable gain allowing a maximum optical output power of 200 mW and a noise figure of 6 dB. This is followed by a polarization controller (PC-1) to adjust the polarization state of the light for the Mach-Zehnder modulator, which is extremely polarization-sensitive. The generated optical wave is described as

$$E_0(t) = B_0 \cos(\omega_0 t) . \tag{3.1}$$

The modulator is biased to a minimum transmission point and modulated with a millimeter-wave signal at a frequency of $f_{LO/2}$ while suppressing the optical central wavelength λ_0. The outbound optical field from the modulator consists now of the suppressed optical carrier and two optical sidebands, the lower sideband (LSB) and the upper sideband (USB). Neglecting higher order sidebands due to remodulation and nonlinearities of the modulator, the optical field is thus described as

$$\begin{aligned} E_1(t) &= C_{LSB} \cos\left[(\omega_0 - \omega_{LO/2})\, t\right] + C_{USB} \cos\left[(\omega_0 + \omega_{LO/2})\, t\right] + \\ &+ C_0 \cos(\omega_0 t) , \end{aligned} \tag{3.2}$$

where C_0, C_{LSB} and C_{USB} describe the amplitudes of carrier and optical sidebands, respectively. Supposing sufficiently high carrier suppression, i.e. $C_0 \ll C_{LSB}$ & C_{USB}, as well as equal sideband amplitudes, **(3.2)** is simplified to

$$E_1(t) = C \cos\left[(\omega_0 - \omega_{LO/2})\, t\right] + C \cos\left[(\omega_0 + \omega_{LO/2})\, t\right] . \tag{3.3}$$

Mach-Zehnder modulator operation principle

The operation principle especially aiming for the above mentioned carrier suppression is detailed in the following, starting with the schematic structure of a Mach-Zehnder modulator shown in **Fig. 3.3**. It consists of an optical splitter, an RF section where data modulation is applied, a DC section for adjusting the desired operation point of the modulator and finally an optical combiner where the divided parts of the light are coupled together. The

optical signal in an arm can be phase-modulated by applying a voltage to the RF electrodes as the electrical field alters the refractive index of the optical waveguide, thus modifying the optical length of the waveguide and inducing a phase shift of $\Delta\phi_{RF}(t)$. A static voltage can be applied to the DC-electrode which further induces a static phase shift of $\Delta\phi_{DC}$. The signal

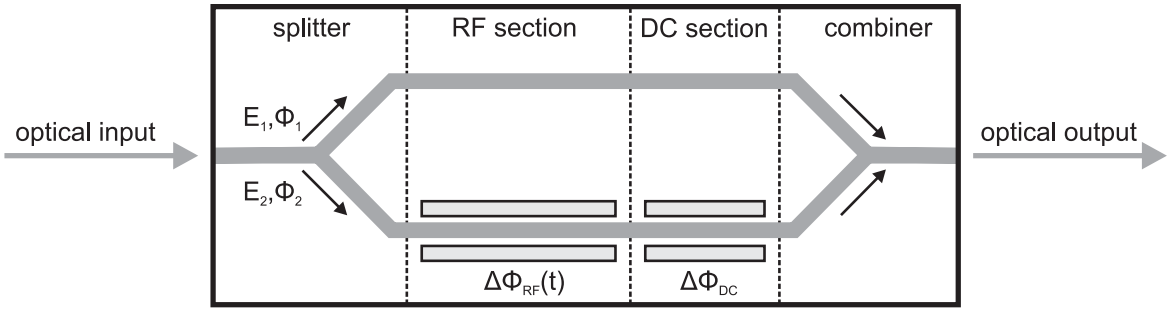

Figure 3.3: Schematic structure of a Mach-Zehnder modulator consisting of an optical splitter, an RF section for data modulation, a DC section for controlling the operation point and a power combiner section.

parts from both arms are coupled together at the combiner, and the phase-modulation is transformed to an intensity-modulation. When combining in-phase, maximum optical transmission is achieved. While increasing the phase difference between the two optical modes, higher-order modes are excited which cannot propagate in the outbound optical waveguide and are therefore scattered into the surrounding substrate. The transmitted optical power at the modulator output is reduced. If phase difference equals to 180°, no light propagates in the fundamental mode and ideally the complete optical power is scattered into the substrate [138]. Even for in-phase recombination a specific amount of optical power gets lost which is denoted as the insertion loss IL. It describes the fraction of optical inbound power $P_{opt,in}$ and outbound power $P_{opt,out}$ and is mainly induced by fiber-chip coupling losses, splitting with subsequent recombination and the material-specific loss of the waveguide as well. Although in theory transmitted optical power for a 180° phase shift is expected to be zero, a specific amount of optical power is still transmitted. This is based upon the fact that the split ratio between both optical arms cannot be exactly manufactured to 50 %. Another point which may limit the actual achievable extinction ratio is the non-infinitely low linewidth of an optical input signal and the fact that a phase shift of π can be achieved only for one specific wavelength at the same time. The fraction of maximum and minimum

transmission is denoted as the extinction ratio *ER*. The nonlinear transfer function of a Mach-Zehnder modulator, i.e. optical outbound versus inbound intensity assuming only a single electrode is described as [139–141]

$$T_{MZM} = \frac{1}{2}IL\left[1 + \cos\left(\pi\frac{V(t)}{V_\pi} + \Delta\phi_{int}\right)\right], \tag{3.4}$$

where $\Delta\phi_{int}$ is an intrinsic phase shift mainly caused by production impairments of the modulator and $V(t)$ a general applied voltage. The required voltage to tune the Mach-Zehnder modulator from minimum to maximum transmission, i.e. to cause a phase shift of 180° is denoted as V_π. To avoid additional bias-T structures most modulators have separated electrodes for DC and RF supply, as indicated in **Fig. 3.3**, to control the operation point and to apply modulation, respectively. Separate values for V_π are therefore given: $V_{\pi,DC}$ for the DC-electrode and $V_{\pi,RF}$ for the RF-electrode. Assuming now an applied modulating voltage $V_{RF}(t)$ to the RF-electrode and a static DC voltage V_{DC} applied to the DC-electrode, **(3.4)** can be rewritten into

$$T_{MZM} = \frac{1}{2}IL\left[1 + \cos\left(\frac{\pi V_{RF}(t)}{V_{\pi,RF}} + \frac{\pi V_{DC}}{V_{\pi,DC}} + \Delta\phi_{int}\right)\right]. \tag{3.5}$$

The modulator's nonlinear electro-optical response and its key parameters are shown in **Fig. 3.4**, giving the relationship between optical output power versus applied voltage. Important DC biasing conditions of a Mach-Zehnder

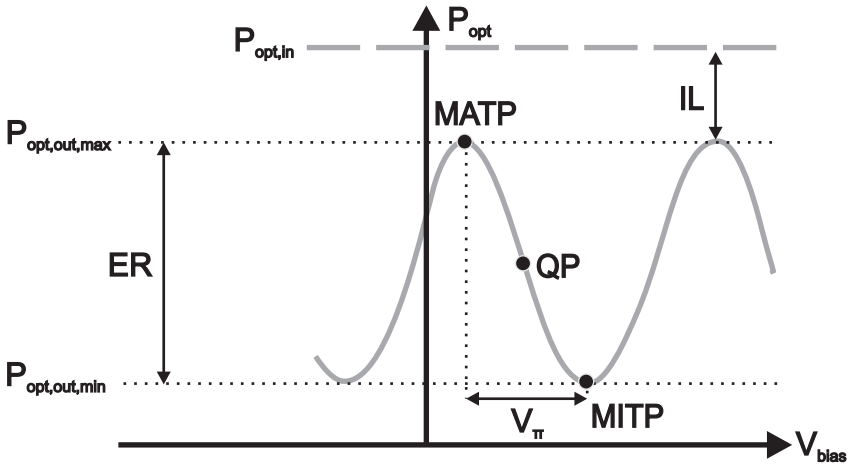

Figure 3.4: Schematic of the non-linear electro-optic transfer function and important key parameters of a Mach-Zehnder modulator.

modulator are further indicated in the figure. The operation point for maximum transmission is denoted as the maximum transmission point (MATP) and vice-versa the minimum transmission point (MITP) for minimum transmission. This will be discussed further in the text. For data modulation, typically the quadrature point (QP) is chosen, defined as (MITP+MATP)/2, as it offers maximum electro-optic slope efficiency for a given modulating voltage $V_{RF}(t)$ and further allows a quasi-linear modulation if the signal power is sufficiently low. This is especially important for the case of multilevel modulation formats with high demands on linearity.

60 GHz carrier generation and optical carrier suppression

The demand for linearity is less stringent when applying a modulator for photonic mm-wave generation, as no amplitude discretization is required and unwanted harmonics while applying an LO signal with high power are eliminated due to the frequency response of the photodetector during o/e-conversion and mm-wave amplifiers applied for wireless transmission as well. Biasing to MITP can be beneficial in this case and will be discussed in the

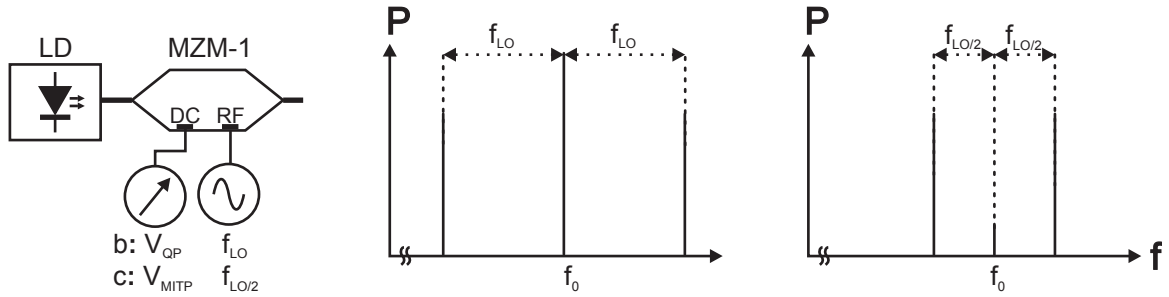

Figure 3.5: (a) Schematic setup for photonic mm-wave carrier generation. Optical spectrum while applying (b) an RF frequency of f_{LO} and DC-biasing to the QP and (c) an RF frequency of $f_{LO/2}$ and DC-biasing to the MITP.

following. Assuming a simplified setup as shown in **Fig. 3.5a**, a laser diode LD is coupled to a Mach-Zehnder modulator MZM-1 and the modulator is biased by different DC voltages. Utilizing a DC bias to operate at the quadrature point and further applying a sinusoidal RF-signal with a frequency of f_{LO}, two optical sidebands – an upper and a lower optical sideband with

a frequency difference of f_{LO} related to the frequency of the optical carrier f_0 – are generated (see **Fig. 3.5b**). When the optical signal is o/e-converted by a photodetector both sidebands beat with the optical carrier producing an electrical frequency of f_{LO}. In contrast, if bias is set to the minimum transmission point with respect to the optical carrier, the carrier is canceled out as the phase shift between both arms is set to π. While applying an electrical signal with half the desired mm-wave frequency, i.e. 30 GHz to the RF electrode of the modulator, the total frequency difference between both sidebands is 60 GHz (i.e. $2f_{LO/2}$, see **Fig. 3.5c**). If carrier suppression is sufficiently high, beating with the carrier can be neglected during o/e-conversion and solely an electrical 60 GHz signal is detected. Summarizing these points, the optical carrier suppression allows reduced requirements in terms of frequency for the electrical LO source. Further on, the tolerance to chromatic dispersion is significantly improved which is subject in **3.3**.

Applied Mach-Zehnder modulators

In this work, two 40 Gb/s Mach-Zehnder modulators (MZM-1 and MZM-2) have been applied which exhibit specified electro-optic bandwidths of 30 GHz

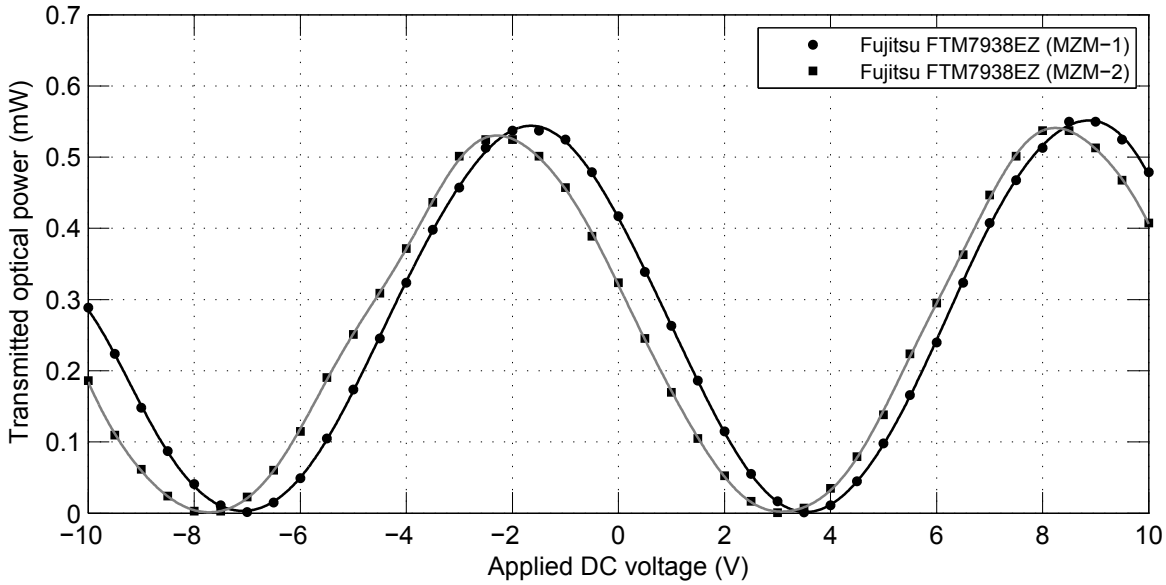

Figure 3.6: Opto-electronic DC transfer functions of the applied Mach-Zehnder modulators measured at a wavelength of 1562 nm and an optical input power of 2 mW.

at the minimum. A characterization of the modulators' key parameters has been carried out to allow a calculation of the electro-optic conversion efficiency which is further discussed in **3.2**. In a first step, the electro-optic transfer functions have been measured which is shown in **Fig. 3.6**. This was accomplished by applying a power of 2 mW to the optical input and by altering the voltage applied to the DC-electrode of the modulators. The laser source (ECL) was adjusted to a wavelength of 1562.25 nm. As can be seen, $V_{\pi,DC}$ of the modulators was measured to 2.8 and 2.7 V for MZM-1 and MZM-2, respectively. From the measurement, an insertion loss of 5.6 dB and a DC extinction ratio of 26.5 dB was deduced. The values for MZM-2 were 5.8 dB and 23.2 dB, respectively. Based upon the DC results, the modulators were biased to the quadrature point while applying an RF signal to the RF electrode with the aim to evaluate $V_{\pi,RF}$. For MZM-1, a 30 GHz sinusoidal RF signal was applied to the electrode input resulting in a value of 2.8 V_{pp} for $V_{\pi,RF}$. In contrast, MZM-2 was operated at 10 GHz as this modulator was applied for data modulation giving a value of about 2.0 V_{pp}.

Optical millimeter-wave signal

With the results above, the optical carrier suppression has been experimentally

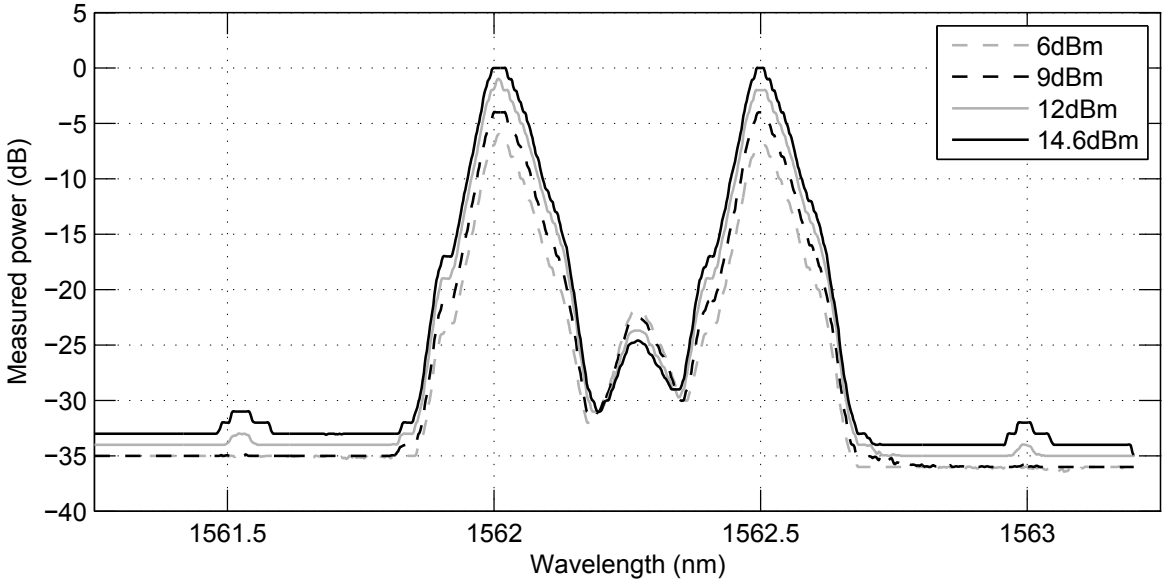

Figure 3.7: Optical spectrum of the DSB-CS signal measured after MZM-1 with different applied LO powers.

evaluated while DC-biasing to the MITP which is shown in **Fig. 3.7**. The 30 GHz LO source was set to output powers of 6, 9, 12 and the maximum of 14.6 dBm, leading to carrier suppression levels of 15, 18, 22 and 25 dB, respectively. The increase in carrier suppression relatively to the sidebands is based upon the fact that the sideband power rises with increasing RF modulation whereas the absolute power of the optical carrier remained about the same. Harmonics suppression is at least 7 dB better and therefore insignificant if compared to carrier suppression. The harmonics in this measurement were induced by several effects like four-wave mixing, modulator nonlinearities, as well as harmonics delivered by the LO source.

3.1.2 Photonic mm-wave generation using a passive MLLD

The second method for photonic millimeter-wave generation applied in this work is based upon a passively mode-locked laser diode as introduced in **2.2**. The laser is an experimental quantum-dash mode-locked laser developed within the IPHOBAC project [77]. As can be seen from **Fig. 3.8**, the subsys-

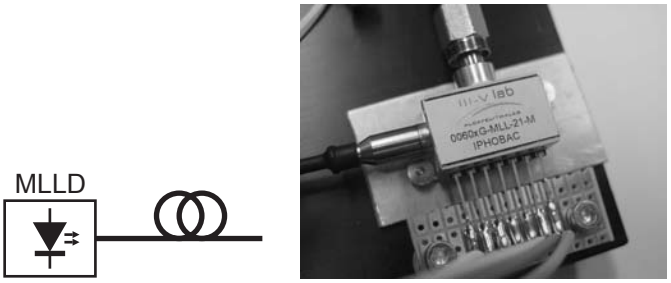

Figure 3.8: Photonic millimeter-wave generator based upon a passively mode-locked laser diode showing the schematic setup in (a) and the experimental setup in (b).

tem consists solely of the mode-locked laser diode without any additional components besides the obligatory laser temperature control for supplying a cooling current to a laser-integrated Peltier element and a further DC source for current injection to the laser diode. Within the chosen operating point, i.e. applying an injection current of 205 mA and adjusting the temperature to 25 °C, the laser exhibited a mode-locking frequency of 58.8 GHz. The optical spectrum of the MLLD is shown in **Fig. 3.9**, according to the formula given in **(2.9)**. As can be seen, the optical comb exhibits several modes within a

wavelength region of 1560 to 1577 nm, with an individual mode spacing of 58.8 GHz. Later on in this work all optical modes will be simultaneously modulated with data and o/e-converted, giving reason to expect a significant chromatic dispersion problem discussed in **3.3**.

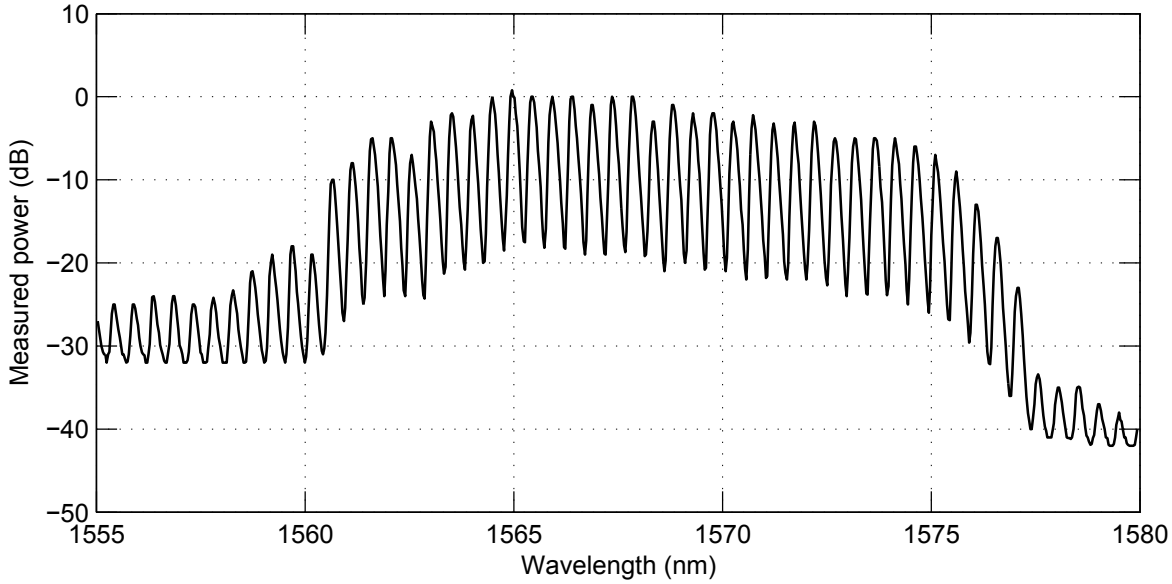

Figure 3.9: Optical spectrum of the applied mode-locked laser diode operated at a temperature of 25 °C and an injection current of 205 mA. The locking frequency under these conditions is 58.8 GHz.

3.2 Broadband photonic data modulation

Photonic data modulation in this work is realized by applying external modulators, a Mach-Zehnder modulator (MZM-2) which was characterized in the previous section and a 10 Gb/s electro-absorption modulator (EAM).

3.2.1 Photonic data modulation using an MZM

For broadband modulation in the optical domain, a Mach-Zehnder modulator (MZM-2) is applied which is shown in **Fig. 3.10**. Due to the polarization dependent losses, a polarization controller (PC-2) is applied before the modulator. The modulator itself is biased to the quadrature point. With an applied input signal, e.g. a DSB-CS signal, the modulator acts as an optical mixer,

multiplying the optical mm-wave carrier with the data signal. To compensate insertion and modulation losses, a low-noise EDFA with a noise figure of 4.5 dB is implemented in the system (EDFA-2). This is followed by an optical band-pass filter (OBPF) to remove amplified spontaneous emission (ASE)

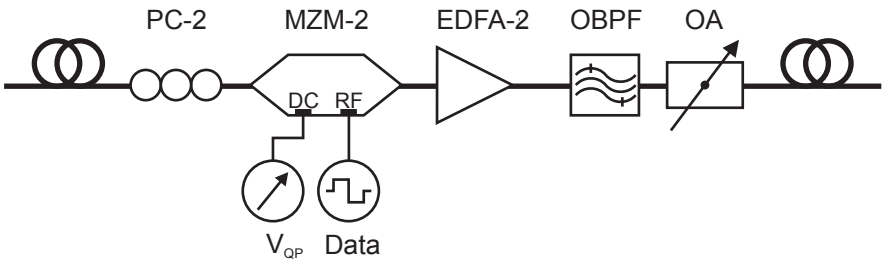

Figure 3.10: Photonic data modulator using a Mach-Zehnder modulator.

noise. An optical attenuator (OA) is applied to control the optical power for o/e-conversion in order to control the electrically generated power further utilized for BER characterization. To evaluate the performance of the modulation procedure and to calculate the signal gain, a complete optical link is supposed, consisting of a modulator which performs e/o-conversion and a photodetector which executes o/e-conversion. This allows a computation of the equivalent-electric signal gain of the optical link.

While further assuming an ideal o/e-converter, which means in particular ideal opto-electronic conversion with a quantum efficiency of one, as well as an ideal quadratic behavior of the detector, the equivalent-electric gain of the modulator can be extracted. An ideal opto-electronic converter which is used as reference can be described as

$$\eta_{OE,ref} = \frac{e\lambda}{hc}, \tag{3.6}$$

where e is the electron charge, λ the optical wavelength, h the Planck constant and c the speed of light. The quantum efficiency is here assumed to be one. For instance, an ideal responsivity of 1.26 A/W can be calculated for an optical wavelength of 1560 nm. Further on, the slope efficiency of a Mach-Zehnder modulator is calculated by [138]

$$\eta_{EO,RF} = Z_{in}\frac{\pi}{2}\frac{P_{opt,in}\mathit{IL}}{V_{\pi,RF}}, \tag{3.7}$$

where Z_{in} denotes the electrical input impedance, IL the insertion loss, $P_{opt,in}$ the optical input power applied to the modulator and $V_{\pi,RF}$ the voltage difference between maximum and minimum transmission. As can be seen from equation **(3.7)**, the conversion efficiency is directly related to the optical input power. Except this value, all other parts are fixed parameters depending on the applied modulator. Thus, the only option to increase $\eta_{EO,RF}$ for a given modulator is to apply more optical power. Based on $\eta_{EO,RF}$, the equivalent RF-gain G_{el} is calculated by [138, 142]

$$G_{el} = \left(\eta_{EO,RF}\,\eta_{OE,ref}\right)^2 \left(\frac{Z_{ref}}{Z_{in}}\right), \tag{3.8}$$

where Z_{ref} is the reference characteristic impedance and Z_{in} the modulator's input impedance.

3.2.2 Photonic data modulation using an EAM

The second approach of broadband photonic data modulation is shown in **Fig. 3.11**, comprising an electro-absorption modulator (EAM) which is followed by an optical amplifier (EDFA-2) to compensate the modulation losses. The OA is applied to control the optical power to the photodetector which

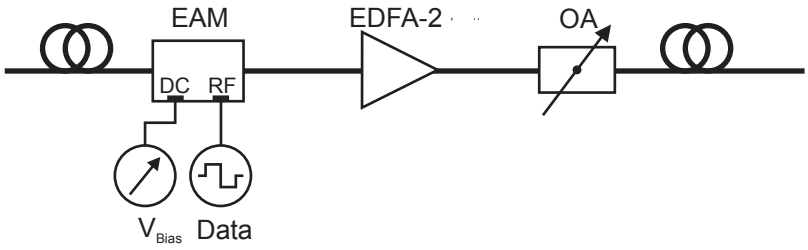

Figure 3.11: Photonic data modulator using an electro-absorption modulator.

allows an adjustment of the generated RF-power at the photodetector. The nonlinear electro-optic transfer function of an EAM can be described as [142]

$$T_{EAM} = \mathit{IL}\,\mathrm{e}^{-\gamma\,\alpha(V)L}, \tag{3.9}$$

where IL is the insertion loss of the modulator while applying a zero voltage to the input. The optical confinement factor γ denotes the quality of the optical waveguide to guide the optical field, $\alpha(V)$ is a factor to consider the changing

optical absorption coefficient due to applied bias voltage and L the modulation length. The slope efficiency of an EAM is further described as [138]

$$\eta_{EO,RF} = Z_{in} \frac{\mathit{IL}\, P_{opt,in}}{V_\alpha}, \tag{3.10}$$

where IL describes the static insertion loss without applied voltage to the modulator and V_α the difference voltage between minimum and maximum transmission in analogy to V_π. The measured electro-optic transfer function

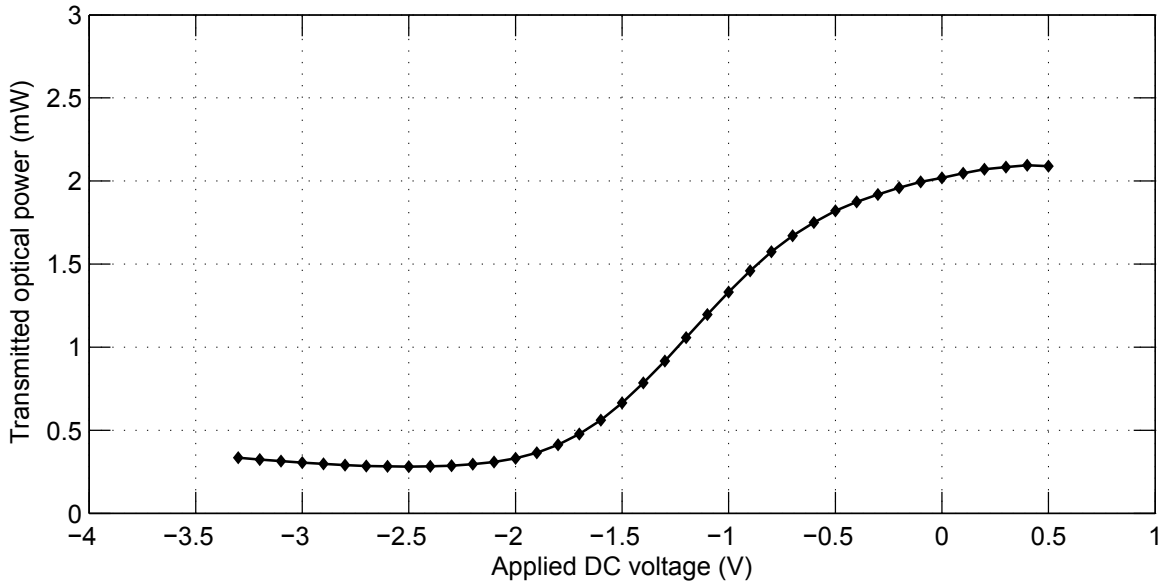

Figure 3.12: Opto-electronic DC transfer function of the applied EAM measured at a wavelength of 1562 nm and an optical input power of 10 mW.

of the applied electro-absorption modulator is shown in **Fig. 3.12**. With an optical input power of 10 mW the extracted values for IL and V_α are 6.8 dB and 2.8 V, respectively.

3.3 Fiber-optic channel and chromatic dispersion

Various impairments emerge for a signal while propagating through a fiber which may be classified into attenuation, non-linear propagation and dispersion. The key impairments in this work are signal attenuation and chromatic dispersion. While traveling through an optical fiber, the light is exponentially

attenuated with the distance due to absorption as well as scattering. The fiber attenuation α is calculated by

$$\alpha = \frac{1}{L} 10 \log_{10} \left(\frac{P_0}{P_L} \right), \tag{3.11}$$

where P_0 and P_L describe the incident and transmitted optical power after propagation within a fiber of the length L. Typically, α is given in dB/km and current available silica glass single mode fibers exhibit a minimum loss of 0.16 dB/km at a wavelength of 1.55 μm [143]. Absorption in silica glass depends strongly on the optical wavelength and exhibits two main absorption bands, an ultraviolet absorption band caused by electronic as well as molecular transitions and a middle-infrared absorption band due to vibrational transitions. A further phenomenon is the Rayleigh scattering which denotes random inhomogeneities of the refractive index leading to small scattering centers [143]. The second major undesired property is the signal dispersion based upon several origins while propagating through a dispersive fiber, describing the fact that the refractive index is dependent on the wavelength, resulting in slightly different group velocities for each spectral component. Intermodal dispersion occurs in multi-mode fibers and results from different propagation properties of higher-order transverse modes and severely limits the possible fiber-optic transmission range and bandwidth, respectively [144]. Polarization mode dispersion results from polarization-dependent propagation properties and becomes an important issue for single-mode fiber-based optical transmission systems with data rates of 40 Gb/s and above [145–147]. Material dispersion describes the wavelength-dependency of the refractive index, which is an intrinsic property of silica glass. It exhibits a negative value for optical wavelengths within the visible range, zeroes at about 1312 nm and exhibits significantly positive values within the wavelength region of 1550 nm. Waveguide dispersion describes the effect of a wavelength-dependent field distribution in the fiber, i.e. in core and cladding, where short wavelengths are more confined to the core and only a small amount of power propagates within the cladding. On the other hand for longer wavelengths a more significant amount of the total propagating light is transmitted within the cladding. Core and cladding exhibit different refractive indices, leading to different propagation speeds and thus to signal dispersion for considerable high optical bandwidths. At around 1550 nm, waveguide dispersion has a minor influence compared to the material dispersion. The sum of material and waveguide dis-

persion is denoted as chromatic dispersion, which is deduced in the following. The propagation constant is calculated by [143]

$$\beta_p(\omega) = n(\omega)\,\frac{\omega}{c}, \tag{3.12}$$

where $n(\omega)$ is the frequency-dependent refractive index. By further assuming that the bandwidth of the optical signal $\Delta\omega$ is much lower than the optical central frequency ω_0, as well as an only slightly and gradually varying propagation constant, a Taylor series expansion can be performed for the linear part of the propagation constant [143]

$$\beta_L(\omega) \approx \beta_0 + \beta_1(\Delta\omega) + \frac{\beta_2}{2}(\Delta\omega)^2 + \frac{\beta_3}{6}(\Delta\omega)^3, \tag{3.13}$$

where $\beta_n = (d^n/d\omega^n)_{\omega=\omega_0}$. Further transformation and calculation leads to the group velocity v_g, whose relationship to β is expressed as

$$\frac{1}{v_g} = \frac{d\beta}{d\omega}. \tag{3.14}$$

The pulse broadening is caused by β_2 and β_3 which are denoted as the second- and third-order dispersion terms leading to the dispersion parameter D and the dispersion slope S. The dispersion parameter is calculated by [143]:

$$D = \frac{d\beta}{d\lambda}\left(\frac{1}{v_g}\right) = -\frac{2\pi c}{\lambda^2}\beta_2. \tag{3.15}$$

The applied single-mode fibers in this work exhibit typical values of $D \approx 17$ ps/(nm/km). Depending on RF carrier frequency, signal bandwidth and the analogue modulation scheme, chromatic dispersion may be a limiting factor in RoF systems due to a comparatively high amount of consumed optical bandwidth. This is especially the fact for systems where an external modulator is utilized for photonic mm-wave generation, creating two optical sidebands without suppressing the optical carrier as previously introduced in **Fig. 3.5b**. Carrier and sidebands propagate with different speeds through a dispersive fiber. At the photodetector, both spectral components mix with the optical carrier while exhibiting a phase difference, leading to a power loss or power penalty. As an example, RoF systems operating at 60 GHz and using DSB optical modulation allowed fiber-optic transmission lengths within a

range of some 100 meters, which is e.g. reported in [101,106]. Several options are available to counter chromatic dispersion, like dispersion compensating fibers with a negative dispersion parameter or dispersion-shifted fibers with a reduced value of D [148, 149]. However, such fibers are barely applicable for existing fiber-optic infrastructure as this would require a partial replacement of already installed standard single-mode fibers. A further option is to utilize fiber-Bragg gratings with a negative value for D [150, 151]. Countering dispersion can also be performed on the electrical side by electronic dispersion compensation (EDC) which is available due to recent progress in digital signal processing. EDC can either be realized on the transmitter side (predistortion) or at the receiver side (post-compensation), which is e.g. reported in [152,153]. A very promising optical approach to counter chromatic dispersion is known as optical single-sideband transmission, comprising various techniques for removing signal parts from the optical spectrum before photodetection [115]. A common approach here is to use a dual-arm Mach-Zehnder modulator. By applying an RF signal directly to the first RF input and to phase-shift the RF signal by 90° before connecting it with the second RF input, one sideband is canceled out [43]. However, all these methods increase system complexity and require additional optical and electrical components, respectively. On the other side as mentioned above, conventional 60 GHz DSB RoF systems exhibit a fiber-optic transmission span of some 100 meters which is simply not enough for most applications. The technique of optical carrier suppression – applied in this work for photonic mm-wave generation in **3.1.1** – offers here an alternative, allowing a sufficiently large fiber-optic transmission span while maintaining low system complexity. This is presented in **3.3.1** by a comparison of DSB-CS modulation with DSB modulation. The dispersion properties of the second applied technique for photonic mm-wave generation by using an MLLD (shown in **3.1.2**) are furthermore discussed in **3.3.2**.

3.3.1 Dispersion induced power penalty utilizing MZM cascading

After fiber-optic transmission of a photonic mm-wave signal through a dispersive fiber the signal may exhibit a reduced power due to chromatic dispersion which is denoted as dispersion-induced power penalty (DIPP). In **Fig. 3.5**, the advantages of optical carrier suppression (DSB-CS) compared to conventional operation (DSB) for photonic mm-wave generation with respect to required LO frequency have already been exemplified. In addition, the carrier

suppression technique allows reduced effects of chromatic dispersion which is studied and compared with the conventional technique in the following. In order to evaluate the DIPP it is necessary to consider not only the optical mm-wave signal alone but together with applied data modulation.

Optical spectrum of a data-modulated DSB- and a DSB-CS signal

Fig. 3.13a shows a subsystem for creating a data-modulated photonic mm-wave signal using cascaded Mach-Zehnder modulators. Light from a laser diode (LD) is coupled to a first Mach-Zehnder modulator MZM-1. By applying a sinusoidal RF-signal a lower and an upper sideband are created exhibiting a frequency spacing of f_{LO} from the optical carrier. Subsequent

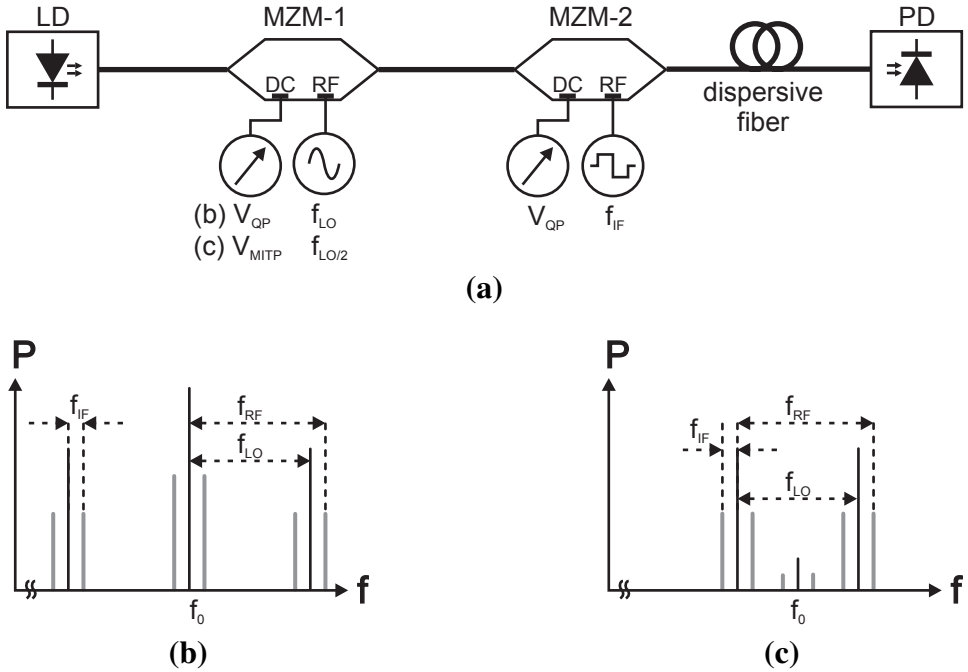

Figure 3.13: (a) Photonic mm-wave generation and data modulation using cascaded MZMs. Optical spectrum while applying (b) an RF frequency of f_{LO} to MZM-1 and DC-biasing to the QP and (c) an RF frequency of $f_{LO/2}$ and DC-biasing to the MITP. MZM-2 is biased to the QP and modulated with f_{IF} in both cases.

data modulation is accomplished with a second Mach-Zehnder modulator MZM-2 by adjusting DC-bias to the quadrature point and modulating with an electrical baseband data signal. To find an analytic description of the DIPP,

a frequency of f_{IF} is utilized here for data modulation, corresponding to the approximate bandwidth of the applied NRZ-signal, i.e. 10 GHz for a 10 Gb/s data signal. This corresponds to a worst-case scenario as only a fraction of the total data signal power is located near f_{IF} for the case of NRZ-modulation. As an example, a ratio of 0.75 times the data rate already comprises 93.6 % of the total signal power (further discussed in **4.2**). For the case of a DSB signal shown in **Fig. 3.13b** MZM-1 is biased to QP and modulated with a frequency of f_{LO}. Due to a different propagation speed of each spectral component the sidebands exhibit a relative phase shift related to the optical carrier. As both phase-shifted sidebands mix with the optical carrier during o/e-conversion, destructive interference may occur depending on the relative phase shift of carrier and sidebands. For the case of a DSB-CS signal shown in **Fig. 3.13c**, MZM-1 is biased to the MITP and modulated with a frequency of $f_{LO/2}$. While suppressing the carrier the sidebands solely mix with each other and power fading effects are severely reduced if the carrier suppression is sufficiently high. Thus, the optical carrier suppression technique exhibits an inherent tolerance to chromatic dispersion besides the reduced requirements for the LO source discussed in **3.1.1**.

Calculation of the DIPP for a DSB and a DSB-CS signal

The calculation of the DIPP for both cases is performed in the following for deducing a quantitative comparison of the dispersion properties. The impact of chromatic dispersion applying conventional DSB-modulation is given by [116, 154–157]. Firstly, the detected RF-photocurrent $i_{ph,RF}(t)$ after fiber-optic transmission is proportional to

$$i_{ph,RF}(t) \sim \cos\left[2\pi\left(f_{IF} + f_{LO}\right)t\right]\cos\left(\beta f_{LO} f_{RF}\right)\cos\left(\beta f_{IF} f_{RF}\right), \tag{3.16}$$

where f_{IF}, f_{RF} and f_{LO} correspond to intermediate frequency, radio frequency (i.e. $f_{LO} + f_{IF}$) and the local oscillator frequency f_{LO}, respectively. The factor β based upon **(3.15)** and [158, 159] is furthermore described as

$$\beta = \frac{\pi D L \lambda^2}{c}, \tag{3.17}$$

where L is the fiber length, D is the dispersion coefficient, λ is the wavelength and c is the speed of light. Considering **(3.16)**, the following relationship

can be deduced for the chromatic dispersion induced power penalty $DIPP_{DSB}$ in case of DSB-modulation, i.e. the logarithmized power reduction after propagating through a dispersive fiber:

$$DIPP_{DSB} = 20\log_{10}\left[\cos\left(\beta f_{LO} f_{RF}\right)\cos\left(\beta f_{IF} f_{RF}\right)\right] \tag{3.18}$$

$$= 20\log_{10}\left[\cos\left(\beta f_{RF}^2\right)\right] \qquad (f_{RF} \gg f_{IF}). \tag{3.19}$$

It is assumed that the photodetector is a perfect squarer, i.e. $P_{opt} \sim P_{el}^2$. If we further assume that $f_{RF} \gg f_{IF}$, the dominant term in **(3.18)** is $\cos\left(\beta f_{LO} f_{RF}\right)$ and as $f_{RF} \approx f_{LO}$ in this case, **(3.18)** can be rewritten to **(3.19)** [159]. Conversely considering the case of optical carrier suppression, the relationship between RF-photocurrent and dispersion-induced photonic mm-wave signal is described as [159]

$$i_{ph,RF}(t) \sim \cos\left[2\pi\left(f_{IF} + f_{LO}\right)t\right]\cos\left(\beta f_{IF} f_{RF}\right). \tag{3.20}$$

Using **(3.20)**, the power penalty for a DSB-signal with suppressed carrier can be described as [107, 154]

$$DIPP_{DSB,CS} = 20\log_{10}\left[\cos\left(\beta f_{IF} f_{RF}\right)\right]. \tag{3.21}$$

Comparing the expressions for power penalty in **(3.21)** and **(3.19)** shows the advantage of carrier suppression, as an f_{RF}-term is replaced by an f_{IF}-term. Accordingly, the fiber length which causes a 3 dB power penalty versus applied IF frequency (data rate) with and without carrier suppression is shown in **Fig. 3.14a**, assuming an LO-frequency of f_{LO} = 60 GHz. Here, a 3 dB power penalty is reached after some hundred meters with a comparatively low influence of data rate for the DSB-case. This is attributed to the beating of the optical sidebands with the carrier which dominates the dispersion properties in this case.

On the contrary, while applying carrier suppression (DSB-CS), the 3 dB power penalty is reached after several kilometers, strongly dependent on the data rate. The course of DIPP versus fiber length assuming an LO-frequency of f_{LO} = 60 GHz and different values for f_{IF} is depicted in **Fig. 3.14b**. The estimated fiber-optic transmission lengths for 12.5, 10.3125 and 1.25 Gb/s are 2.0, 2.5 and 23.9 km, respectively. Fiber lengths around 2 km may already be sufficient for application in optical access networks, however,

the maximum fiber length could be easily extended by implementing some dispersion compensation techniques as previously discussed. The results here give an estimation of minimum achievable fiber lengths. More accurate results may be achieved using numerical simulation tools. In conclusion,

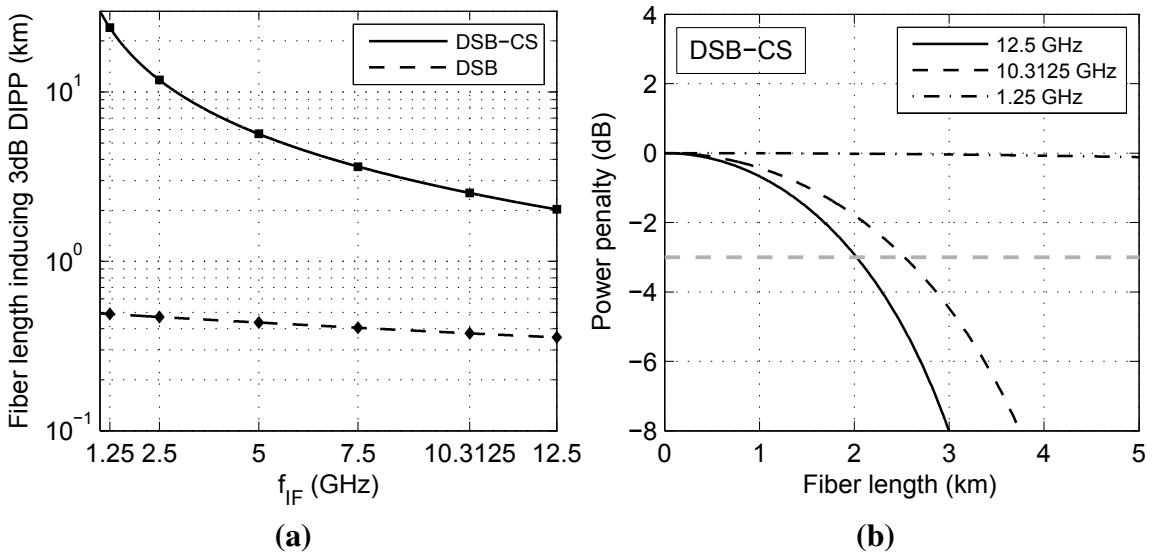

Figure 3.14: (a) Fiber length inducing a 3 dB DIPP versus f_{IF} for the DSB and the DSB-CS case. (b) DIPP versus fiber length for different values of f_{IF}. The LO frequency f_{LO} is 60 GHz in both cases and D is assumed to be 17 ps/(nm/km).

MZM cascading in conjunction with optical carrier suppression (DSB-CS) offers a significantly higher fiber-optic transmission span if compared to conventional DSB modulation while maintaining low system complexity.

3.3.2 Dispersion induced power penalty using a passive MLLD

Deducing the dispersion-induced power penalty for an MLLD is much more challenging due to the number of participating optical modes exhibiting different amplitudes as well (see **Fig. 3.9**). The photocurrent at fundamental beating frequency was introduced in **(2.10)**:

$$i_{ph,RF}(t) = \eta_{OE,RF} \sum_n E_n E_{n-1} \exp\left[j(2\pi n f_{ML} t + \phi_n - \phi_{n-1})\right].$$

While propagating through a dispersive fiber, each beat note exhibits another relative phase state. During o/e-conversion some of the beat notes are more

or less in phase and will participate to the RF signal where other notes are out of phase leading to destructive interference which lowers the generated signal power. A measurement of the power penalty versus applied fiber length

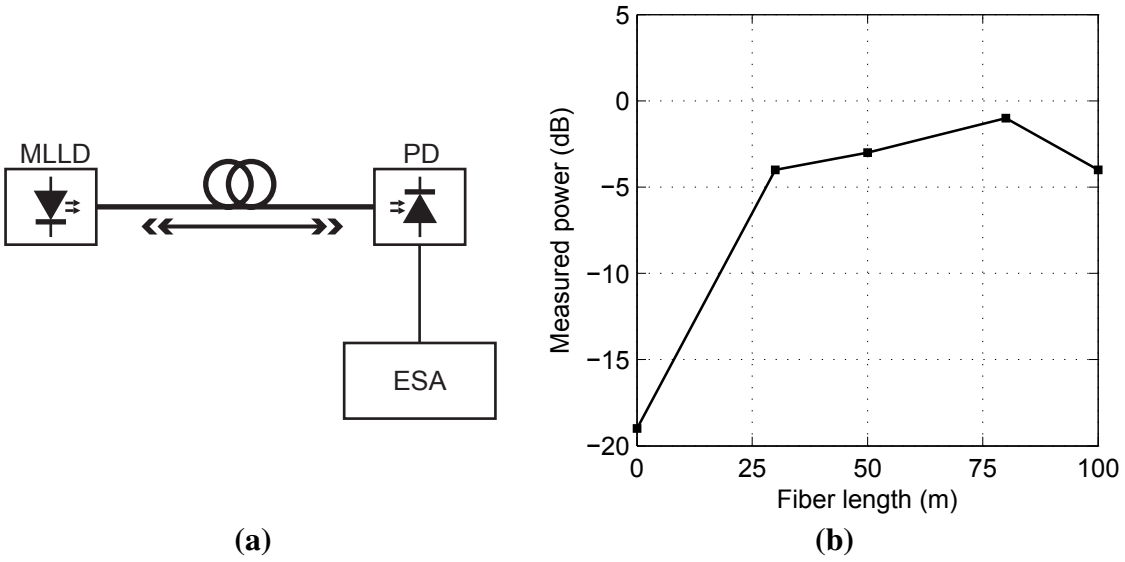

Figure 3.15: MLLD dispersion power penalty versus fiber-optic transmission length, showing the measurement setup in (a) and the results in (b) [160].

for the optical mm-wave carrier was performed by a project partner [160], applying different fiber lengths between the MLLD and the photodetector while measuring the o/e-converted power with an electrical spectrum analyzer (ESA) in conjunction with an external mixer (see **Fig. 3.15a**). The results are shown in **Fig. 3.15b**, indicating an optimum fiber length of 80 m which induces a power penalty of about 1 dB. The power penalty in the figure is attributed to the numerous optical modes with a large total consumed bandwidth resulting in a radically limited fiber-optic transmission range due to chromatic dispersion compared to the previous approach in **3.3.1**. The reason for this optimum not being located at a fiber-optic transmission length of zero is based upon the chirp generated by the MLLD itself [65, 101, 160].

As a conclusion, the MLLD is only applicable for short-range fiber-optic transmission but offers a concept for photonic mm-wave generation with extremely low complexity. In addition, larger fiber-optic spans could be achieved e.g. by applying an optical bandpass filter to remove some of the modes and further utilizing an EDFA to compensate the optical losses due to filtering.

3.4 Wireless radio-over-fiber transmitter

The wireless RoF transmitter consists of a photodetector with a specified bandwidth of 70 GHz to perform o/e-conversion, an optional amplifier to boost the electrical output signal and an antenna as shown in **Fig. 3.16**. The

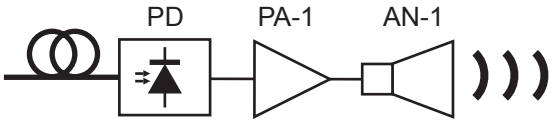

Figure 3.16: Wireless radio-over-fiber transmitter.

DC conversion efficiency of the photodetector $\eta_{OE,DC}$ is computed relatively to the conversion efficiency of an ideal photodetector $\eta_{OE,ref}$ as introduced in **(3.6)**. The equivalent RF conversion efficiency is further calculated by implementing the detector's frequency response:

$$\eta_{OE,DC} = \eta_{OE,ref}\,\eta \tag{3.22}$$

$$\eta_{OE,RF} = \eta_{OE,DC}\,R(f), \tag{3.23}$$

where $R(f)$ denotes a correction factor to consider the frequency response and η the quantum efficiency. With these information, the equivalent RF gain of the photodetector can be calculated as following:

$$G_{el} = \left(\frac{\eta_{OE,RF}}{\eta_{OE,ref}}\right)^2 \frac{Z_{out}}{Z_{ref}}, \tag{3.24}$$

where Z_{out} is the electrical output impedance of the photodetector. Later during the system experiments the transmitted RF power is controlled by an optical attenuator giving a wide optical input power range to the photodetector. It is therefore required to evaluate a regular quadratic detection behavior for the whole operational range. Determining the frequency response of the photodetector is a further point of interest as broadband data signals with bandwidths exceeding 20 GHz are o/e-converted. A measurement is performed to study these detector key characteristics.

The applied measurement setup in **Fig. 3.17a** consists of a dual-mode laser setup, a polarization controller to achieve identical polarization states of both optical modes, an optical coupler for combining the two modes and an

optical amplifier to boost the optical signal level. The o/e-converted signal was characterized by an ESA up to 50 GHz, while measurements of higher frequencies have been accomplished by the ESA together with external mixers. The characterization of electrical output power versus optical input power is

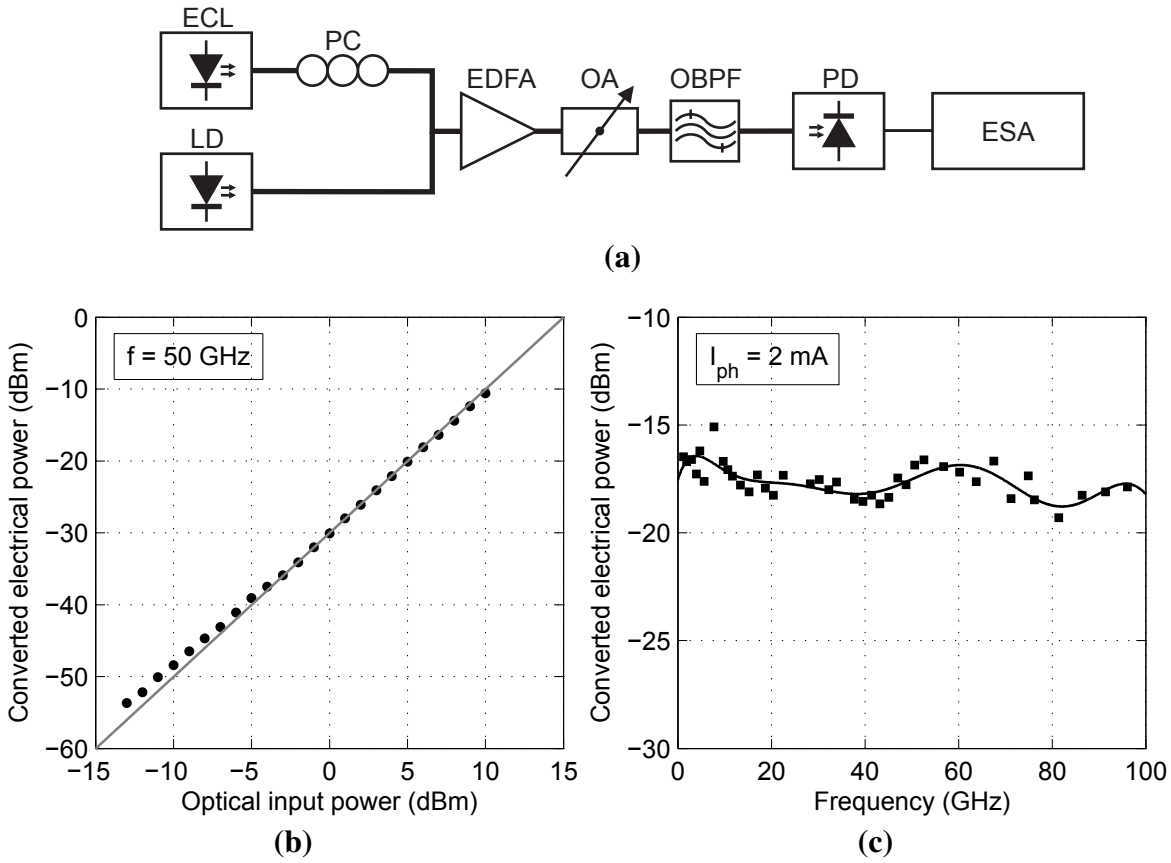

Figure 3.17: The measurement setup for determining key characteristics of the photodetector is given in (a). The o/e-converted electrical output power versus optical input power at 50 GHz is shown in (b) whereas (c) gives the frequency response of the photodetector at an optical input power of 8.1 dBm corresponding to a photocurrent of 2 mA.

given in **Fig. 3.17b**, applying an optical 50 GHz signal. The deviation from ideal behavior for optical input power levels below −5 dBm is based upon the applied resolution bandwidth of the spectrum analyzer. It was set large to integrate the whole signal power as the phase noise of a dual laser source is high, measuring not only the signal power but also a significant amount of noise power within the resolution bandwidth. Maximum applied optical input power during the experiments was limited to 10 dBm. Up to this value,

the detector exhibits a quadratic detection behavior, and no saturation effects can be noticed. The measured frequency response is shown in **Fig. 3.17c**. Here, an optical input power of 8.1 dBm resulting in a photocurrent of 2 mA was applied while adjusting the frequency within DC to 100 GHz. The DC responsivity can thus be calculated to $\eta_{OE,DC} = 0.32$ A/W. Within the frequency range of interest, i.e. 50–75 GHz, the output power is fluctuating within less than about 3 dB. Related to the DC responsivity, a loss of about 1 dB at 60 GHz gives an effective responsivity of 0.29 A/W for $\eta_{OE,RF}$ at the photodetector's output, supposing quadratic detection.

The applied RF-amplifier PA-1 is a waveguide-coupled broadband millimeter-wave amplifier with specified bandwidth, gain and noise figure of 50–70 GHz, 40 dB and 5 dB, respectively. Vector network analyzer measurements have been carried out using a V-band analyzer to obtain the S-parameters of the amplifier and to verify the specified bandwidth as well. The measured S_{21} of

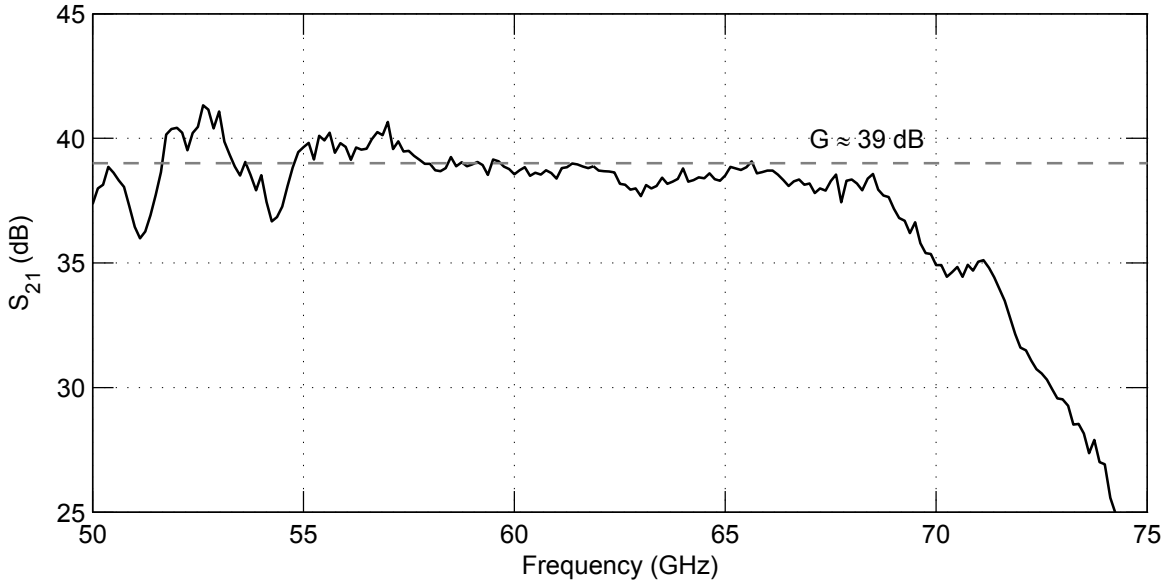

Figure 3.18: S_{21}-measurement of the applied transmit amplifier PA-1 within 50–75 GHz. The approximate gain is further indicated in the figure.

the amplifier is shown in **Fig. 3.18**, indicating a bandwidth of approximately 55–68 GHz and an average gain of 39 dB. After amplification, the signal is coupled to a waveguide horn antenna with a gain of 23 dBi and transmitted to free space.

3.5 Optical link noise contributions

Relevant noise sources and their influence on the system performance are discussed in this section. In the electrical domain it is comparatively easy to calculate the influence of a noisy component on the system. Here, it is typical to characterize a noise figure which allows a calculation of the generated noise power, especially for components at critical positions like a low-noise amplifier applied after wireless transmission.

In contrast, calculation of noise contributions of active devices is not as straight forward within the optical domain as the generated noise power is

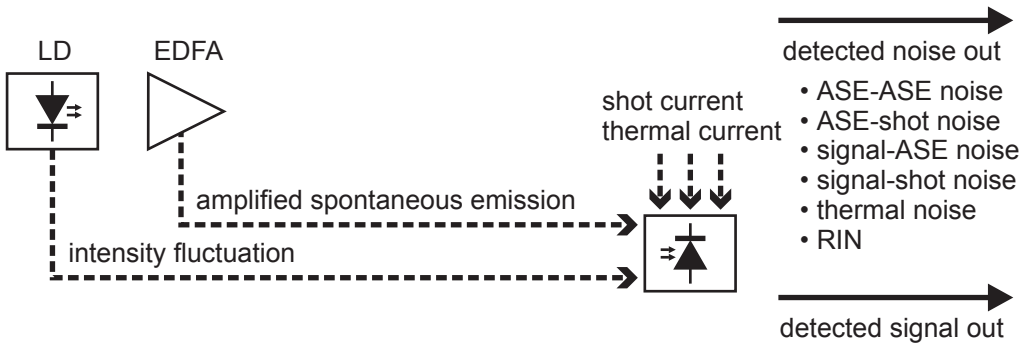

Figure 3.19: Noise contributions within the optical link.

strongly dependent on the operation point and further environmental conditions which will be discussed in the following. The relevant active optical and optoelectronic devices are shown in **Fig. 3.19**. Noise contributions are the relative intensity noise (RIN) caused by the laser, the amplified spontaneous emission (ASE) noise of the optical amplifiers, the thermal noise and the shot noise generated in the photodetector which all act together during o/e-conversion.

Fibers and optical adapters are treated as passive devices like corresponding electrical components (cables, waveguides and electrical adapters). The applied Mach-Zehnder modulators can be approximately treated as optical passive devices as well without any additional noise contributions besides the losses in the waveguides [142]. While considering the noise terms after photodetection as current sources which are ergodic, wide-sense stationary and independent from each other, the total noise power can be calculated by summing up each individual noise contribution [138].

3.5.1 Thermal noise

A pervasive noise contribution is the thermal noise (Johnson noise) describing power fluctuations across a circuit element caused by thermal motion of charge carriers. Thermal noise is modeled as a Gaussian process with a mean value of zero. The generated noise power is described as

$$N_{el,th} = \underbrace{\frac{4k_B B_{N,el} T}{Z_{out}}}_{\langle i_{th}^2(t)\rangle} Z_{ref} = k_B B_{N,el} T \;|_{Z_{out}=Z_{ref}}, \tag{3.25}$$

where k_B is the Boltzmann constant, $B_{N,el}$ the noise-equivalent electrical bandwidth, $\langle i_{th}^2(t)\rangle$ the variance of the thermal noise current and T the temperature. If circuit resistance Z_{out} and input resistance of the subsequent element Z_{ref} are matched together, solely half of the noise current is delivered to the next component which is further indicated in **(3.25)** [142]. The thermal noise power density exhibits a value of −174 dBm/Hz at 290 K. Supposing for example a 10 Gb/s signal with a value of $B_{N,el} = 10$ GHz, the total thermal noise power level would be −74 dBm in this case.

3.5.2 Photodetector shot noise

Shot noise originates from the fact that the incident light, i.e. the individual photons, arrive randomly distributed at the photodetector, thus generating a random fluctuation in the photocurrent. An additional contribution is given by the detector's dark current which flows through the bias circuitry in the absence of an optical input signal. It originates from thermally generated charge carriers in the junction as well as surface defects resulting in surface current flows. Shot noise is assumed to be Gaussian-distributed and can be calculated by [141, 143, 161]

$$N_{el,shot} = \underbrace{2eB_{N,el}\left(P_{opt,in}\eta_{OE,DC} + I_{dark}\right)}_{\langle i_{shot}^2(t)\rangle} Z_{ref}, \tag{3.26}$$

where I_{dark} denotes the dark current and $\langle i_{shot}^2(t)\rangle$ the variance of the shot noise induced current.

3.5.3 Laser relative intensity noise

Relative intensity noise originates from the laser source spontaneous emission resulting in random fluctuations of the optical power, thus evolving random fluctuations of the detected photocurrent. The term relative in RIN denotes that the noise power is normalized to the average laser output power. Other impairments and parasitic properties generated by the laser like wavelength stability, linewidth or side-mode suppression ratio are not critical due to the laser signal quality as well as the application scenario [162–165]. The optical signal composed by the desired continuous-wave output signal in conjunction with the undesired power fluctuation is described as

$$P_{opt,out}(t) = \overline{P_{opt,out}} + \Delta P_{opt,out}(t). \tag{3.27}$$

Typically, lasers are characterized with a logarithmic value for the RIN, i.e. the power spectral density is given in dB/Hz. The noise power due to RIN during o/e-conversion can be calculated by

$$N_{el,rin} = \underbrace{10^{\frac{RIN}{10}} B_{N,el}\, I_{ph}^2}_{\langle i_{rin}^2(t)\rangle} Z_{ref} = \underbrace{10^{\frac{RIN}{10}} B_{N,el} \left(P_{opt,in}\, \eta_{OE,DC}\right)^2}_{\langle i_{rin}^2(t)\rangle} Z_{ref}, \tag{3.28}$$

where I_{ph} is the generated average photocurrent, $\langle i_{rin}^2(t)\rangle$ the variance of the RIN-induced photocurrent and Z_{ref} the reference impedance. For further calculations on the link budget, the RIN noise is expressed by optical input power and responsivity instead of the generated photocurrent. This is further described in the equation above, where $P_{opt,in}$ denotes the optical input power applied to the photodetector and $\eta_{OE,DC}$ the photodetector's DC conversion efficiency.

3.5.4 Amplified spontaneous emission noise

The amplified spontaneous emission noise originates from the applied EDFAs, which do not only amplify the desired signal (stimulated emission) but also generate a significant amount of amplified spontaneous emission. An EDFA is described as a linear amplifier with an optical gain G_{opt} in conjunction with a Gaussian noise source due to amplified spontaneous emission (ASE) acting over the optical bandwidth of interest. The resulting optical noise

bandwidth is here determined by the gain spectrum of the EDFA which may be further limited by optical multiplexers or filters, as well as the responsivity of the photodetector at a certain wavelength. This leads to additional noise contributions, the detected noise due to ASE-ASE and signal-ASE beating as well as ASE-shot noise [166–168]. A direct measurable parameter of an EDFA is its optical noise figure NF_{opt}, which is given by [169]

$$NF_{opt} = \frac{2\rho_{sp}}{h\nu\, G_{opt}}, \tag{3.29}$$

where ρ_{sp} denotes the spontaneous power density, $h\nu = hc/\lambda$ the photon energy and G_{opt} the gain of the amplifier which is assumed to be $\gg 1$. Considering [166] and using **(3.29)**, the noise power due to ASE-ASE beating is described as

$$\begin{aligned} N_{el,ase-ase} &= \underbrace{4\,\eta_{OE,DC}^2\,\rho_{sp}^2 B_{N,opt} B_{N,el}}_{\langle i_{ase-ase}^2(t)\rangle} Z_{ref} \\ &= \underbrace{\left(\eta_{OE,DC}\, G_{opt} NF_{opt}\, h\nu\right)^2 B_{N,opt} B_{N,el}}_{\langle i_{ase-ase}^2(t)\rangle} Z_{ref}, \end{aligned} \tag{3.30}$$

where $\eta_{OE,DC}$ is the photodetector's DC-responsivity and $B_{N,opt}$ the optical bandwidth. The term $\langle i_{ase-ase}^2(t)\rangle$ denotes the variance of the noise current at the photodetector due to ASE-ASE beating. Using **(3.29)**, the generated noise power while the signal is beating with the ASE noise is further described as [166]

$$\begin{aligned} N_{el,sig-ase} &= \underbrace{4\,\eta_{OE,DC}^2\, G_{opt} P_{opt,in}\, \rho_{sp} B_{N,el}}_{\langle i_{sig-ase}^2(t)\rangle} Z_{ref} \\ &= \underbrace{2\left(\eta_{OE,DC}\, G_{opt}\right)^2 NF_{opt} P_{opt,in}\, h\nu B_{N,el}}_{\langle i_{sig-ase}^2(t)\rangle} Z_{ref}, \end{aligned} \tag{3.31}$$

where $\langle i_{sig-ase}^2(t)\rangle$ denotes the variance of the photocurrent induced by beating of the signal with ASE noise. Finally, by using **(3.29)**, the noise contribution due to ASE-shot noise is given by [166]

$$N_{el,ase-shot} = \underbrace{4\eta_{OE,DC}\, e\, \rho_{sp}\, B_{opt} B_{el}}_{\langle i_{ase-shot}^2(t)\rangle} Z_{ref}$$

$$= \underbrace{2\eta_{OE,DC}\, e\, G_{opt} NF_{opt}\, h\nu B_{opt} B_{el}}_{\langle i^2_{ase-shot}(t)\rangle} Z_{ref}, \tag{3.32}$$

where $\langle i^2_{ase-shot}(t)\rangle$ denotes the variance of the photocurrent induced by ASE-shot noise.

3.6 Wireless channel modeling

Modeling of the wireless channel is performed with respect to wireless path length, frequency as well as further environmental conditions. Three main contributors can be identified for computing the total path loss: the free-space path loss, the atmospheric gaseous attenuation and attenuation induced by rain fall.

Other effects only marginally contribute to the loss, like fog or mist [170–172], while other possible contributions are not applicable for terrestrial line-of-sight communication, like attenuation due to clouds [173].

3.6.1 Free space path loss

Calculation of the propagation losses of the wireless line-of-sight (LOS) link is performed by the free-space path loss model. The free-space path denotes a linear, lossless and isotropic propagation medium without any current sources and charges. Further on, permittivity and permeability are assumed to be equal to the vacuum.

However, for moderate-range propagation through the atmosphere, the simplification to the described free-space case is applicable in good approximation [170]. The relationship of received signal power $P_{el,RX}$ and transmitted power $P_{el,TX}$ for a wireless link is given by the Friis equation [174, 175]

$$P_{el,RX} = \frac{P_{el,TX}}{4\pi d^2} G_{el,TX} G_{el,RX} \frac{\lambda^2}{4\pi}, \tag{3.33}$$

where $G_{el,TX}$ and $G_{el,RX}$ denote the antenna gains of transmitter and receiver antenna, d the wireless path length and λ the wavelength of the radio signal.

This relationship is valid for a line-of-sight path with perfectly matched antennas. From **(3.33)**, the free-space path loss can be expressed as

$$L_{fs} = \frac{P_{el,TX}}{P_{el,RX}} G_{el,TX} G_{el,RX} = \left(\frac{4\pi d}{\lambda}\right)^2. \tag{3.34}$$

The free space path loss in **(3.34)** is quadratic-dependent on the frequency which is based upon a reduction of the effective area of the receiving antenna with rising frequency, thus reducing the effective received power. In **Fig. 3.20** the free-space path loss for 60 GHz and some further important frequencies are given as an example. Comparing e.g. conventional WLAN applications operating at 2.4 GHz with the frequency of interest in this work, the path loss

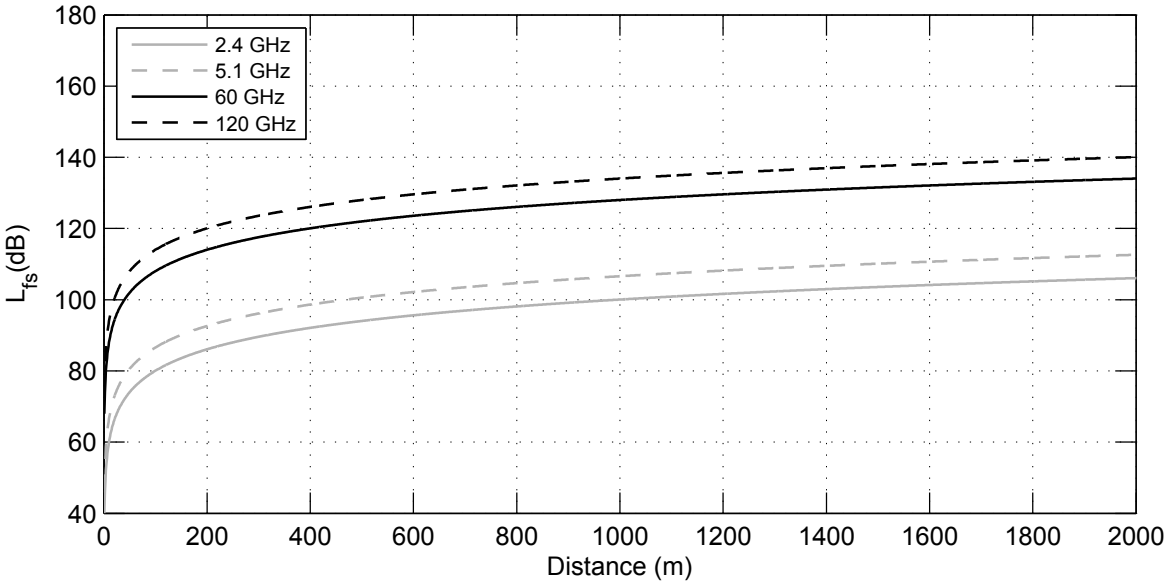

Figure 3.20: Free space path loss L_{fs} for 2.4, 5.1, 60 and 120 GHz.

is increased by a value of 28 dB. The free-space path loss assumption is only valid in the far-field denoted as Fraunhofer region when the transmitted signal can be described approximately as a plane wave. This distance of interest is calculated by [176, 177]

$$d_f \geq \frac{2D_A^2}{\lambda}, \tag{3.35}$$

where d_f is the Fraunhofer distance, D_A the largest antenna dimension and λ the wavelength. For the later applied V-band horn antennas with a gain of 23 dBi, the Fraunhofer distance is calculated to 1.95 m at a frequency of

60 GHz. As this formula describes the loss of an ideal line-of-sight path without obstacles and without any multipath propagation due to reflective surfaces, it is barely applicable for indoor communication over longer distances. Here, path loss can be e.g. modeled by the exponential-loss model, where the exponent is adapted to the corresponding environment like a corridor, hallway or open-plan office. However, good agreement with the free space path loss is given for wireless propagation over short LOS distances within a range of some meters [170, 175, 178, 179].

3.6.2 Atmospheric gaseous attenuation

While propagating through the atmosphere, an electromagnetic wave is attenuated by molecular absorption. The atmosphere comprises a large number of gases like N_2, CO_2, SO_2, H_2O, O_2, inert gases, particles as well as pollutants and many of them exhibit molecular absorption lines within the millimeter-wave range [170]. However, up to frequencies of about 350 GHz atmospheric gaseous absorption is almost exclusively caused by absorption lines of oxygen and water vapor. For all conventional microwave radio applications which are mainly operating below frequencies of 10 GHz, atmospheric gaseous attenuation L_{gas} is negligible in most cases. Other for the case of millimeter-wave communication where attenuation figures can exceed levels of some 10 dB/km [180–182].

Various experimental and theoretical studies have been carried out to quantify the atmospheric gaseous absorption in detail. Based upon this work, the ITU has developed and continuously improved a detailed model using several fit parameters for predicting the atmospheric gaseous losses within 1–350 GHz while further considering temperature dependence and pressure. For the calculations in this work ITU standard environmental conditions are applied, i.e. a temperature of 15 °C and a pressure of 1013 hPa. Furthermore, the ITU proposes a water vapor density of 7.5 g/m^3 which corresponds to a relative humidity of 58.7 % at 15 °C. The model is separated into two sections, one for dry air especially comprising the oxygen peaking around 60 GHz and a further one considering attenuation due to water vapor (see **Fig. 3.21**). The spectral attenuation in the figure is composed of several individual absorption peaks which are not visible at a pressure of 1013 hPa due to absorption line broadening [171]. With rising altitude (approximately 4 km and above)

the individual absorption lines get more and more observable, and as an example the spectrum within 54–66 GHz exhibits more than 20 significant absorption lines. This model allows a convenient description of atmospheric gaseous attenuation within the microwave- and millimeter-wave range, as the maximum error is specified with typically less than 0.7 dB around 60 GHz and 0.1 dB otherwise [181, 183]. **Fig. 3.21a** shows the spectral attenuation within

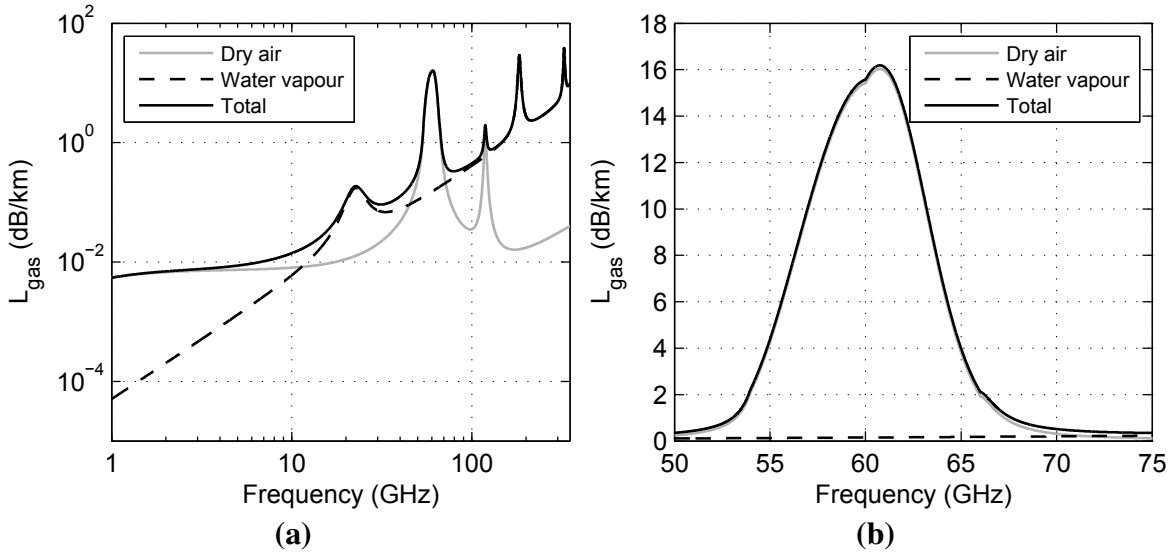

Figure 3.21: Specific attenuation due to atmospheric gases L_{gas} within a frequency range of (a) 1–350 GHz and (b) 50–75 GHz, applying ITU standard conditions of 15 °C, 1013 hPa and a water vapor density of 7.5 g/m^3.

1–350 GHz whereas in **Fig. 3.21b** the atmospheric gaseous attenuation within the V-band is plotted in detail. As can be seen, L_{gas} peaks at about 60.76 GHz with a value of 16.18 dB/km. This is more than 3 orders of magnitude higher than for example the corresponding attenuation at 2.4 GHz.

3.6.3 Rain attenuation and concept of availability

While losses due to free-space propagation and atmospheric gases can be predicted in a very accurate way, the situation gets more complicated for specific attenuation due to rain L_{rain}, which is mainly dependent on rain amount but also the size of rain drops. Especially forecasting the rain amount can be difficult even if large empiric datasets are available as e.g. in the case of subtropical and tropical regions within the rainy seasons [184–186]. **Fig. 3.22a**

shows the specific attenuation due to rain within 1–350 GHz for different rain amounts [187]. For most application cases, rain attenuation can be neglected for frequencies below 10 GHz. Higher frequencies in conjunction with sig-

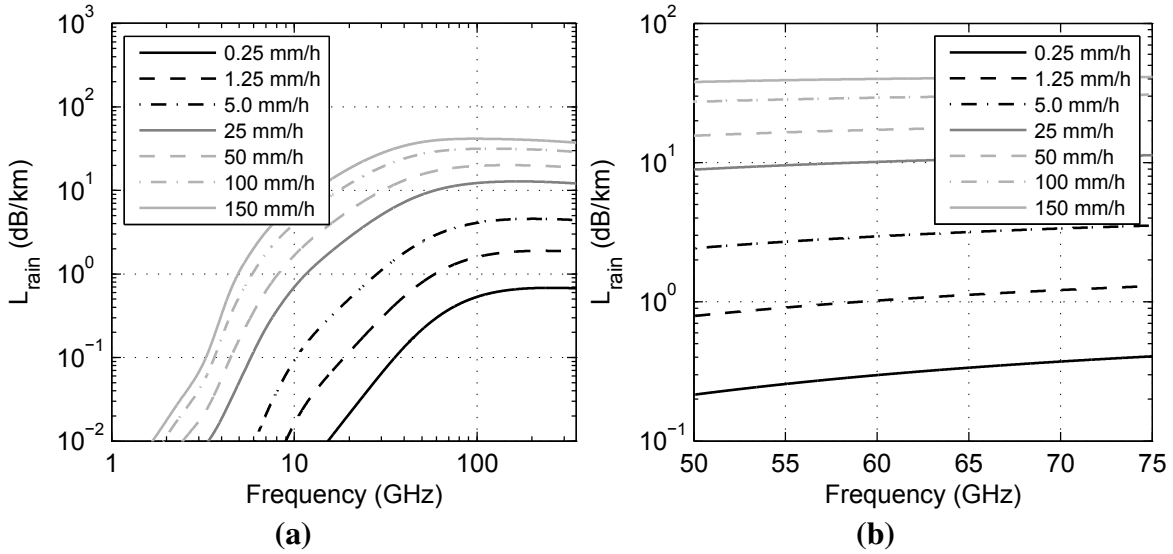

Figure 3.22: Specific attenuation caused by rain L_{rain} for different rain rates, (a) within 1–350 GHz and (b) within 50–75 GHz.

nificant rain amounts can cause severe additional attenuation, and a maximum is reached at around 100 GHz. The rain attenuation within a frequency range of 50–75 GHz is shown in **Fig. 3.22b** exhibiting comparatively flat characteristics. If wireless connectivity (i.e. link availability) must be maintained even for heavy downpour, the corresponding maximum attenuation has to be considered in the wireless power margin requiring e.g. higher transmit powers, receivers with better sensitivities or more directional antennas, leading to increased costs. However, an availability level of around 100 % is often not necessary and a specific amount of unavailability can be tolerated. To calculate the availability of a wireless system the annual rain distribution needs to be known for the geographic region of operation. **Tab. 3.1** shows the rain rate versus statistical incidence for various climate regions. As an example, within 1 % or 5260 min per year the rain rate is exceeding 1.9 mm/h in the climate region C. If the power budget of a wireless link is sufficient to compensate this corresponding rain attenuation, its availability level is 99 % in a yearly period. Typically requested availabilities are 99.999 % ('five-nines rule') for carrier-class links, whereas for campus connectivity and enterprise

applications, availabilities within 99 and 99.99 % are mostly considered to be sufficient [127]. The climate regions B, C, D, E, F correspond to moderate, maritime, continental, wet and arid weather, and many parts of e.g. Europe or

Table 3.1: Rain rates of different climate regions and availabilities.

Rain rate	Rain versus climate region (mm/h)							Rain rate
(% per year)	B	C	D1	D2	D3	E	F	(min. per year)
0.001	54	80	90	102	127	164	66	5.3
0.003	40	62	72	86	107	144	51	10.5
0.005	26	41	50	64	81	117	34	26.3
0.01	19	28	37	49	63	98	23	52.6
0.02	14	18	27	35	48	77	14	105
0.05	9.5	11	16	22	31	52	8.0	263
0.1	6.8	7.2	11	15	22	35	5.5	526
0.2	4.8	4.8	7.5	9.5	14	21	3.8	1052
0.5	2.7	2.8	4.0	5.2	7.0	8.5	2.4	2630
1	1.8	1.9	2.2	3.0	4.0	4.0	1.7	5260
2	1.2	1.2	1.3	1.8	2.5	2.0	1.1	10520

the U.S.A. are classified as continental weather zones. For further detailing continental weather three subcategories have been introduced, namely D1, D2 and D3 [186]. As an example, weather region D1 can be supposed for large parts of Germany. For the following calculations rain amounts corresponding to region D1 with 90 mm/h rain for 99.999 % availability level, 37 mm/h for 99.99 % availability and 2.2 mm/h for 99 % availability are chosen, corresponding to additional attenuations of 27.0, 13.7 and 1.6 dB/km, respectively.

3.6.4 Applied model for total path loss

The total path loss L_{path} is calculated by merging all individual contributions together, comprising the free-space path loss, the atmospheric gaseous attenuation as well as the attenuation due to rain:

$$L_{path} = L_{fs} + L_{gas} + L_{rain}. \tag{3.36}$$

Fig. 3.23a shows the total path loss per km for fair weather and rain amounts of 2.2, 37 and 90 mm/h within a frequency range of 1–350 GHz. **Fig. 3.23b** illustrates the total path loss L_{path} for various wireless path lengths and a rain rate of 37 mm/h within a frequency range of 50–75 GHz. As can be seen, the spectral attenuation for 50 and 100 m is comparatively flat with

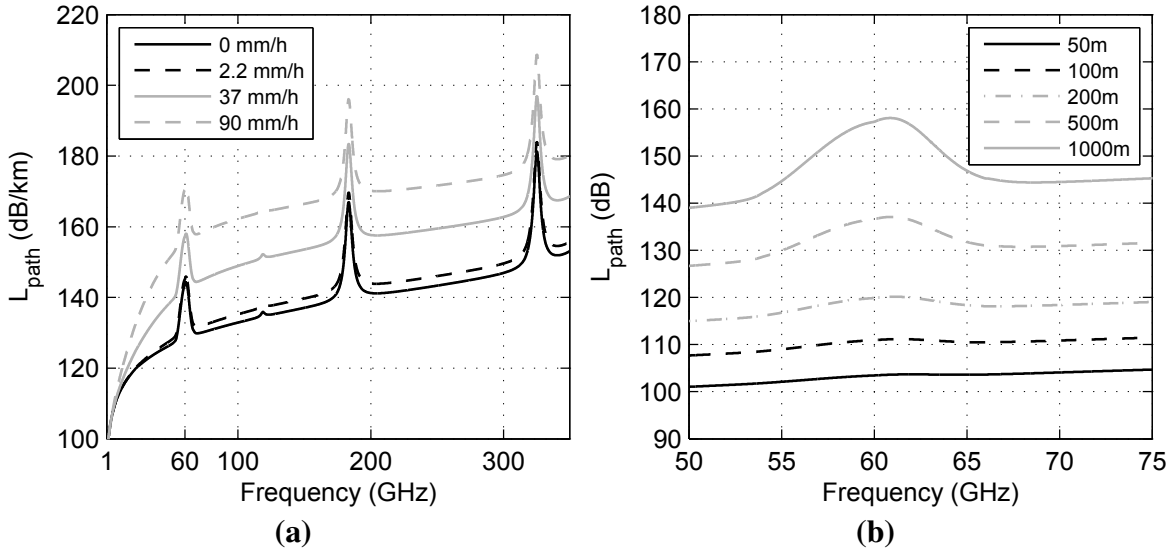

Figure 3.23: Total spectral path loss L_{path} within 1–350 GHz and different rain amounts is given in (a), whereas (b) shows L_{path} within a frequency range of 50–75 GHz for different wireless path lengths and a rain rate of 37 mm/h.

around 3 dB fluctuation and total attenuation figures of approximately 104 and 111 dB at 60 GHz, respectively. For larger wireless path lengths, the impact of atmospheric gaseous attenuation becomes more and more severe leading to strong variations in spectral attenuation. This can be especially difficult for single-carrier modulation schemes with more amplitude levels like e.g. 4-QAM or 16-QAM in conjunction with a large consumed bandwidth. In this work, a binary amplitude modulation scheme is applied which is thus more tolerant to spectral attenuation impairments. Anyway, large wireless path lengths in conjunction with large consumed bandwidths are challenging for single-carrier modulation techniques applied. This can be countered by using multicarrier modulation like OFDM as reported in [O33]. As each data-modulated subcarrier only consumes a fraction of the total signal bandwidth, the varying channel attenuation can be partially equalized if the received signal quality with respect to SNR is sufficiently high.

3.7 Wireless receiver

After wireless transmission the signal is received at the wireless receiver. In this work, two different architectures have been developed. The first receiver

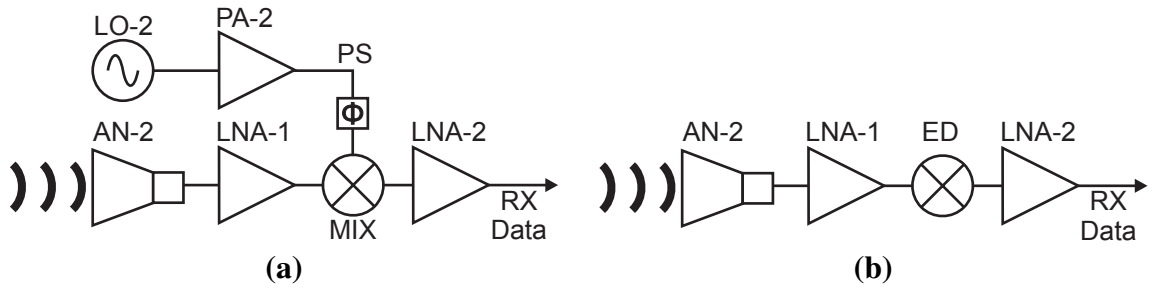

Figure 3.24: Wireless receiver architecture using (a) coherent and (b) incoherent detection.

shown in **Fig. 3.24a** is a coherent receiver, thus requiring information about the phase state of the received signal. After signal reception with a 23 dBi horn antenna the signal is amplified by a waveguide-coupled RF amplifier (LNA-1). For down-conversion, a 60 GHz signal source LO-2 is applied and further

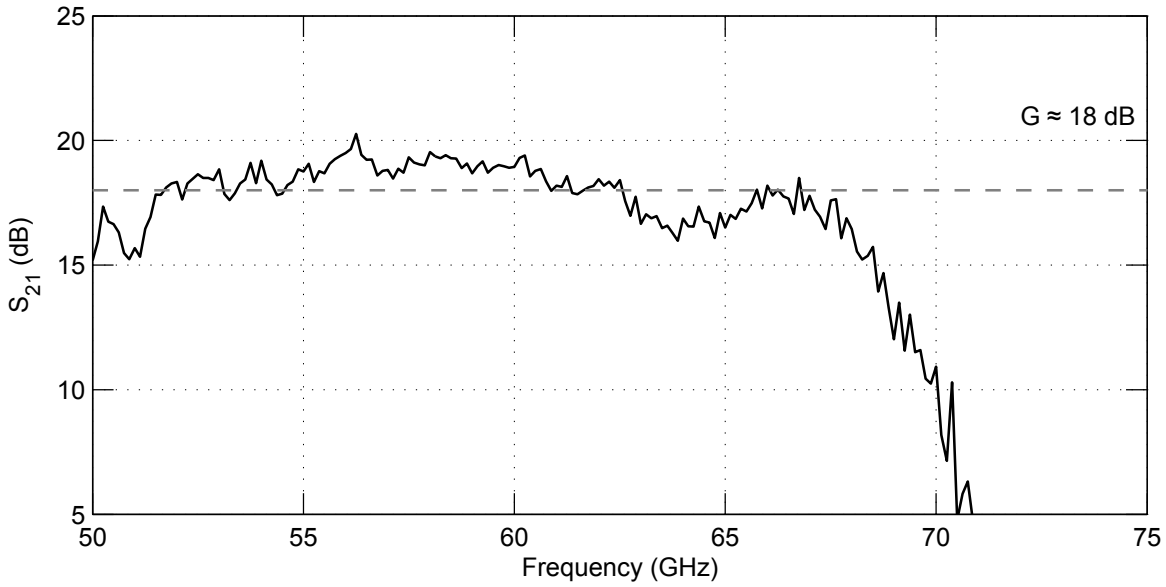

Figure 3.25: S_{21}-measurement of the applied receiver amplifier LNA-1 within 50–75 GHz. The approximate gain is further indicated in the figure.

amplified by PA-2 to boost the LO signal power to 13 dBm. Both LO and RF signals are further coupled to a broadband custom-design low-loss mixer to perform the downconversion, which requires a phase locking of both signals

together. The utilized mixer exhibits specified RF, LO and IF bandwidths of 55–72.5 GHz, 55–60 GHz and DC–12.5 GHz, respectively. Typically, a phase locked loop is applied in such receiver architectures requiring electronic components like phase comparators and phase shifters. However, to achieve phase-locking in the experiments, a locking functionality of the LO sources LO-1 and LO-2 is utilized. A 10 MHz reference signal from LO-1 is coupled to a synchronization input of LO-2 to lock both phases together. After down-conversion the signal is further amplified by a broadband baseband amplifier LNA-2 to compensate conversion losses and to support a sufficiently high signal power required for BER analysis. The applied RF-amplifier LNA-1 is specified with a noise figure of 3.5 dB. Gain and bandwidth are further specified with 16 dB and 55–65 GHz, respectively. Analog to the case of the RF amplifier PA-1 applied in the wireless transmitter, vector network analyzer measurements have been carried out to determine the amplifier's performance. The measured S_{21} of the amplifier indicates a bandwidth of $\approx$ 52–68 GHz and an average gain of 18 dB shown in **Fig. 3.25**.

Conversely, the architecture shown in **Fig. 3.24b** applies incoherent detection without the need of phase detection. After amplification in LNA-1 the signal is coupled to an envelope detector. Due to the limited video bandwidth of

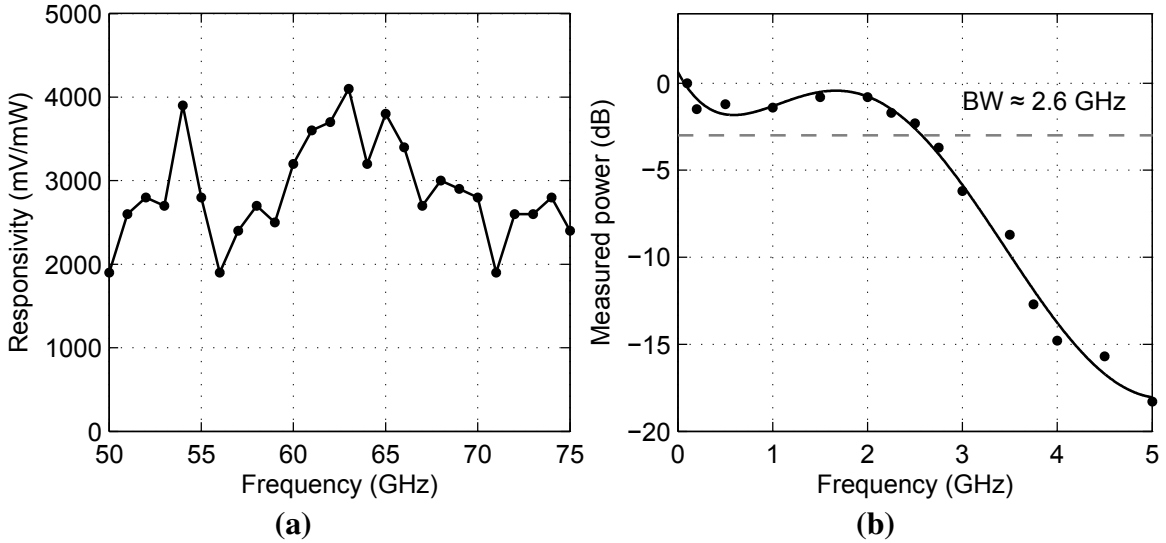

Figure 3.26: Characterization of the envelope detector showing the frequency response in (a) and the video bandwidth in (b) applying an RF carrier frequency of 55.4 GHz.

the detector the mm-wave carrier is not visible for the Schottky detector, and

solely the desired signal envelope (i.e. the data) is recovered. Identical to the first architecture, the baseband signal is coupled to LNA-2 to increase the signal level for loss compensation necessary for performing BER analysis. The applied WR15 envelope detector is a full-custom design Schottky detector whose RF response within the V-band is shown in **Fig. 3.26a**. As can be seen, the spectral response fluctuates within a value of 2000 to 4000 mV/mW, which corresponds to a power fluctuation of approximately 6 dB. Experiments have been carried out applying a data-modulated mm-wave carrier to the detector while altering the LO frequency for photonic mm-wave generation and measuring the eye diagram at the video output of the detector. The measurements showed that the received eye quality is strongly dependent on the RF carrier frequency, giving e.g. a degraded eye diagram at 60.0 GHz but operating well at other carrier frequencies as e.g. 55.4, 57.5 and 59.1 GHz. Besides the fluctuating spectral response, resonances in the RF circuitry are assumed to cause this behavior. In a next step, the video bandwidth was measured by applying an IF-frequency modulated RF-carrier at a frequency of 55.4 GHz which is shown in **Fig. 3.26b**, giving a value of approximately 2.6 GHz.

3.8 Conclusion

Subsystems for photonic mm-wave generation, photonic data modulation, photonic-wireless transmission and radio reception – further used in the developed RoF systems – have been described, experimentally characterized and modeled. Both fiber-optic and wireless channel with their impairments have been studied as well. Further on, relevant optical noise contributions have been described and modeled. The results achieved in this chapter allow to deduce a theoretical system description accomplished in **4** to predict the signal quality within an RoF system. This allows to verify the experimental results and to optimize the system performance of the realized RoF systems in **5**–**7** as well. The model will further be used for predicting system properties in **5**, where experimental data was not accessible.

4

Simulation environment

This chapter describes a system model for the developed RoF systems in **5**–**7** carried out in Matlab®. Based upon the results in **3**, electrical and optical subsystems are implemented to a simulation environment where the deduced noise sources will be integrated as well. A link budget model has been developed comprising signal and noise power calculation, thus the signal-to-noise ratio (SNR) at relevant points within the system can be predicted. Based upon the SNR, the bit-error-rate (BER) can be derived to evaluate the transmission quality. By further implementing the properties of wireless and fiber-optic channel which have been previously studied in **3**, sample wireless and photonic transmission simulations will be carried out and discussed.

Two main objectives are pursued with the model. Firstly, the simulation environment will be used for comparing experimental with theoretical results for verification issues. Secondly, prediction of specific system properties will be accomplished using the developed model in those cases where experimental data is not accessible, e.g. for predicting the possible wireless transmission range of the developed RoF system in **5**, if antennas with higher gain are utilized.

4.1 Component description and implementation

For clarification, electrical parameters will be designated by an *el*-subscript and optical parameters with an *opt*-subscript, respectively. Further on, linear values will be designated by a *lin*-subscript and logarithmic values with a *dB*-subscript. Each electrical component in the budget link will be characterized by an electrical gain G_{el} and a noise figure NF_{el}. Incorporating the output power of the previous component thus the actual input power to the observed component allows the calculation of the signal power level P_{el} and the noise power level N_{el}. Starting with the signal power, the output power $P_{el,out}$ with respect to the input power $P_{el,in}$ is calculated by

$$P_{el,out,dB} = P_{el,in,dB} + G_{el,dB}. \tag{4.1}$$

Output noise power of a component is calculated by considering input noise power $N_{el,in,lin}$, gain $G_{el,lin}$ and component noise figure $NF_{el,lin}$

$$N_{el,out,lin} = G_{el,lin} \left\{ N_{el,in,lin} + \left[\left(NF_{el,lin} - 1 \right) T_0 \, k_B \, B_{N,el} \right] \right\}, \tag{4.2}$$

where T_0 is the reference temperature, k_B the Boltzmann constant and $B_{N,el}$ the electrical receiver noise bandwidth. Based upon signal output and noise output power, the SNR is calculated by

$$SNR_{el,dB} = P_{el,out,dB} - N_{el,out,dB}. \tag{4.3}$$

The source code for calculating the electrical link budget is shown in **Lis. 4.1**.

After the calculation of output power, noise power and SNR the values are written to a table for visualization. The link budget calculation in the electrical domain for components is straight forward, as the noise contributions of a component are more or less operating-point independent and the noise figure is typically given for critical elements like low-noise amplifiers.

A sample link budget table is shown in **Tab. 4.1**, assuming a 1 GbE signal which is modulated on a 60 GHz carrier, wirelessly transmitted and down-converted to baseband.

Signal power and SNR are set to values of −26 dBm and 50 dB while assuming a noise-equivalent bandwidth of 1.25 GHz. The signal is further amplified by

```
function [Budget,SIG]=ESysBudget(GlobalV,SIG,Name,Comment,G_dB,NF_dB)
% General parameters
  kb=1.38e-23;T0=GlobalV.T0;B=GlobalV.B;
% Signal power level at output
  SIG.P_dBm=SIG.P_dBm+G_dB;
% Noise power level at output
  G=dB2plin(G_dB);
  NF=dB2plin(NF_dB);
  Nin=dBm2W(SIG.N_dBm);
  Nout=G*(Nin+((NF-1)*T0*kb*B));
  SIG.N_dBm=W2dBm(Nout);
% SNR at output (dB)
  SNR_dB=SIG.P_dBm-SIG.N_dBm;
% Link budget table
  Budget={...
  Name, Comment,...              % component ID, comment
  G_dB, NF_dB,...                % el. gain, el. noise figure
  SIG.P_dBm, SIG.N_dBm,...       % el. signal power, el. noise power
  SNR_dB,...                     % el. SNR
  SIG.Gopt_dB, SIG.Popt_dBm}     % opt. gain, opt. power
```

Listing 4.1: Matlab® source code for calculating the electrical link budget.

PA-1, coupled to a 23 dBi transmit antenna AN-1 and wirelessly transmitted over a span of 50 m. For the wireless transmission, the calculated values are given in terms of an equivalent isotropic radiated power (EIRP) to incorporate the gain of transmitter and receiver antenna while considering the propagation loss in the wireless channel. The noise figure of an antenna is calculated by

$$NF_{antenna} = 10\log_{10}\left(\frac{T_a}{T_0}+1\right). \tag{4.4}$$

For calculating the link budget the critical component where the signal is attenuated most is during reception by the receiver antenna where an antenna noise temperature of 290 K can be assumed regarding applied frequency and antenna directivity [188]. This would correspond to a noise figure of 3.01 dB. However, for a consistent description, i.e. by allowing the utilization of the previously mentioned m-function in **Lis. 4.1**, an effective noise figure is modeled while considering the antenna gain. Thus, **(4.4)** is modified to $10\log_{10}(T_a/T_0G_{el,lin}+1)$ to calculate the noise power with **(4.2)**. For the wireless propagation an ideal rainless scenario under free-space path loss conditions is assumed while neglecting the atmospheric attenuation due to its insignificance for this transmission span. The path loss of ≈ 102 dB attenuates

the signal close to thermal noise floor and the SNR is reduced to a value of 39.44 dB after reception. Finally, the signal is down-converted by MIX and amplified by LNA-2 with a remaining SNR of 29.67.

Table 4.1: Example link budget table for wireless 1.25 Gb/s transmission at 60 GHz, followed by down-conversion and amplification.

ID	Comment	G_{el} (dB)	NF_{el} (dB)	P_{el} (dBm)	N_{el} (dBm)	SNR_{el} (dB)
TX	1 GbE @ 60 GHz	-	-	−26.00	−76.00	50.00
PA-1		39.00	5.00	13.00	−35.44	48.44
AN-1	EIRP	23.00	-	36.00	−12.44	48.44
FSPL 50 m	EIRP	−101.98	-	−65.98	−114.43	48.44
AN-2		23.00	0.0217	−42.98	−82.42	39.44
MIX		−7.50	7.50	−50.48	−82.89	32.41
LNA-2		35.50	2.80	−14.98	−44.65	29.67

For the optical link, the calculation of optical signal power is performed analogous to the electrical power

$$P_{opt,out,dB} = P_{opt,in,dB} + G_{opt,dB}, \tag{4.5}$$

where G_{opt} is the optical gain and $P_{opt,in}$ and $P_{opt,out}$ are the optical signal input and output power levels, respectively. Assuming quadratic detection of the photodetector, the relationship between electrical gain G_{el} and optical gain G_{opt} can be written as

$$G_{el,dB} = 2G_{opt,dB}. \tag{4.6}$$

The implementation of optical noise sources and their influence on signal quality is different and more challenging, as most of the components are typically not deployed with a noise figure and the generated noise is furthermore strongly dependent upon the operating point. The corresponding optical noise contributions deduced in **3** are calculated and superimposed while assuming statistical independence [142].

A sample link budget for an optical link is shown in **Tab. 4.2**, assuming a 1 GbE electrical signal which is e/o-converted using a Mach-Zehnder modulator (MZM-2), fiber-optically transmitted, amplified with an erbium-doped

fiber amplifier (EDFA-2) and o/e-converted by a photodetector (PD). Optical noise sources are considered after o/e-conversion. Values of 1562 nm, 200 GHz and 1.25 GHz are supposed for optical wavelength, noise-equivalent optical bandwidth and noise-equivalent electrical bandwidth, respectively. Besides thermal noise, further noise contributions originating from photode-

Table 4.2: Example link budget table for fiber-optic 1.25 Gb/s transmission with an additional EDFA.

ID	Comment	G_{el} (dB)	NF_{el} (dB)	P_{el} (dBm)	N_{el} (dBm)	SNR_{el} (dB)	G_{opt} (dB)	P_{opt} (dBm)
ECL		-	-	-	-	-	-	3.00
TX	1 GbE	-	-	10.00	−40.00	50.00	-	-
MZM-2	$\eta_{EO,RF} = 0.0054$	−43.01	-	−33.01	−83.01	50.00	−5.80	−2.80
EDFA-2		25.60	-	−7.41	−57.41	50.00	12.80	10.00
PD	$\eta_{OE,RF} = 0.29$	−13.20	-	−20.62	−70.62	50.00	-	-
$>N_{el,shot}$	−71.9 dBm	-	11.40	−20.62	−68.22	47.60		**(3.26)**
$>N_{el,rin}$	−56.9 dBm	-	26.08	−20.62	−56.63	36.01		**(3.28)**
$>N_{el,ase-shot}$	−110.7 dBm	-	0.0073	−20.62	−56.63	36.01		**(3.32)**
$>N_{el,ase-ase}$	−102.6 dBm	-	0.048	−20.62	−56.63	36.01		**(3.30)**
$>N_{el,sig-ase}$	−60.7 dBm	-	22.29	−20.62	−55.20	34.59		**(3.31)**

tector, laser source and optical amplifier are considered. These are shot noise $N_{el,shot}$, the laser intensity noise $N_{el,rin}$ as well as $N_{el,ase-shot}$, $N_{el,ase-ase}$ and $N_{el,sig-ase}$ from the EDFA. The calculated noise figures of the optical sources are related to the total thermal noise power with a noise bandwidth of 1.25 GHz, identical to electrical components. In general, the SNR is reduced from 50 to 34.59 dB in this sample scenario after fiber-optical transmission and back-conversion. Largest noise contributor is the RIN noise, followed by signal-ASE noise as well as shot noise.

The source code for calculating the generated shot noise during o/e-conversion is shown in **Lis. 4.2** as an example. Calculation of the shot noise is accomplished by considering various parameters like signal bandwidth or generated photocurrent and written to a link budget table for visualization. The optical link budget is calculated similar to **Lis. 4.1** with an additional parameter for the optical gain.

```
function [SIG,OSS,Budget] = O_Noise_Shot(GlobalV,SIG,OSS,varargin)
 Name='>Shot';
% General parameters
  e=1.60e-19;kb=1.38e-23;T0=GlobalV.T0;B=GlobalV.B;
% Parameters from PD
  Zout=OSS.OEConv_Zout;
  nOEdc=OSS.OEConv_nOEdc;
  PPDin=dBm2W(OSS.OEConv_Pin_dBm);
% Update of parameters given in function call
  if nargin~=0
      for ii=1:2:length(varargin)-1;
          eval([varargin{ii},'=varargin{',num2str(ii+1),'};']);
      end
  end
% Calculate shot noise
  Ns      = 2*e*B*(PPDin*nOEdc)*Zout;
  Comment = ['Ns=',num2str(W2dBm(Ns),'%2.1f'),'dBm '];
% Calculate NF
  Nin   = kb*T0*B;       % thermal noise
  NF    = (Ns+Nin)/Nin;  % lin NF
  NF_dB = plin2dB(NF);   % log NF
% Output
  [Budget,SIG] = ESysBudget(GlobalV,SIG,Name,Comment,G_dB,NF_dB);
```

Listing 4.2: Matlab® source code for calculating the shot noise generated by the photodetector.

4.2 Applied test signal and error statistics

This section describes the applied modulation scheme non-return to zero on-off-keying (NRZ-OOK). Parameters of interest are the error statistics while considering coherent and incoherent detection and the consumed bandwidth at a given data rate. For the case of a transmitted 1-bit, the signal exhibits an amplitude of A and correspondingly an amplitude of $-A$ for the case of a transmitted 0-bit. Considering a duty cycle of 50 %, each bit exhibits a unique time slot with a duration of T_B, denoted as bit period.

For the experiments, a pseudo-random bit sequence is applied which means that all possible bit transitions appear randomly distributed. The term pseudo indicates that the signal is not really a random signal, but repeated after a data word with n transitions. However, the applied PRBS word length of $2^{31}-1$ in conjunction with the employed signal bandwidths allows an extremely even channel utilization. While considering autocorrelation and Fourier transform of an ideal rectangular signal with an infinite small rise and fall time, the

power spectral density of an NRZ-PRBS signal is given by [189, 190]

$$PSD_{NRZ} = A^2 T_B \ \mathrm{si}^2\left(\frac{\omega T_B}{2}\right), \tag{4.7}$$

where $\mathrm{si}(x) = \sin(x)/x$. As the rectangular pulses are assumed to be ideal, i.e. with a rise and fall-time of zero, the PSD is infinitely broad. The normal-

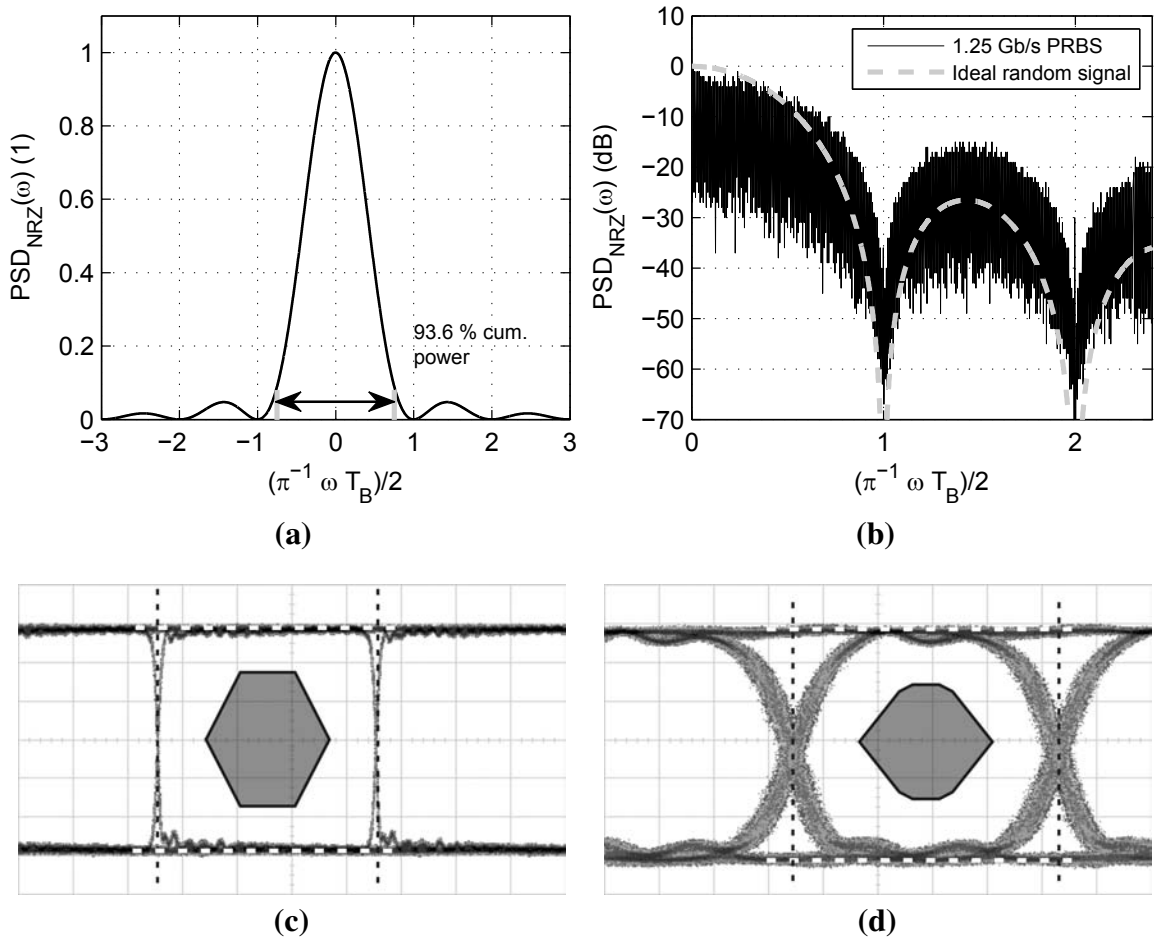

Figure 4.1: (a) Double sideband PSD of a random NRZ signal linearly scaled. (b) Logarithmically scaled single sideband PSD of a random NRZ-signal, compared with a measured 1.25 Gb/s PRBS signal. The PRBS transmit eyes for 1.25 Gb/s and 10.3125 Gb/s are shown in (c) and (d) with further indicated eye masks as defined in [82].

ized PSD of a random NRZ-signal is shown in **Fig. 4.1a**, indicating that most of the signal energy is located within the lower-frequency part of the signal. At a ratio of 0.75 times the data rate, already 93.6 % of the signal energy is

integrated. For channel quality analysis a pseudo-random binary sequence with a word length of $2^{31}-1$ was chosen for all the experiments. **Fig. 4.1b** shows the logarithmic-scaled spectrum of an ideal NRZ-PRBS signal, and a measured signal for a word length of $2^{31}-1$ at 1.25 Gb/s normalized to the approximation, i.e. 1 corresponds to 1.25 GHz. It can be seen that the real measured signal is not fully congruent with the theoretical spectrum as rise and fall times are not infinitely small. However, the fact that most of the energy is located within the lower-frequency part becomes evident. The 1.25 Gb/s and 10.3125 Gb/s transmit eyes of the applied test signal are shown in **Fig. 4.1c** and **Fig. 4.1d**. Minimum required eye openings for 1 and 10 GbE as defined by the IEEE are further indicated in the figure [82]. Based upon knowledge on modulation scheme and detection technique, the error statistics of a pseudo-randomly distributed signal can be calculated. As discussed in **3.7**, both coherent and incoherent detection are used in this work. Detection of a signal is in general processed in two steps. Firstly, the received signal at the sampling point, typically in the middle of a bit period T_B, has to be reduced to a numerical value. Secondly, this value has to be compared with a reference signal to decide which original signal was received, typically using a sensitive comparator. If the received signal is higher than the reference voltage, a 1-state is interpreted and vice-versa for a received signal lower than the reference voltage a 0-state. For the case of coherent detection while supposing predominantly Gaussian noise sources, the 0-state and the 1-state are Gaussian-distributed as well. As the antiderivative cannot be described in a closed form for the density function of 0- and 1-state, the Gaussian error function is applied, which is given by

$$\mathrm{erf}(z) = \frac{2}{\sqrt{\pi}} \int_0^z e^{-u^2} du. \tag{4.8}$$

Probability calculation of a wrong decision can be realized with the complementary error function

$$\mathrm{erfc}(z) = 1 - \mathrm{erf}(z). \tag{4.9}$$

With **(4.9)**, the bit error rate for the case of coherent detection is expressed as [190]

$$BER_{coherent} = \frac{1}{2}\,\mathrm{erfc}(z)\left(\sqrt{\frac{E_B}{2N_0}}\right), \tag{4.10}$$

where E_B is the energy per bit and N_0 the noise power spectral density; thus the term E_B/N_0 denotes a normalized signal-to-noise ratio. In contrary, for the case of incoherent detection, both signal states are no longer Gaussian-distributed but exhibit a Rician distribution for the 1-state and a Rayleigh distribution for the 0-state. The error statistics is here described as [191]

$$BER_{incoherent} = \frac{1}{2}\exp\left(-\frac{1}{2}\frac{E_B}{N_0}\right). \tag{4.11}$$

In the simulation, the SNR is deduced by the fraction of signal power P_{el} and noise power N_{el} as described in **(4.3)**. The energy per bit E_B is calculated by signal power divided by the bit rate, i.e. P_{el}/R_{bit}, whereas the bit rate is described by the spectral efficiency b multiplied with the bandwidth B_{el}, i.e. $R_{bit} = B_{el}\,b$. The noise power spectral density is calculated by the fraction of total noise power N_{el} divided by the bandwidth B_{el}. Thus, the relationship between SNR and E_B/N_0 is given by [192]

$$\frac{E_B}{N_0} = \frac{SNR_{el}}{b}, \tag{4.12}$$

where the single-sided spectral efficiency at the detector in the case of an NRZ-OOK signal is 1 b/s/Hz. Using the relationship between BER and

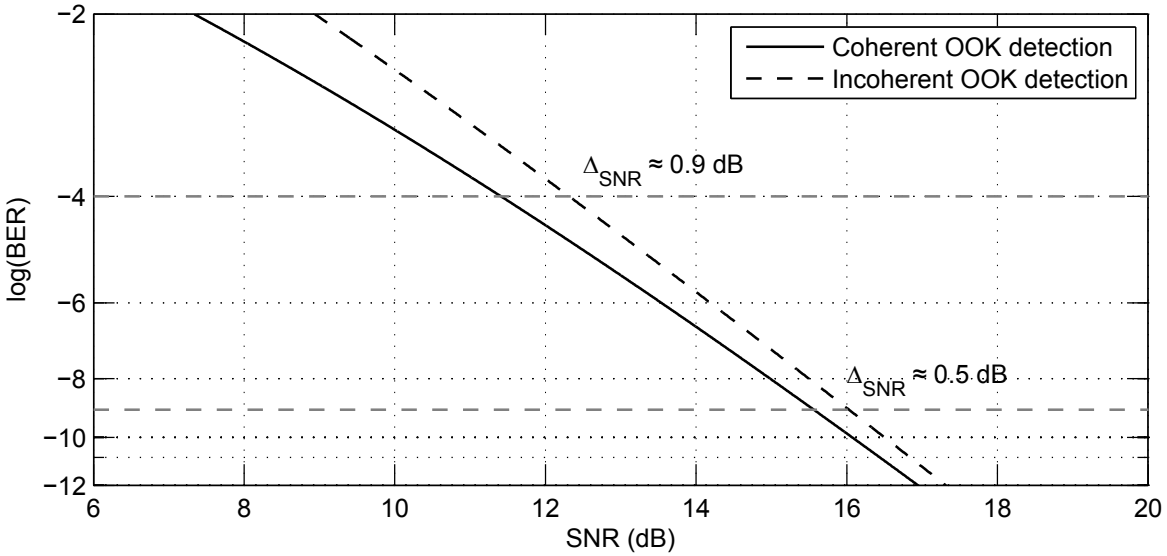

Figure 4.2: BER curves for coherent and incoherent detection schemes.

SNR in **(4.12)** for coherent and incoherent detection, the BER is deduced

from the calculated SNR. The theoretical BER is further compared with the experimentally achieved BER values during system characterization. Both cases are plotted in **Fig. 4.2**, requiring an SNR of 15.55 dB to achieve a BER of 10^{-9} for coherent detection and 16.03 dB for incoherent detection, respectively. Thus, an SNR penalty of about 0.48 dB has to be taken into account while applying incoherent detection. Supposing besides thermal noise an ideal, noiseless NRZ-modulated 10 Gb/s signal, the noise power would exhibit a value of approximately −74 dBm for a noise bandwidth of 10 GHz. In this case, the required signal powers to achieve a BER of 10^{-9} would be approximately −58.5 and −58 dBm for coherent and incoherent detection, respectively. The majority of lightwave communication systems specify a BER of below than 10^{-9} or 10^{-12} for operation, some of them even less than 10^{-15}. However, it is often not possible to achieve such low error rates at the receiver due to system design or economical reasons. In this case, forward error correction codes are applied to reduce the raw BER to the required level, like e.g. implemented to commercial 10 GbE transceivers [143].

5

Experimental RoF system based upon external modulation and coherent detection

This chapter discusses a 60 GHz RoF system based upon the system description in **3** by further utilizing the system link budget model detailed in **4**. Major aim of this system is to demonstrate wireless and fiber-optic transmission for point-to-point connections supporting 10 GbE-compatible data rates. The applied subsystems are

- 60 GHz DSB-CS carrier generation based upon external modulation,
- broadband NRZ data modulation using an external modulator,
- conversion and wireless transmission using an RoF transmitter,
- a wireless receiver using coherent detection.

The structure of the system is discussed in **5.1**, followed by the achieved experimental results in **5.2**. Simulations on the system link budget contrasted with experimental results are carried out in **5.3**. The system's potential for

extending the wireless range by further utilizing the developed model is discussed in **5.4**, followed by a conclusion in **5.5**.

5.1 System setup

The configuration of the developed system is shown in **Fig. 5.1**. For optical mm-wave carrier generation, light from an external cavity laser source at a wavelength of $\lambda_0 = 1562.25$ nm is coupled to an EDFA for optical amplification up to a value of 17 dBm to increase the modulation efficiency of the following Mach-Zehnder modulator MZM-1. A polarization controller is implemented to properly adjust the polarization state of the light incident to the modulator, thus minimizing the polarization dependent losses. DC-Bias is set to minimum transmission point MITP with respect to f_0 for achieving carrier suppression. A 30 GHz RF signal with a modulation power of 14.6 dBm is applied to create the two optical sidebands with a total frequency difference of $f_{LO} = 60$ GHz. Under these conditions the optical carrier suppression is sufficiently high and exhibits a value of about 25 dB.

The 60 GHz photonic millimeter-wave carrier is further modulated at MZM-2 with NRZ-OOK data. A second polarization controller (PC-2) is implemented to adjust the polarization state of the incident light to the modulator. The NRZ-OOK data signal is generated by a pulse pattern generator (PPG) with a maximum output voltage of 2 V_{pp} delivering a PRBS with a word length of $2^{31}-1$. DC-Bias of the modulator is set to the quadrature point. In conjunction with the applied maximum power of the modulating signal, a quasi-linear modulation is achieved with low signal distortion.

The data modulated mm-wave signal is amplified by an erbium amplifier (EDFA-2) to compensate the modulation losses of MZM-1 and MZM-2. The following optical band-pass filter is applied within the system to limit the cumulated amount of ASE noise as well as to remove harmonics during photonic millimeter-wave generation which would otherwise generate unwanted beat notes at the photodetector. The optical attenuator is used for controlling the o/e-converted signal after photodetection and thus the later received power within the wireless receiver to allow BER characterization. For a comparability of the experimental results EDFA-2 is always operated at 15.5 dBm optical output power, and the required signal power is adjusted

with the optical attenuator. After fiber-optic transmission to the wireless RoF transmitter via a standard single mode fiber (SMF-28) the optical mm-wave

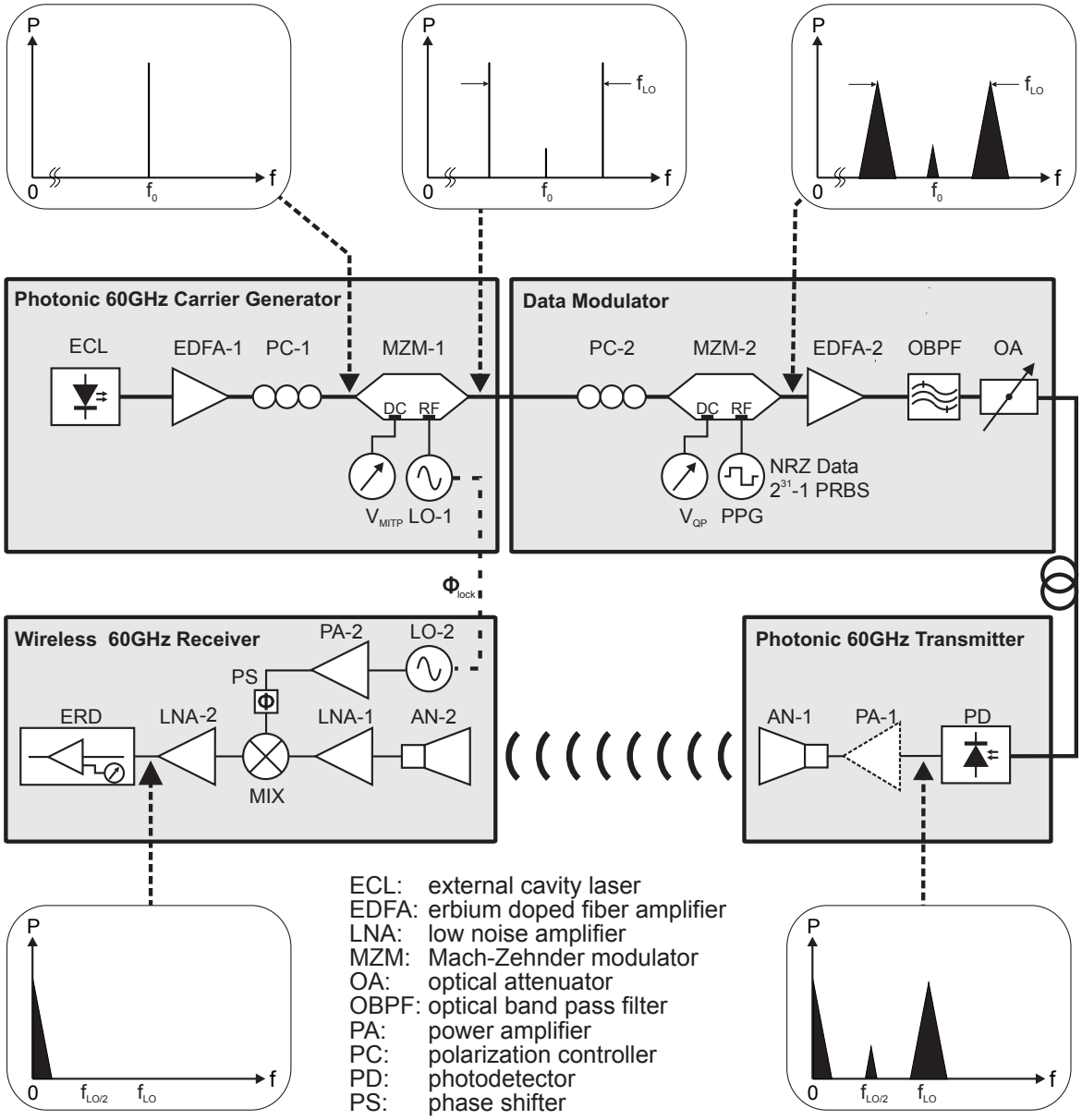

Figure 5.1: System setup showing the photonic 60 GHz carrier generator with subsequent broadband data modulation using external modulators, the photonic transmitter and the wireless receiver.

signal is o/e-converted by a broadband photodetector. Further on, the electrical signal is amplified by PA-1 which delivers a maximum RF output power of ≈ 10 dBm at 1 dB compression, coupled to a 23 dBi horn antenna and

transmitted. Signal detection is performed in the coherent wireless receiver. After reception by an identical 23 dBi gain horn antenna and amplification by a low-noise amplifier (LNA-1) the signal is down-converted to baseband. A 60 GHz RF source (LO-2) is amplified by PA-2 to a power level of 16 dBm and applied to the mixer's LO input. Phase locking between the received RF signal and the LO signal is achieved by utilizing a locking functionality of LO-1 and LO-2 described in **3.7**. A phase shifter (PS) is implemented to minimize the phase difference between RF- and LO-signal. After down-conversion to baseband and amplification with LNA-2, error-detection (ERD) can be performed to evaluate the system properties.

5.2 Experimental results

This section describes the achieved experimental results for photonic-wireless data transmission of up to 12.5 Gb/s. Indoor measurements within a laboratory environment have been performed, setting fiber-optic transmission span and wireless path length to 50 and 2.5 m, respectively. BER characterizations have been carried out without and with RF transmit amplifier PA-1. In the first case, the system's suitability for in-house communication scenarios was studied, the required wireless path lengths being within a range of about 5–10 m. The second case with included transmit amplifier allows to bridge increased wireless path lengths, corresponding experimental results act as a base for the outdoor experiments performed afterwards. Further on, indoor measurements were carried out to evaluate the fiber-optic transmission span the system can accommodate at a 10 GbE compatible data rate, concluding with a characterization of the system linearity. This is followed by outdoor measurements with a constant fiber-optic transmission length of 50 m and wireless path lengths of 25 and 50 m, performed with data rates of up to 12.5 Gb/s.

5.2.1 Indoor – 2.5 m wireless transmission length

Indoor experiments within a laboratory environment have been accomplished where the wireless transmitter and receiver were placed at a height of 120 cm over ground and separated to a distance of 2.5 m to get a reference measurement for further characterizations. The wireless span in conjunction with a

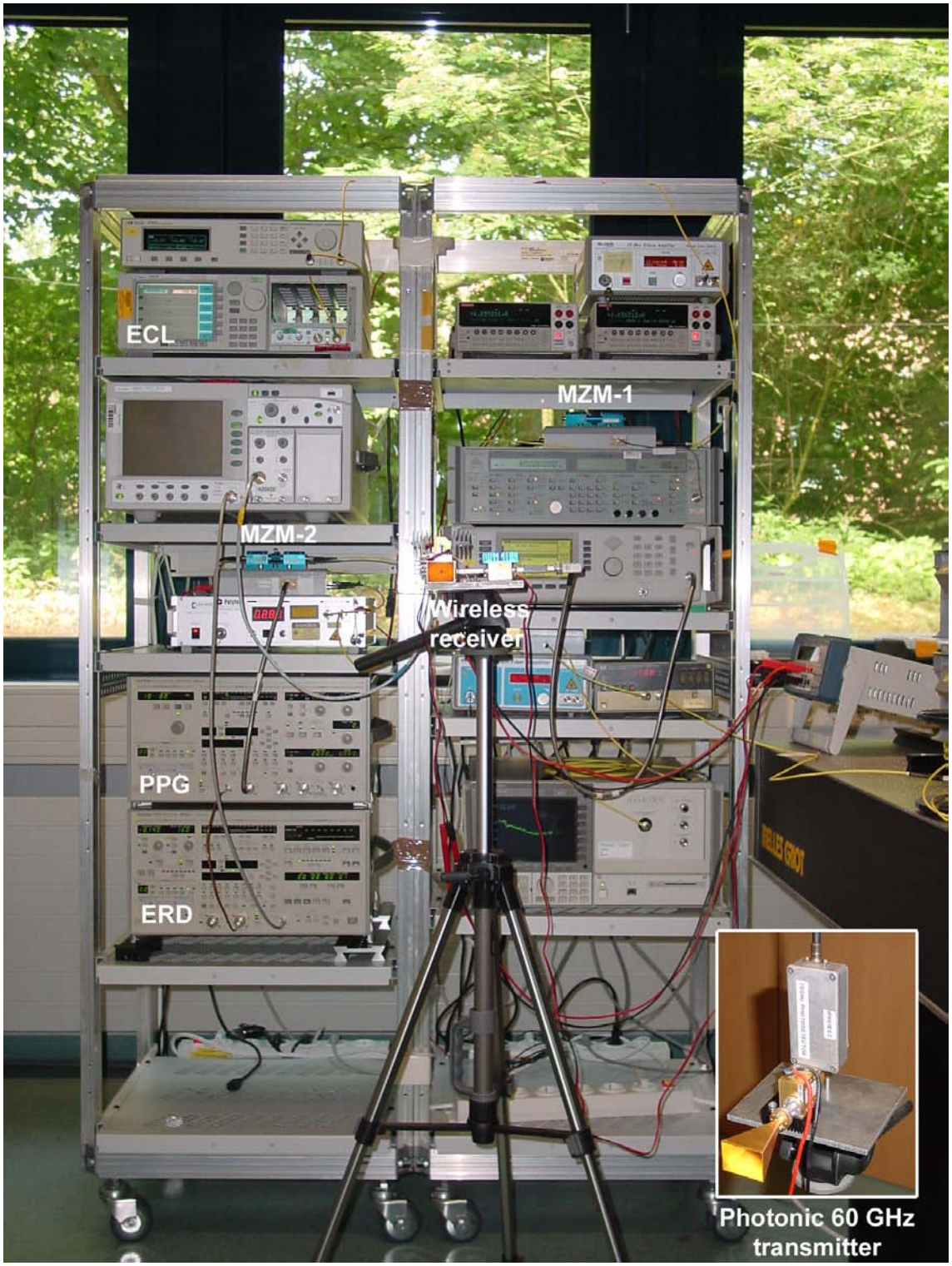

Figure 5.2: Photograph of the system showing photonic mm-wave generation with subsequent data modulation and the wireless receiver. The wireless RoF transmitter is further shown in the inset.

high antenna directivity of 23 dBi ensured a minimum of multi-path propagation for this reference measurement which would otherwise have affected the measurement results. A photograph of the measurement setup is shown in **Fig. 5.2**, comprising photonic mm-wave generation with subsequent data modulation, the wireless transmitter and the wireless receiver. Measurement devices like a sampling oscilloscope or an optical spectrum analyzer are further observable in the photograph.

BER characterizations at different data rates have been carried out, i.e. from 1.25 Gb/s compatible to 1 GbE up to 10.3125 and 12.5 Gb/s for 10 GbE. In a first case, the system was operated without transmit amplifier and thus with reduced maximum transmit power, aiming for communication over very short distances like e.g. within an open-plan office. For the second case, PA-1 was implemented in the wireless RoF transmitter for an increased output power and therefore higher wireless transmission distances. The corresponding BER curves are shown in **Fig. 5.3**. For the case of no transmit amplifier shown in **Fig. 5.3a**, the sensitivities for 1.25, 2.5, 5.0, 7.5, 10.3125 and 12.5 Gb/s are −56.7, −56.5, −56.4, −55.7, −51.1 and −43.4 dBm, respectively. No error-floor can be observed for a BER down to 10^{-9}. The BER curves for an operation of up to 5 Gb/s are nearly congruent. This is based upon the fact that the receiver noise bandwidth (i.e. the ERD) remained the same for all data rates during characterization and no additional filter has been applied here between LNA-2 and ERD. Higher data rates of 7.5, 10.3125 and 12.5 Gb/s cause power penalties of 1.2, 5.3 and 13.0 dB related to the sensitivity for 5 Gb/s-operation. This is partially attributed to the bandwidth insufficiency of the RX amplifier LNA-1, among other components like the mixer MIX (see **3.7**). The corresponding frequency response was introduced in **Fig. 3.25**, indicating an approximate operational frequency range of 52–68 GHz, i.e. a bandwidth of about 16 GHz which is insufficient for 10.3125 and 12.5 Gb/s DSB operation.

This is even more given for the case with TX amplifier exhibiting an operational frequency range of approximately 55–68 GHz (see **Fig. 3.18**). As shown in **Fig. 5.3b**, the sensitivities of up to 10.3125 Gb/s are −49.6, −49.6, −48.8, −48.5 and −44.0 dBm, respectively. The BER curve for 12.5 Gb/s-operation shows an error floor at a BER of about 10^{-7}, giving a best value of $3.4 \cdot 10^{-7}$. The 10.3125 Gb/s curve tends to an error floor of below 10^{-9}. Comparing the results in **Fig. 5.3b** with **Fig. 5.3a**, the overall sensitivities

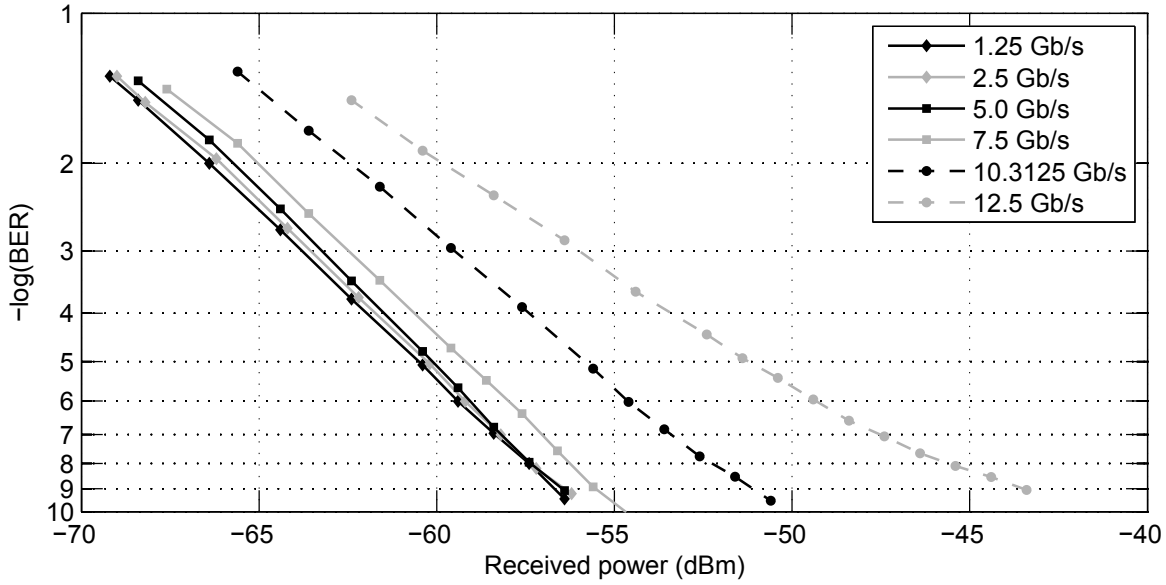

(a) without PA-1

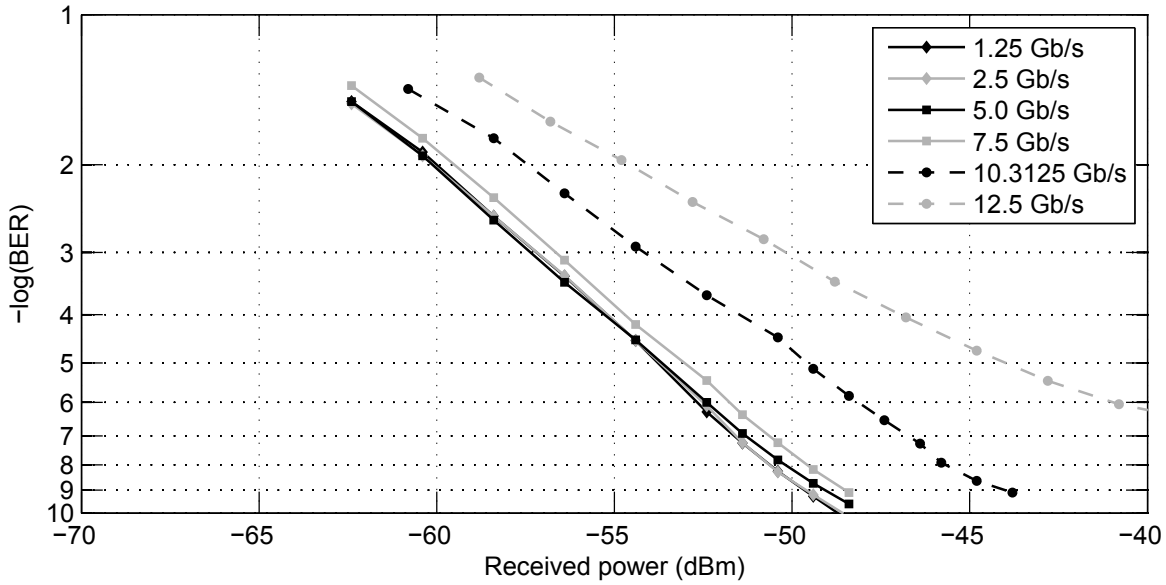

(b) with PA-1

Figure 5.3: Indoor BER measurements for a wireless path length of 2.5 m and a fiber-optic transmission span of 50 m at various data rates.

are considerably decreased by a value of about 6 dB while applying the TX amplifier within the system. To compensate the amplifier's gain of 39 dB, the optical input power to the photodetector was reduced accordingly by the optical attenuator. As a consequence, the signal power after photodetection is very close to the noise floor. Considering the low electrical input power

to PA-1 and its noise contribution as well ($NF_{el} = 5$ dB, see **3.4**), the SNR is severely reduced after amplification, which consequently limits the system sensitivity. This is further discussed in the next section where the experimental characterization is compared with the simulated system. The error-floors

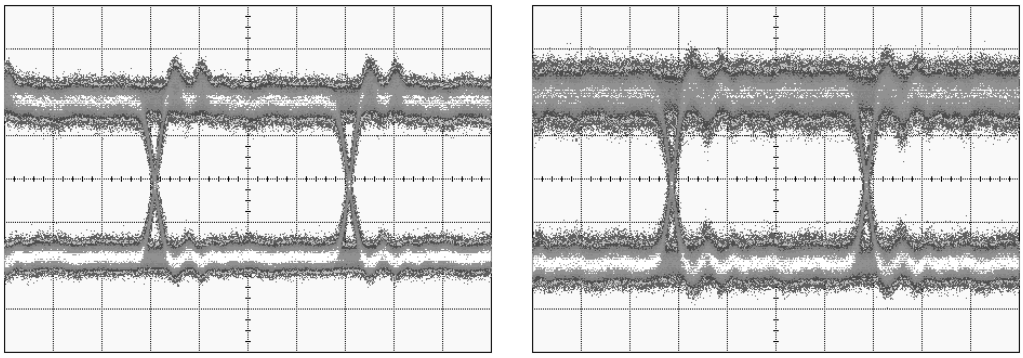

(a) 1.25 Gb/s, without TX amplifier, 100 mV/div, 200 ps/div

(b) 1.25 Gb/s, with TX amplifier, 100 mV/div, 200 ps/div

(c) 10.3125 Gb/s, without TX amplifier, 100 mV/div, 15.5 ps/div

(d) 10.3125 Gb/s, with TX amplifier, 100 mV/div, 20.0 ps/div

Figure 5.4: Eye diagrams measured at a received power of ≈ −45 dBm for 1.25 and 10.3125 Gb/s photonic-wireless transmission.

for 10.3125 and 12.5 Gb/s-operation on the other side are mainly attributed to the combined bandwidth insufficiency of both RF amplifiers on the TX side, as well as on the RX side. To give a qualitative evaluation of this behavior, eye diagram measurements have been performed shown in **Fig. 5.4**. Here, 1.25 and 10.3125 Gb/s eyes are confronted for both cases. Apparently, the noise amplitudes for the 1- and the 0-state are clearly higher with additional amplifier and exhibit roughly a doubled value, which corresponds to an increase in noise power of 6 dB. The bandwidth insufficiency is further observable from the eye diagram. For the 10.3125 Gb/s eye, the 10 to 90 % rise and fall time

is significantly increased. The corresponding values without amplifier are approximately 56 and 59 ps, respectively. With amplifier, rise and fall time exhibit values of approximately 68 and 69 ps.

A further point of interest is the remaining power budget for each BER curve, and the question which maximum indoor path length could be realized to meet a BER value of below 10^{-9}. To calculate this, the free-space path loss model was utilized as discussed in **3.6**, giving a sufficient approximation for LOS indoor propagation over small distances. Atmospheric gaseous and rain attenuation are neglected due to their insignificance. As can be seen

Table 5.1: Maximum possible indoor path lengths considering the remaining power budget to achieve a BER of 10^{-9}.

Data rate (Gb/s)	Remaining power budget (dB)	Estimated indoor range (m)
1.25	12.7	10.8
2.5	12.5	10.6
5.0	12.3	10.3
7.5	10.0	7.9
10.3125	7.8	6.1
12.5	1.5	3.0

from **Tab. 5.1**, wireless path lengths of more than 10 m can be predicted for data rates of up to 5 Gb/s while distance is reduced to 3.0 m for 12.5 Gb/s data transmission. These results do not take multi-path propagation into account, which is a limiting factor for broadband wireless communication, especially applicable within indoor environments due to many reflective objects and obstacles. However, former experiments performed within a corridor of the department with a similar setup and 20 dBi antennas instead of 23 dBi antennas have revealed a possible wireless path length of about 8 m at 12.5 Gb/s and 13 m at 7.5 Gb/s for a BER of 10^{-4} while higher path lengths resulted in severe effects of multi-path propagation [O13].

A further measurement was carried out to determine the maximum fiber-optic transmission length the system can accommodate. BER characterizations have been accomplished at a data rate of 10.3125 Gb/s while altering the fiber length between data modulator and wireless RoF transmitter of up to 6 km.

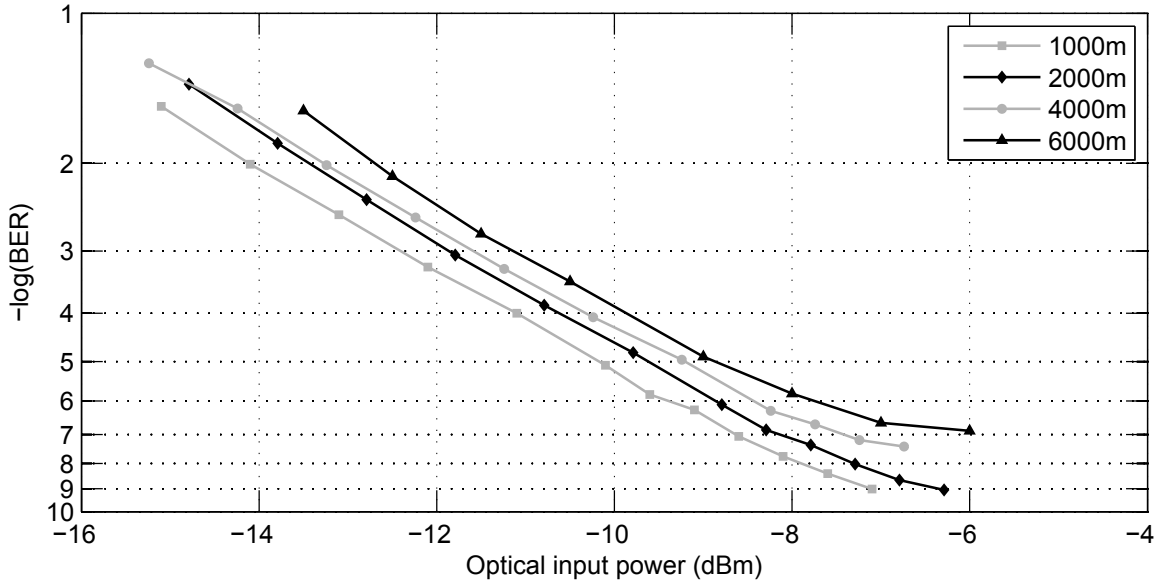

(a) BER characterization

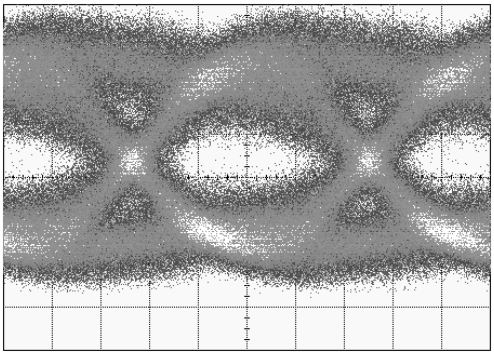

(b) 1000 m, 100 mV/div, 20.0 ps/div

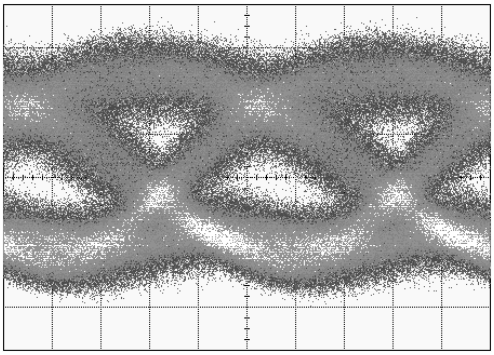

(c) 6000 m, 100 mV/div, 20.0 ps/div

Figure 5.5: BER measurements at 2.5 m wireless path length, a data rate of 10.3125 Gb/s and various fiber-optic transmission lengths are shown in (a). Corresponding eye diagram characterizations after 1000 and 6000 m fiber-optic transmission are given in (b) and (c), measured at a received power of ≈ −45 dBm.

This is shown in **Fig. 5.5a**, confronting the BER versus optical input power. As can be seen, error-free operation was achieved applying fiber lengths of 1000 and 2000 m, respectively. 4000 and 6000 m fiber length resulted in error floors with approximate BER levels of 10^{-8} and 10^{-7}, respectively. Related to 1000 m fiber-optic transmission, the power penalties for 2000, 4000 and 6000 m fiber length are 0.6, 1.0 and 1.3 dB at a BER level of 10^{-4}, respectively. This corresponds to electrical power penalties of 1.2, 2.0 and 2.6 dB. Eye diagram measurements after 1000 and 6000 m are shown in **Fig. 5.5b** and

Fig. 5.5c. Apparently, the eye opening is significantly reduced after 6000 m fiber-optic transmission due to chromatic dispersion effects.

A further measurement was carried out to evaluate the system linearity, i.e. received signal versus transmitted signal amplitude, which is shown in **Fig. 5.6**. This is of interest when applying higher-level amplitude modulation schemes like 5-ASK which is e.g. applied for the case of 1 GbE [82]. For the measurement, a data rate of 1.25 Gb/s was utilized, and the transmit amplitude was varied within 0.25 and 2 V_{pp}. As can be seen, the system exhibits a

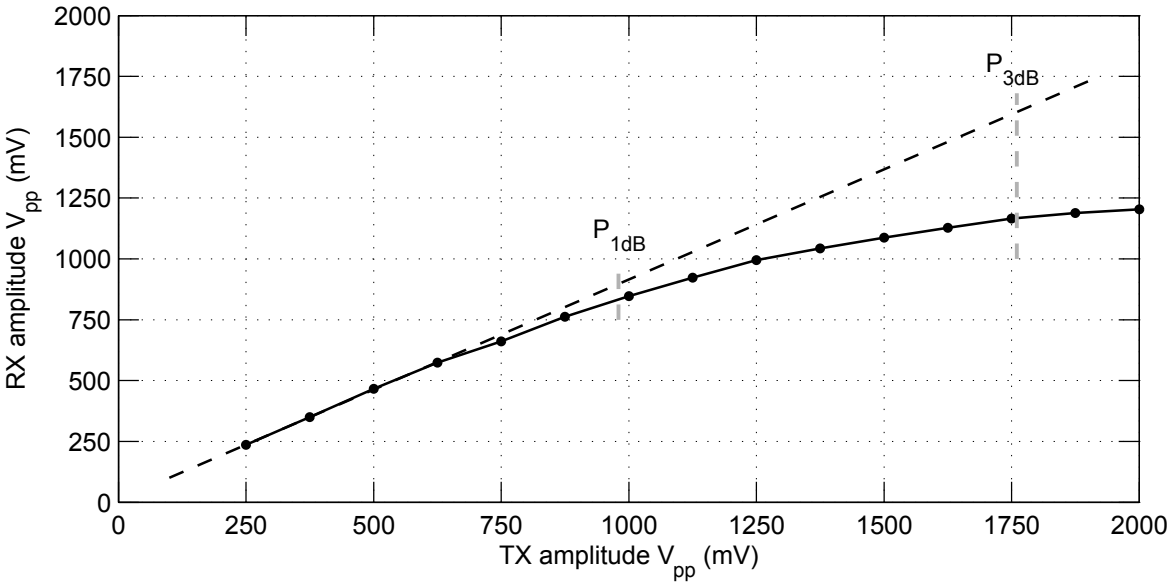

Figure 5.6: System linearity measurement showing the amplitude of the received signal versus transmit signal amplitude.

quasi-linear behavior for TX amplitudes of up to ≈ 1000 mV. The measured values for 1 and 3 dB power compression P_{1dB} and P_{3dB} are 980 and 1760 mV, respectively. As a conclusion, the signal power would have to be reduced accordingly with rising number of amplitude states.

5.2.2 Outdoor – 25 and 50 m wireless transmission length

Outdoor measurements have been performed at the university campus in front of the department. The system remained unaltered as shown in **Fig. 5.1**, also the operation conditions remained the same, and wireless RoF transmitter and wireless receiver were placed at a height of 120 cm above ground. The

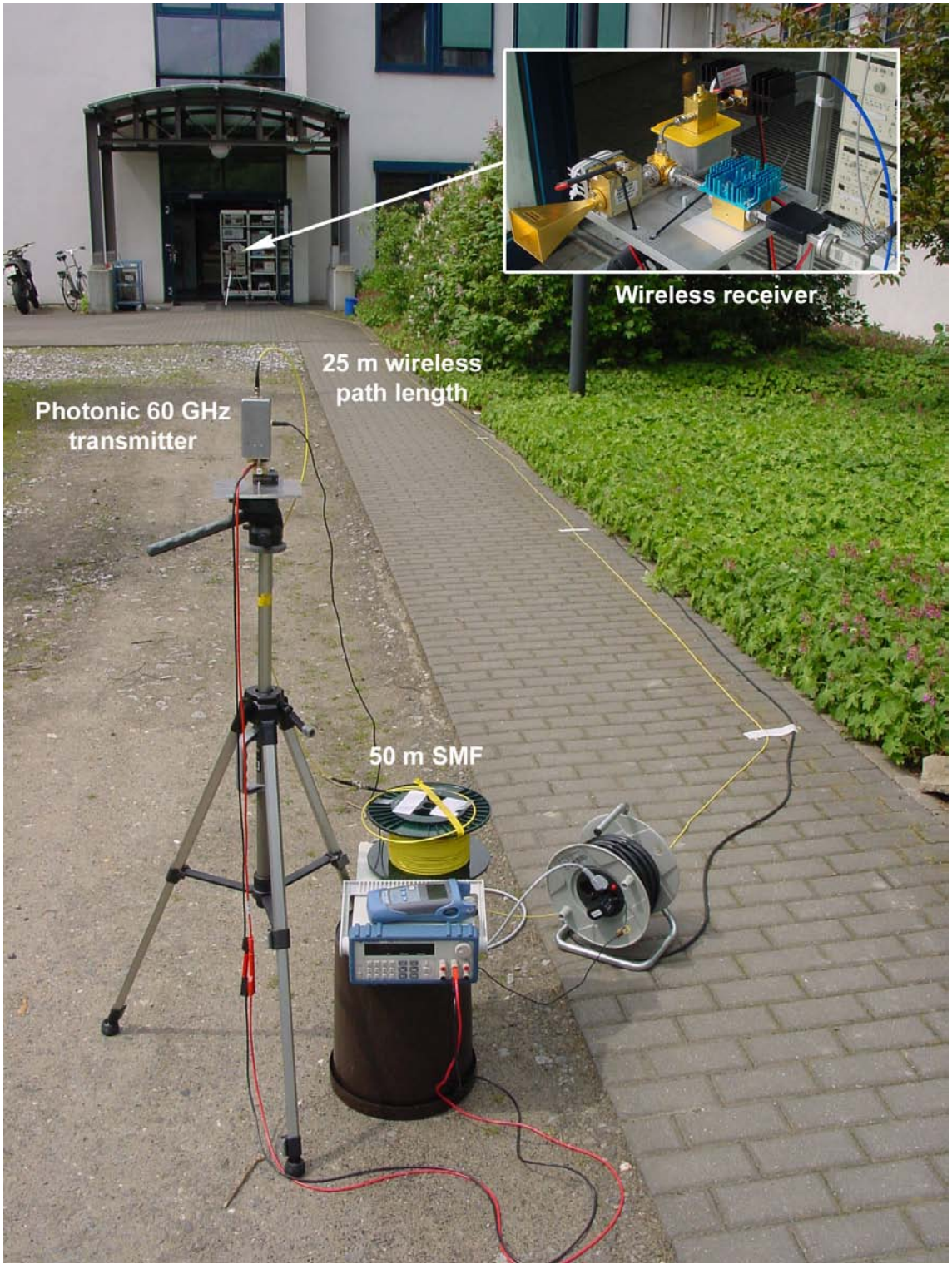

Figure 5.7: Photograph of the outdoor measurement with an applied wireless path length of 25 m. The wireless receiver is further shown in the inset.

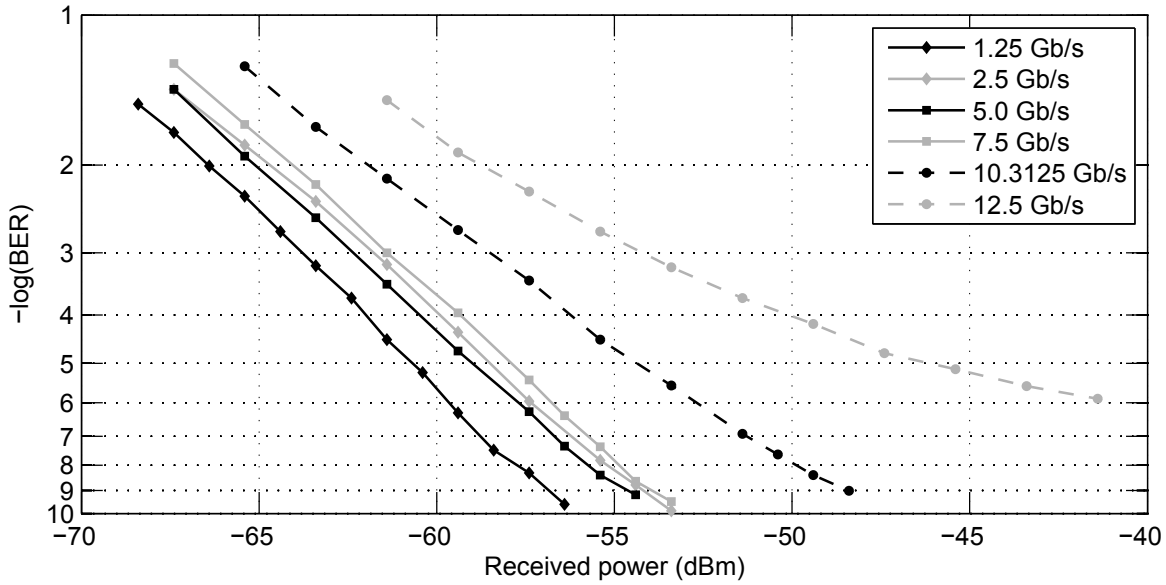

(a) 25 m of wireless transmission

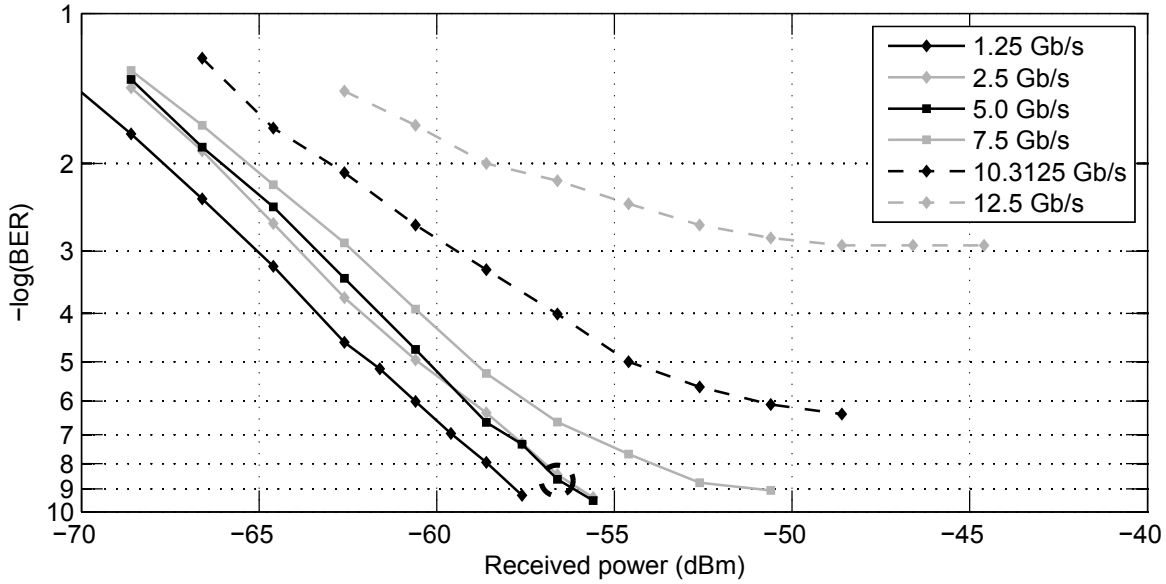

(b) 50 m of wireless transmission

Figure 5.8: Outdoor BER measurements for a fiber-optic transmission span of 50 m at various data rates. The indicated point in (b) will be further discussed in **Tab. 5.2**.

transmit power of the link was controlled by the OA. Different from the indoor experiments is an increased optical input power to the photodetector and thus an increased transmit power at the antenna to counter the larger path loss. Experiments have been carried out with data rates of up to 12.5 Gb/s for wireless path lengths of 25 and 50 m. The maximum wireless path

length was limited by surrounding buildings and obstacles. The measurement environment for 25 m wireless path length is shown in **Fig. 5.7**. Optical signal generation and the wireless receiver were positioned at the main entrance of the department, and the wireless RoF transmitter was separated to a path length of 25 m.

BER characterizations have been accomplished for 25 and 50 m for data rates of 1.25 Gb/s up to 12.5 Gb/s, which is shown in **Fig. 5.8**. The measured sensitivities to achieve a BER of 10^{-9} after 25 m for 1.25, 2.5, 5.0, 7.5 and 10.3125 Gb/s are −56.9, −54.2, −54.6, −53.8 and −48.4 dBm, respectively. The BER curve for 12.5 Gb/s shows an error floor of about 10^{-6}, the lowest BER measured here was $1.3 \cdot 10^{-6}$. For 50 m wireless path length, sensitivities of −57.1, −56.0, −56.1 and −50.9 dBm have been achieved with data rates of 1.25, 2.5, 5.0 and 7.5 Gb/s, respectively. The error-floor for 7.5 Gb/s is clearly observable. For 10.3125 and 12.5 Gb/s-operation, the best bit error rates are $4.3 \cdot 10^{-7}$ and $1.3 \cdot 10^{-3}$, respectively.

In comparison, BER characterization results for data rates of up to 5 Gb/s are in good agreement with 25 and 50 m of wireless transmission. However, the difference in sensitivity may be caused by slightly misaligned antennas or a fractionally different system operation point during characterization. For

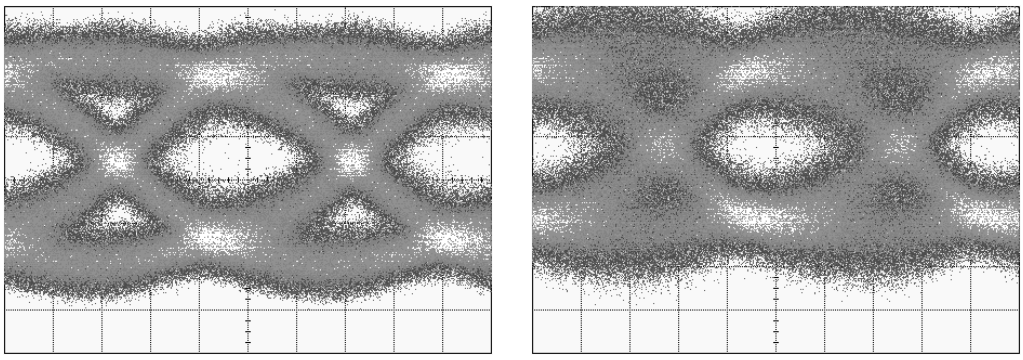

(a) 100 mV/div, 20.0 ps/div **(b)** 100 mV/div, 20.0 ps/div

Figure 5.9: 10.3125 Gb/s eye diagrams measured at a received power of ≈ −45 dBm, (a) after 25 m and (b) after 50 m of wireless transmission.

higher data rates of 7.5 Gb/s and above with 50 m of wireless transmission distance, the BER curves exhibit considerable variations. Possible reasons for this mismatch may be multipath propagation effects due to reflective surfaces

surrounding the measurement setup and an incipient power saturation of a component within the setup. A positioning test of the wireless transmitter has been carried out at a wireless path length of 50 m while repositioning the wireless transmitter in 25 cm transversal steps. While realigning the transmitter antenna in each step to the receiver antenna and maintaining the wireless path length, the quality of the received eye exhibited significant fluctuations. The reduced received signal quality for 50 m compared to 25 m of wireless transmission is further exemplified in **Fig. 5.9**, showing eye diagrams measured at a data rate of 10.3125 Gb/s. The eye opening for 50 m of wireless transmission is apparently reduced.

5.3 Link budget simulation

The link budget of the system is calculated by considering each significant electrical and optical component and implementing relevant noise contributions as discussed in **3** and **4**. Identical operation points are chosen both for the simulation and the experimental system. In detail, the optical power was controlled by an optical attenuator OA.

In the following, a link budget is simulated for 50 m of fiber-optic and 50 m of wireless transmission at a data rate of 5 Gb/s which is shown in **Tab. 5.10**. The corresponding experimental result is indicated in **Fig. 5.8b**. According to the system setup given in **Fig. 5.1**, the photonic mm-wave generator is modeled by ECL, EDFA-1 and MZM-1, delivering a carrier-suppressed photonic 60 GHz signal with an optical power of 7.50 dBm to the input of MZM-2. The applied operating point induces equivalent-electric losses of about −34 dB to the signal. After amplification with EDFA-2 and attenuation with the OA the signal is coupled to the photodetector, giving a further equivalent electric loss of −13.2 dB while o/e-converting the signal. The optical losses of 5 dB are induced by fibers, couplers and the insertion loss of the optical attenuator as well. After photodetection the SNR is reduced from initially 72 dB to now 28.45 dB due to shot-, RIN- and ASE-noise contributions. After amplification and wireless transmission the signal is received by AN-2. The described electrical losses are caused by a WR15-to-V transition and flanged waveguide lengths as well. After 50 m of wireless propagation the signal is attenuated close to noise floor and the noise contributions generated in

Table 5.2: Link budget table for 5 Gb/s photonic-wireless transmission.

ID	Comment	G_{el} (dB)	NF_{el} (dB)	P_{el} (dBm)	N_{el} (dBm)	SNR_{el} (dB)	G_{opt} (dB)	P_{opt} (dBm)
ECL		-	-	-	-	-	-	03.00
EDFA-1		-	-	-	-	-	14.00	17.00
MZM-1	$\eta_{EO,RF} = 0.011$	-	-	-	-	-	−9.50	7.50
PPG	5.0 Gb/s	-	-	10.00	−62.00	72.00	-	-
MZM-2	$\eta_{EO,RF} = 0.015$	−34.01	-	−24.01	−96.01	72.00	−5.80	1.70
EDFA-2		27.60	-	3.59	−68.41	72.00	13.80	15.50
(opt. losses)		−10.00	10.00	−6.41	−74.89	68.48	−5.00	10.50
OA		−18.00	18.00	−24.41	−76.95	52.53	−9.00	1.50
PD	$\eta_{OE,RF} = 0.29$	−13.20	-	−37.62	−90.15	52.53	-	-
$N_{el,shot}$	−74.4 dBm	-	4.48	−37.62	−74.30	36.69	-	-
$N_{el,rin}$	−67.9 dBm	-	9.58	−37.62	−67.02	29.40	-	-
$N_{el,sig-ase\,(1)}$	−76.0 dBm	-	3.52	−37.62	−66.50	28.89	-	-
$N_{el,sig-ase\,(2)}$	−76.2 dBm	-	3.41	−37.62	−66.06	28.45	-	-
PA-1		39.00	5.00	1.38	−26.36	27.75	-	-
(el. losses)		−2.50	2.50	−1.12	−28.86	27.75	-	-
AN-1	EIRP	23.00	-	21.88	−5.86	27.75	-	-
(50 m)	EIRP	−101.98	-	−80.10	−107.85	27.75	-	-
AN-2		23.00	0.02	−57.10	−76.33	19.23	-	-
LNA-1		18.00	3.50	−39.10	−55.18	16.08	-	-
MIX		−7.50	7.50	−46.60	−62.55	15.95	-	-
LNA-2		35.50	2.80	−11.10	−26.91	15.81	-	-
	simulated BER (using **(4.10)**)					$3.3 \cdot 10^{-10}$		
	measured BER (see **Fig. 5.8b**)					$2.5 \cdot 10^{-9}$		

AN-2 and LNA-1 severely reduce the SNR. After down-conversion using MIX and baseband amplification with LNA-2, the received signal exhibits now a simulated SNR of 15.81 dB which corresponds (according to **(4.10)**) to a BER of $3.3 \cdot 10^{-10}$, assuming white noise sources with Gaussian distribution. For the same operation point, the experimental BER exhibits a value of $2.5 \cdot 10^{-9}$. Further, experimental and simulated BER curves at a data rate of 5 Gb/s are shown in **Fig. 5.10**, comparing the cases of 2.5, 25 and 50 m of wireless transmission. As can be seen, both experimental result and simulation

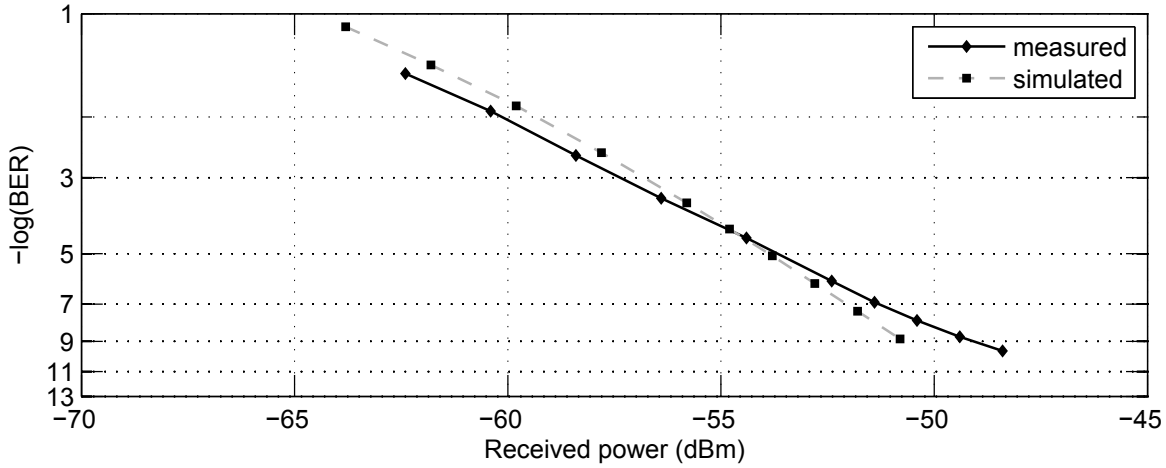

(a) 2.5 m of wireless transmission (see **Fig. 5.3b**)

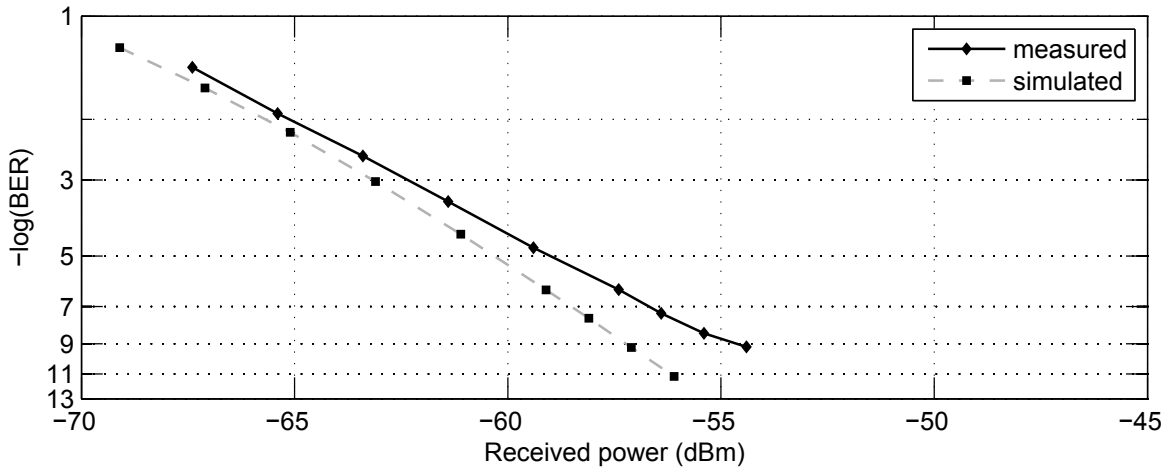

(b) 25 m of wireless transmission (see **Fig. 5.8a**)

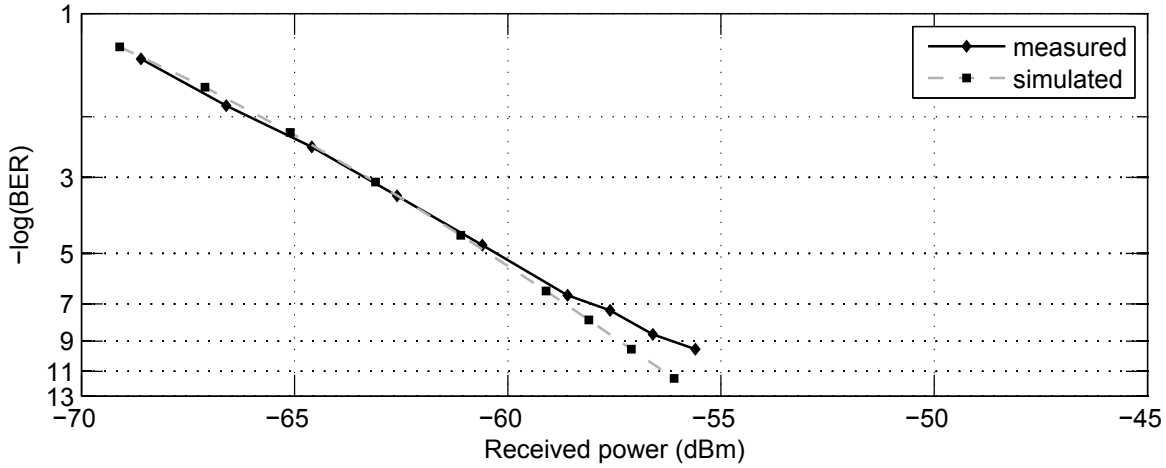

(c) 50 m of wireless transmission (see **Fig. 5.8b**)

Figure 5.10: Simulated vs. measured BER curves at 5 Gb/s.

for 2.5 m of wireless transmission show a sensitivity reduction of ≈ 7 dB compared to the characterization with 25 and 50 m of wireless transmission span. The reason here is the extremely low signal input power to PA-1 due to high levels of optical attenuation which is validated by the simulation results. The congruence between simulation and characterization is best at 50 m of wireless transmission span and decreases for wireless distances of 25 and 2.5 m. Further on, the simulated BER curves exhibit a better behavior and tend to lower error levels than the measured ones.

It is difficult to identify the exact cause for this mismatch. Potential reasons may be for instance a bandwidth insufficiency of a component at a specific frequency generating persistent errors, or real noise figures slightly different than the specified ones. Another potential reason is that the assumption of an additive white Gaussian noise (AWGN) channel used for calculating the BER from the SNR is not fully appropriate, as some noise sources exhibit other distributions. Finally, the simulation is scalar which does not comprise frequency responses of the applied components. This makes especially the simulation of the 10.3125 and 12.5 Gb/s-curve impractical. However, the developed theoretical model exhibits a sufficient agreement with the experimental results and allows a very good estimation of the system performance.

5.4 Range extension

With the experiments discussed above, wireless path lengths of up to 50 m have been achieved due to spatial limitations of the university campus on the one side and a limited power budget on the other side. Transmitter and receiver placement at a height of 120 cm over ground with surrounding buildings may lead to multipath propagation and thus to a distorted received signal. However, the typical application scenario of such a link would be to place transmitter and receiver on the roof of two opposing buildings to bridge longer distances.

In this section, a thought experiment is discussed in which the wireless path length could be increased by replacing the applied 23 dBi horn antennas with high-gain antennas (e.g. Cassegrain or Gaussian optical lens antennas), which are commercially available with gains of 50 dBi and more. Based upon the experimental results, i.e. applying the measured receiver sensitivities

which are shown in **Fig. 5.8**, the power received by the wireless receiver is calculated as a function of wireless path length. Besides 50 dBi instead of 23 dBi gain antennas, as well as a transmit power of 10 dBm, the setup is supposed to be unaltered. Considering the properties of the V-band as deduced in **3.6**, the spectral attenuation peaks at approximately 60 GHz but remains comparatively flat below 55 and above 65 GHz. Further considering

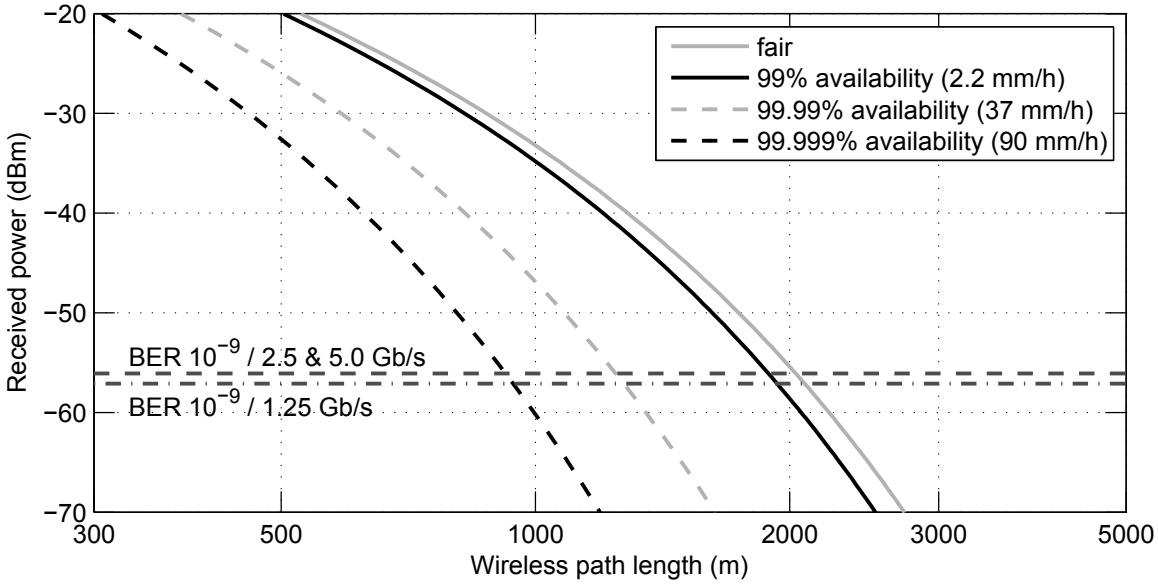

Figure 5.11: Wireless range estimation of the system for the case of 50 dBi instead of 23 dBi antennas being applied. The measured sensitivities for a BER of 10^{-9} for data rates of 1.25, 2.5 and 5.0 Gb/s deduced from **Fig. 5.8** are further indicated.

for example an NRZ-modulated 10.3125 Gb/s signal with a carrier frequency of 60 GHz, the spectral path loss after 1 km of wireless transmission would differ by a value of about 19 dB, which is inapplicable. However, for the case of a wireless 1 GbE (1.25 Gb/s) or an OC-48 signal (2.5 Gb/s) with approximate double-side bandwidth consumptions of 2.5 and 5.0 GHz, a wireless link extension to the km-range is feasible.

For the calculation of the wireless path loss at 60 GHz as described in **3.6**, peak gaseous attenuation L_{gas} of 16.2 dB/km and rain attenuations L_{rain} for availability levels of 99, 99.99 and 99.999 %, as well as for fair weather conditions (without rain attenuation) were considered. Within a continental-D1 climate region as discussed in **Tab. 3.1**, the corresponding rain amounts are 2.2 mm/h for 99 %, 37 mm/h for 99.99 % and 90 mm/h for 99.999 % availability, leading to attenuation figures of 1.6, 13.7 and 27.0 dB/km, respectively.

While further considering the measured receiver sensitivity for a given data rate as shown in **Fig. 5.8**, the corresponding maximum wireless path length can be derived. As can be seen from **Fig. 5.11**, maximum wireless path length to achieve a BER of 10^{-9} for 1.25 Gb/s-operation is ≈ 2040 m supposing fair weather conditions. While implementing rain attenuation, the achievable wire-

Table 5.3: Link budget table according to **Tab. 5.2** assuming 50 dBi antennas and a transmit power of 10 dBm.

ID	Comment	G_{el} (dB)	NF_{el} (dB)	P_{el} (dBm)	N_{el} (dBm)	SNR_{el} (dB)	G_{opt} (dB)	P_{opt} (dBm)
(unaltered photonic mm-wave generation / data modulation, see **Tab. 5.2**)								
...	...	...	...	...	...	...	...	...
OA		−6.88	6.88	−13.29	−76.47	63.17	−3.44	7.06
PD	$\eta_{OE,RF}$ = 0.29	−13.20	-	−26.50	−89.67	63.17	-	-
$N_{el,shot}$	−68.9 dBm	-	8.75	−26.50	−68.82	42.33	-	-
$N_{el,rin}$	−56.8 dBm	-	20.23	−26.50	−56.53	30.04	-	-
$N_{el,sig-ase\,(1)}$	−64.9 dBm	-	12.35	−26.50	−55.94	29.45	-	-
$N_{el,sig-ase\,(2)}$	−65.1 dBm	-	12.16	−26.50	−55.45	28.95	-	-
PA-1		39.00	5.00	12.50	−16.38	28.88	-	-
(el. losses)		−2.50	2.50	10.00	−18.88	28.88	-	-
AN-1	EIRP	50.00	-	60.00	31.12	28.88	-	-
(940 m)	EIRP	−127.47	-	−67.46	−96.35	28.88	-	-
(gas. att.)	EIRP	−15.23	-	−82.69	−111.58	28.88	-	-
(rain att.)	EIRP	−25.38	-	−108.07	−136.96	28.88	-	-
AN-2		50.00	$4.3\cdot10^{-5}$	−58.07	−76.57	18.50	-	-
LNA-1		18.00	3.50	−40.07	−55.30	15.22	-	-
MIX		−7.50	7.50	−47.57	−62.66	15.09	-	-
LNA-2		35.50	2.80	−12.07	−27.02	14.95	-	-
	simulated BER (using **(4.10)**)					$1.1\cdot10^{-8}$		

less path lengths for 99, 99.99 and 99.999 % link availability can be predicted to 1930, 1270 and 940 m, respectively. This scenario is simulated in the following using the link budget model and assuming carrier-class availability of 99.999 % with a predicted wireless path length of 940 m. Besides the antenna gain modification to 50 dBi and a transmit power of 10 dBm, atmospheric gaseous and rain attenuation have been implemented as well. The results are

shown in **Tab. 5.3**, indicating a received SNR of 14.95 dB corresponding to a BER of $1.1 \cdot 10^{-8}$. This is in good agreement to the expected BER of $1 \cdot 10^{-9}$ for 940 m wireless transmission where experimental sensitivities have been utilized.

5.5 Comparison with the state-of-the-art and conclusion

The developed system using external modulation and coherent detection is capable of transporting data signals of up to 12.5 Gb/s. This fully meets the required gross data rates for 10 GbE. However, BERs of below 10^{-12} are suggested in the corresponding standards [82]. To meet this requirement, error correction may be performed at the receiver side, which is further described in [82] and common for commercial 10 GbE fiber-optic transceivers. A current limitation in the setup is the bandwidth of the applied mm-wave TX and RX amplifiers reducing transmission quality for data rates of 7.5 Gb/s and above.

The achieved wireless path length was as high as 50 m, limited by surrounding buildings and the remaining power budget. Based upon the system description in **3** and the developed simulation environment in **4** simulations on the system have been performed and proven an adequate theoretical description. This allows for instance a system designer to evaluate the system performance and to identify critical components and subsystems depending from the RoF system operating point. It was further shown that the wireless path length could be extended to the km-range while applying antennas with higher gain. Here, predictions based upon the experimentally determined receiver sensitivity and on theoretical simulations using the model reported in **4** have shown a very good agreement. According to these predictions, the maximum wireless range for carrier class availability is 940 m for 1.25 Gb/s.

For achieving carrier-class availability at higher data rates, the spectral efficiency needs to be increased, allowing the transmission of a 10 GbE signal over distances within the km-range. Using a digital modulation scheme with higher spectral efficiency would also result in a regulation-conform operation regarding the allocated unlicensed bandwidth.

Experiments have revealed that the maximum fiber-optic transmission span at 10.3125 Gb/s is as high as 6000 m, which would already be sufficient for many applications. Longer transmission spans can be realized by compensative methods like e.g. EDC or the usage of DCF.

In conclusion, 12.5 Gb/s data transmission via fiber and via a 60 GHz wireless RF carrier has been demonstrated for the first time over technical relevant distances in [O13]. This data transmission rate of 12.5 Gb/s has been achieved by utilizing the concept of MZM cascading and applying DSB-CS modulation. In addition, the fiber-optic transmission span was significantly extended if compared to conventional DSB-systems as for instance reported in [101, 106]. Further, compared to systems utilizing SSB modulation (e.g. reported in [108]) or DSF (e.g. reported in [193]), the complexity of the system developed in this thesis is significantly reduced. As regards the state-of-the-art, it should be noted that systems with higher data rates have been reported in [128, 135, 136]. However, those RoF systems either operated at a lower RF carrier frequency and much shorter wireless distances (e.g. at 24 GHz with a wireless path length of only 6 m [128]) or did not achieve any wireless transmission at all (e.g. in [135, 136]).

6

Experimental RoF system based upon external modulation and incoherent detection

This chapter presents a RoF system based upon the system description in **3** and utilizing the system link budget model detailed in **4**. Major aim of this system is to demonstrate multi-Gb/s wireless and fiber-optic transmission for point-to-point connections with reduced system complexity. The applied subsystems are

- 55.4 GHz DSB-CS carrier generation based upon external modulation,
- broadband NRZ data modulation using an external modulator,
- conversion and wireless transmission using an RoF transmitter,
- a wireless receiver using incoherent detection.

The structure of the system will be discussed in **6.1**, pointing out the differences from a comparison with the previous system in **5**. The achieved experimental results will be discussed in **6.2**. A simulation on the system will

be presented in **6.3**, utilizing the developed theoretical model. This will be followed by a conclusion in **6.4**.

6.1 System setup

The experimental system is shown in **Fig. 6.1**, exhibiting identical subsystems for photonic millimeter-wave generation, data modulation and wireless transmission as described in **5.1**. The coherent wireless receiver is replaced by an incoherent one. This is beneficial in terms of system complexity, as the phase information is no longer required, thus a PLL can be avoided besides a broadband mixer and the mm-wave LO source. After reception with a 23 dBi horn antenna and amplification with a low-noise amplifier, the envelope of the NRZ-OOK-modulated RF signal is detected with an envelope detector. The recovered baseband signal is further amplified and applied to an error detector for BER analysis. Besides the modified architecture for the wireless receiver, the system remained the same. This applies as well for the operating conditions for the photonic millimeter-wave generator, the data modulator and the wireless RoF transmitter. However, the RF carrier frequency was shifted from 60 GHz to 55.4 GHz for the experiments due to limitations of the utilized envelope detector discussed in **3.7**.

6.2 Experimental results

This section describes the achieved experimental results from transmitting data rates of up to 5 Gb/s. This reduced data rate compared to the previous system is based upon the limited bandwidth of the applied envelope detector. The characterization starts with an indoor measurement, setting fiber-optic transmission span and wireless path length to 50 and 2.5 m, respectively. A further indoor measurement will be discussed, applying a wireless path length of 2.5 m, a data rate of 1.25 Gb/s and various fiber-optic transmission spans. The aim here was to experimentally evaluate the maximum fiber-optic transmission span supported by the system at a 1 GbE compatible data rate. This will be followed by outdoor measurements with a constant fiber length of 50 m and wireless path lengths of 25 and 50 m.

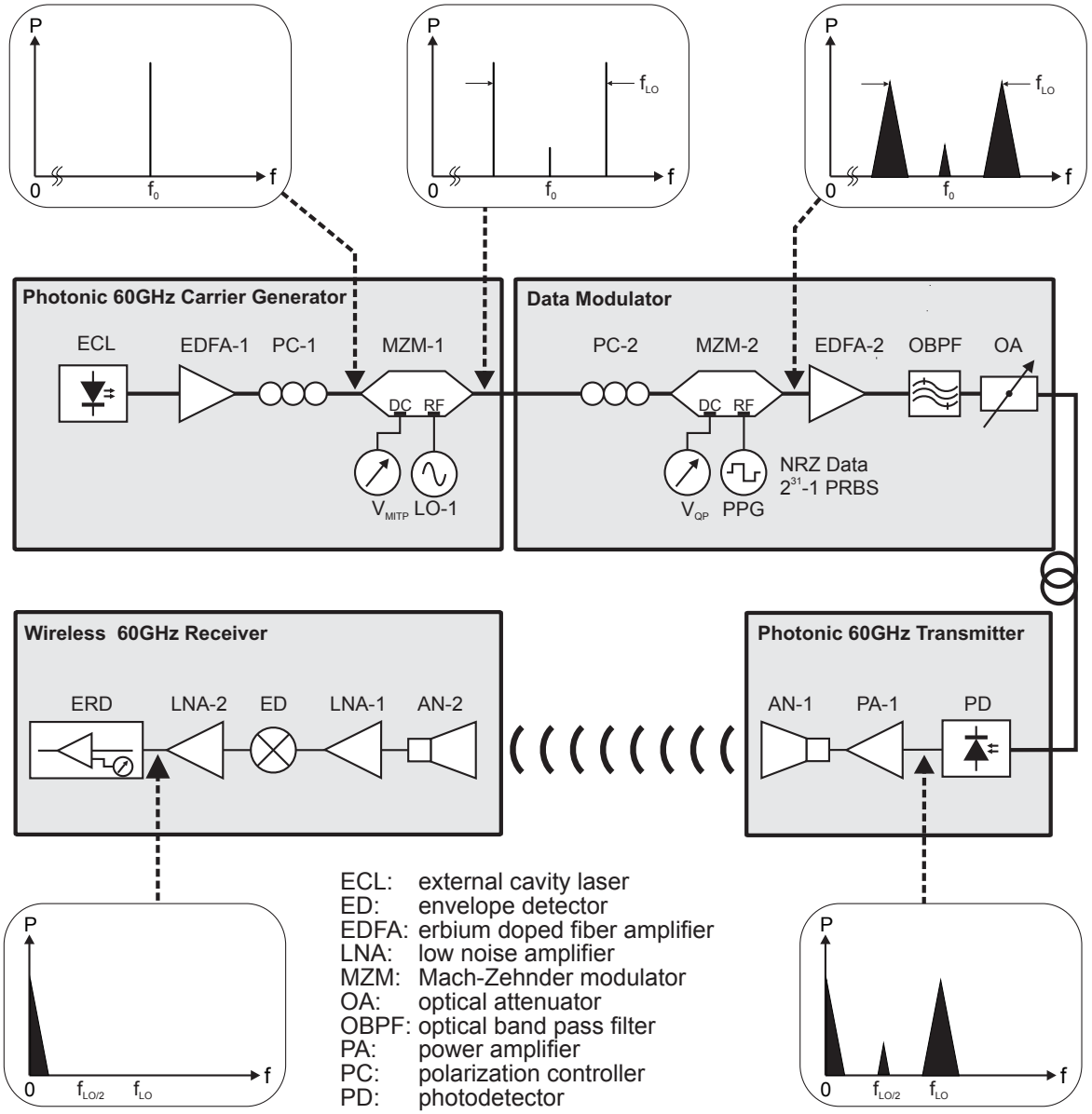

Figure 6.1: System setup showing the photonic 55.4 GHz carrier generator with subsequent broadband data modulation, the photonic transmitter and the wireless receiver using incoherent detection.

6.2.1 Indoor – 2.5 m wireless transmission length

Indoor characterizations within a laboratory environment have been accomplished where the wireless transmitter and receiver were placed at a height of 120 cm over ground and placed at a distance of 2.5 m. BER measurements have been carried out which are shown in **Fig. 6.2**. The measured sensitivities

for 1.25 and 2.5 Gb/s are −52.8 and −48.9 dBm, respectively. This corresponds to a power penalty of 3.9 dB for the 2.5 Gb/s curve. The BER curve for 5 Gb/s shows an error floor of about 10^{-7}.

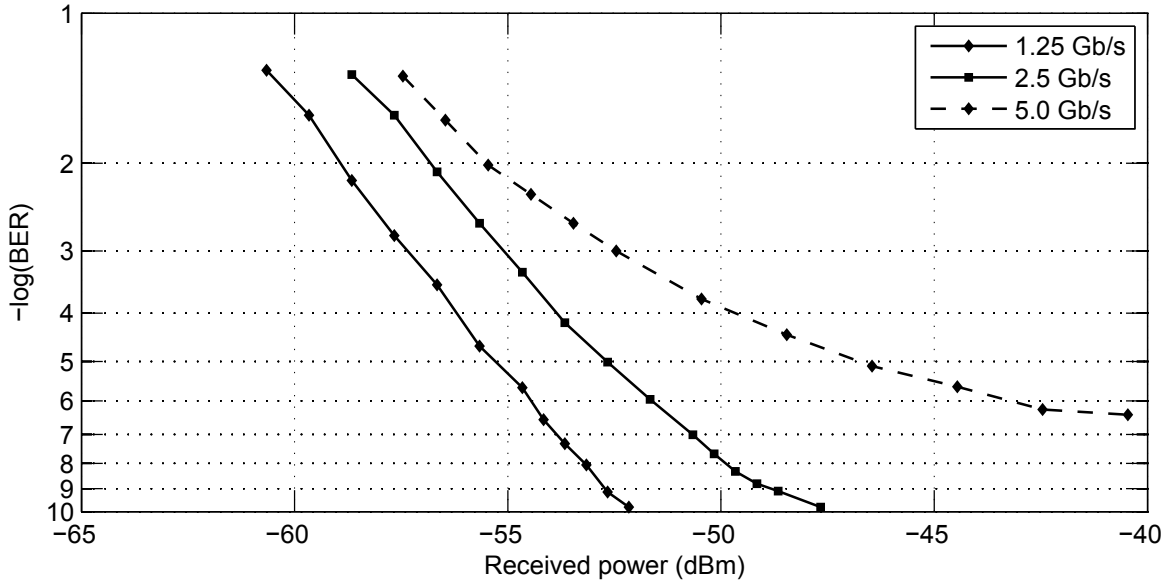

Figure 6.2: BER measurements applying 2.5 m of wireless and 50 m of fiber-optic transmission for various data rates.

Reasons for this reduced performance in terms of data rate are the applied envelope detector with its bandwidth of ≈ 2.6 GHz shown in **Fig. 3.26** and the utilized RF carrier frequency of 55.4 GHz. Here, the RF amplifiers PA-1 and LNA-1 were operated at their band edges which is shown in **Fig. 3.18** and **Fig. 3.25**, respectively. Besides these points the system remained unaltered compared to the previous setup in **5**.

A further measurement has been carried out to determine the maximum fiber-optic transmission length the system can accommodate. BER measurements have been accomplished at a 1 GbE compatible data rate of 1.25 Gb/s while altering the fiber length between data modulator and wireless RoF transmitter up to 40.9 km which is shown in **Fig. 6.3**, confronting the BER versus optical input power.

As can be seen, error-free operation is achieved applying fiber lengths of up to 25.4 km. Referring to 50 m of fiber-optic transmission length, the optical power penalties for 4.1, 10.7 and 25.4 km are 0.4, 0.6 and 1.9 dB, respectively. The curve for 40.9 km shows an error floor of about 10^{-8}.

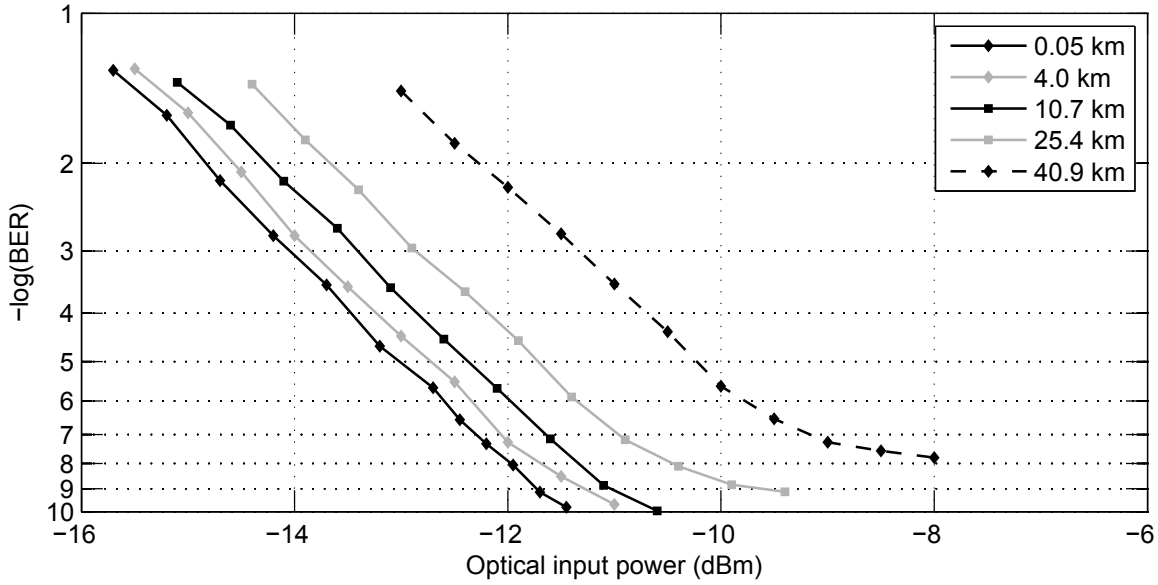

Figure 6.3: BER measurements at 2.5 m wireless path length and a data rate of 1.25 Gb/s for various fiber-optic transmission spans.

6.2.2 Outdoor – 25 and 50 m wireless transmission length

Outdoor measurements have been performed at the university campus in front of the department using an unaltered system. Also, the operation conditions remained the same and wireless RoF transmitter and wireless receiver were placed at a height of 120 cm above ground. As detailed above, the transmit power of the link was controlled by the OA, the difference compared to the indoor experiments is an increased optical input power and therefore increased transmit power at the antenna to counter the larger path loss.

Experiments have been carried out with data rates of up to 5 Gb/s for wireless path lengths of 25 and 50 m. Considering the results in **Fig. 6.4a** for 25 m of wireless transmission, the sensitivities for 1.25 Gb/s and 2.5 Gb/s are −54.5 and −49.5 dBm, respectively. An error-floor of below 10^{-9} can be deduced from the figure. The BER curve for 5 Gb/s-transmission shows an error-floor of $\approx 8 \cdot 10^{-5}$. For 50 m of wireless transmission given in **Fig. 6.4b** the sensitivity is −55.5 dBm for 1.25 Gb/s-operation while the BER-curve for 2.5 Gb/s-transmission exhibits an approximate error-floor of $3 \cdot 10^{-6}$. A measurement of 5 Gb/s was not possible as the received signal quality was too low. Comparing the BER curves at 1.25 Gb/s for 25 and 50 m of wireless transmission shows a good congruence. Eye diagrams have been measured

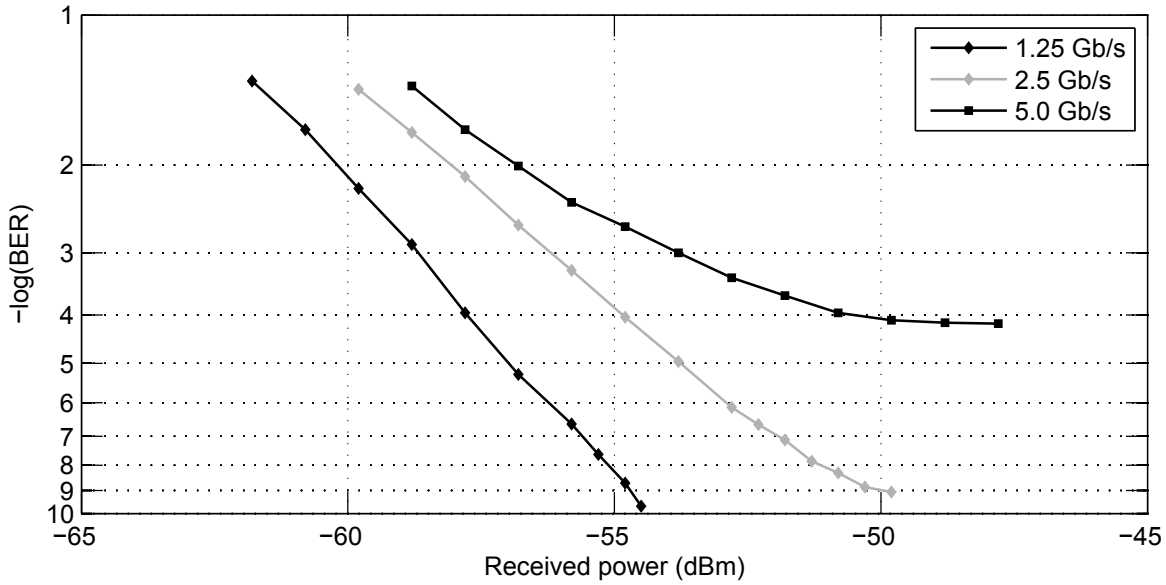

(a) 25 m of wireless transmission

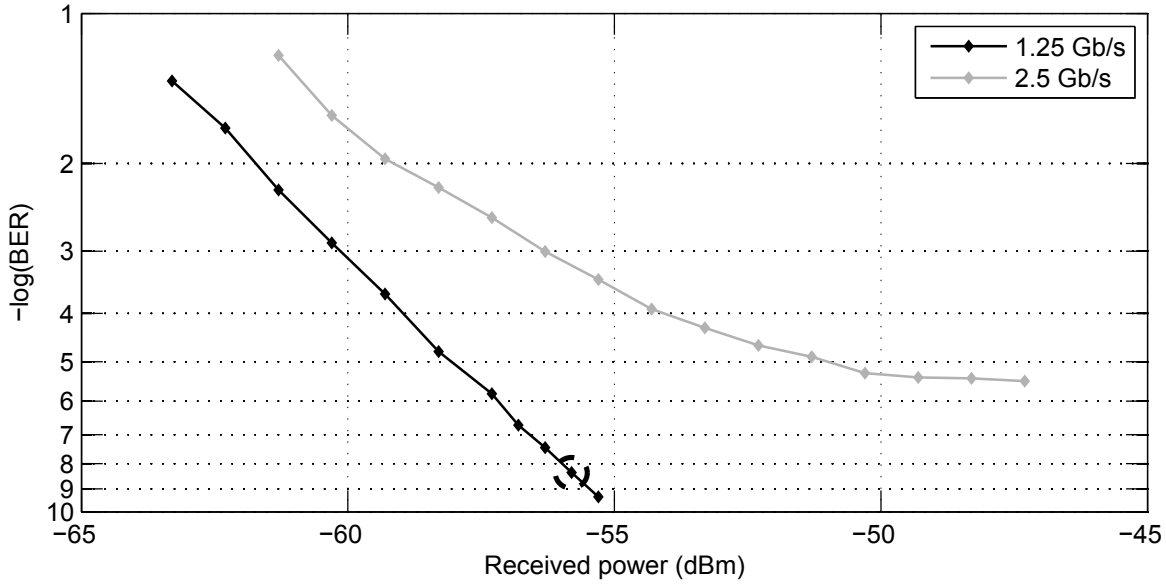

(b) 50 m of wireless transmission

Figure 6.4: Outdoor BER measurements at various data rates for a fiber-optic transmission length of 50 m. The indicated point in (b) will be further discussed in **Tab. 6.1**.

for a qualitative comparison which is shown in **Fig. 6.5**, exemplifying the eyes for 25 and 50 m of wireless transmission for 2.5 and 5.0 Gb/s-operation. For the case of 2.5 Gb/s shown in **Fig. 6.5a** and **Fig. 6.5b**, the eye for 50 m of wireless transmission is severely degraded and the eye opening is barely visible. For the case of 5.0 Gb/s-operation shown in **Fig. 6.5c** and **Fig. 6.5d**,

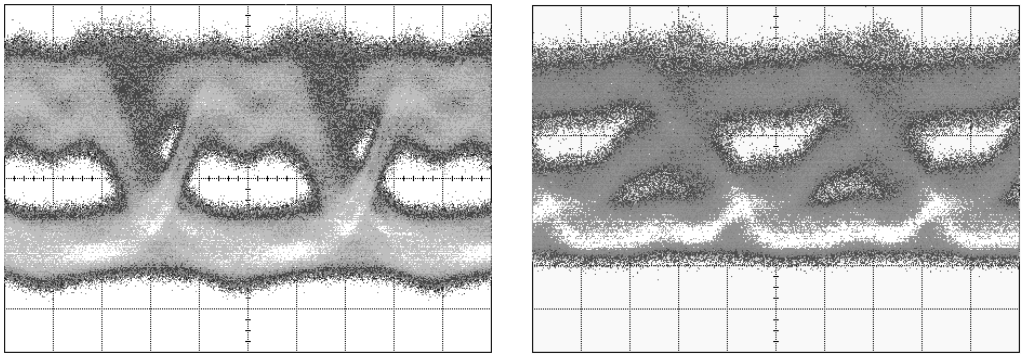

(a) 2.5 Gb/s, 25 m, 100 mV/div, 100 ps/div

(b) 2.5 Gb/s, 50 m, 100 mV/div, 100 ps/div

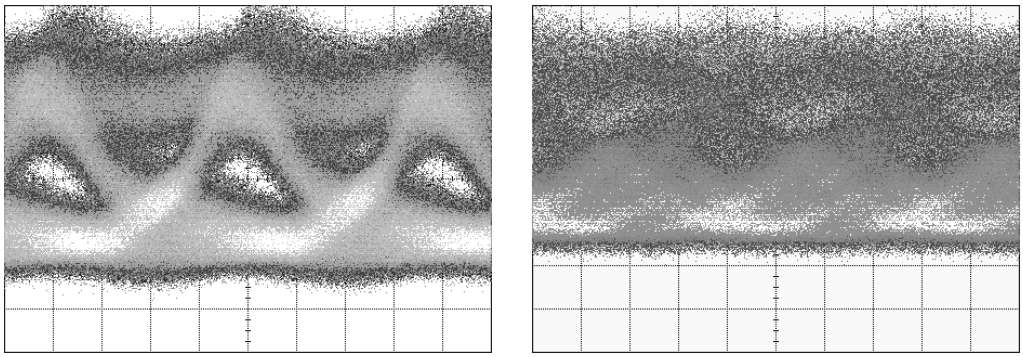

(c) 5.0 Gb/s, 25 m, 100 mV/div, 50 ps/div

(d) 5.0 Gb/s, 50 m, 100 mV/div, 50 ps/div

Figure 6.5: 2.5 and 5 Gb/s eye diagrams measured at a received power of ≈ -45 dBm applying 50 m fiber-optic transmission and a wireless span of 25 and 50 m, respectively.

the eye for 25 m wireless transmission is already defective while the 50 m eye is completely closed. This behavior is attributed to the performance of the envelope detector and the RF carrier frequency in conjunction with the bandwidths of PA-1 and LNA-1 as discussed in the previous section.

6.3 Link budget simulation

In analogy to **5.3** the link budget of the system is calculated by implementing the relevant noise contributions deduced in **3** and **4**. Like in the experimental characterization the optical power in the simulation was adjusted by the optical attenuator OA. A link budget has been simulated for 50 m fiber-optic

Table 6.1: Link budget table for 1.25 Gb/s photonic-wireless transmission.

ID	Comment	G_{el} (dB)	NF_{el} (dB)	P_{el} (dBm)	N_{el} (dBm)	SNR_{el} (dB)	G_{opt} (dB)	P_{opt} (dBm)
ECL		-	-	-	-	-	-	03.00
EDFA-1		-	-	-	-	-	14.00	17.00
MZM-1	$\eta_{EO,RF} = 0.011$	-	-	-	-	-	−9.50	7.50
PPG	1.25 Gb/s	-	-	10.00	−62.00	72.00	-	-
MZM-2	$\eta_{EO,RF} = 0.015$	−34.01	-	−24.01	−96.01	72.00	−5.80	1.70
EDFA-2		27.60	-	3.59	−68.41	72.00	13.80	15.50
(opt. losses)		−10.00	10.00	−6.41	−75.98	69.57	−5.00	10.50
OA		−17.50	17.50	−23.91	−79.12	55.21	−8.75	1.75
PD	$\eta_{OE,RF} = 0.29$	−13.20	-	−37.12	−92.32	55.21	-	-
$N_{el,shot}$	−76.4 dBm	-	4.64	−37.12	−76.27	39.16	-	-
$N_{el,rin}$	−69.6 dBm	-	10.02	−37.12	−68.78	31.67	-	-
$N_{el,sig-ase\,(1)}$	−77.7 dBm	-	3.81	−37.12	−68.26	31.15	-	-
$N_{el,sig-ase\,(2)}$	−77.9 dBm	-	3.69	−37.12	−67.82	30.71	-	-
PA-1		39.00	5.00	1.88	−28.18	30.07	-	-
(el. losses)		−2.50	2.50	−0.62	−30.68	30.07	-	-
AN-1	EIRP	23.00	-	22.38	−7.68	30.07	-	-
(50 m)	EIRP	−101.98	-	−79.60	−109.67	30.07	-	-
AN-2		23.00	0.02	−56.60	−78.49	21.89	-	-
LNA-1		18.00	3.50	−38.60	−57.37	18.77	-	-
ED		−16.05	16.05	−54.65	−72.42	17.78	-	-
LNA-2		35.50	2.80	−19.15	−36.17	17.02	-	-
	simulated BER (using **(4.11)**)					$5.8 \cdot 10^{-12}$		
	measured BER (see **Fig. 6.4b**)					$4.6 \cdot 10^{-9}$		

and 50 m wireless transmission at a data rate of 1.25 Gb/s. The simulated link budget table corresponds to the indicated measurement point in **Fig. 6.4b**.

According to the system setup shown in **Fig. 6.1** the photonic mm-wave generator is modeled by ECL, EDFA-1 and MZM-1, supporting an optical 60 GHz signal with suppressed carrier and with an optical power of 7.50 dBm to the input of MZM-2. After data modulation with MZM-2, amplification with EDFA-2 and attenuation with the OA the signal is coupled to the photode-

tector for performing o/e-conversion. Considering shot-, RIN- and ASE-noise contributions and the noise figure of PA-1 as well, the signal exhibits a SNR of 30.07 dB before wireless transmission. The electrical losses of 2.5 dB are induced by a WR15-to-V transition and by flanged waveguide lengths as well. The wireless path of 50 m causes losses of about 102 dB and attenuates the signal close to noise floor. After reception with AN-2 and amplification with LNA-1 the signal is applied to the envelope detector ED. The responsivity of $\approx$ 3000 mV/mW of the ED in conjunction with the input impedance of LNA-2 of 50 Ohm causes a loss of ≈ -16 dB. Finally, the received signal exhibits now a simulated SNR of 17.02 dB which corresponds (according to **(4.11)**) to a BER of $5.8 \cdot 10^{-12}$ assuming white noise sources with Gaussian distribution. In the experimental characterization the BER exhibits a value of $4.6 \cdot 10^{-9}$ at the same operation point.

Experimental and simulated BER curves are shown in **Fig. 6.6**, comparing the cases of 2.5, 25 and 50 m of wireless transmission for a data rate of 1.25 Gb/s. The course of the theoretical BER-curve for 2.5 m of wireless transmission agrees well with the experimental results but exhibits a slightly decreased BER performance. The simulated BER curves for 25 and 50 m of wireless transmission exhibit a larger gradient than the experimental ones. In addition, for the case of 25 m of wireless transmission, simulation and measurement exhibit a power mismatch of about 2 dB. Like in the previous chapter, both measured and simulated sensitivity for 2.5 m of wireless transmission is considerably reduced, if compared to 25 and 50 m. This is attributed to the low input power to PA-1 with its noise figure of 5 dB, as the reduced path loss for 2.5 m of wireless transmission is equalized with an increased level of optical attenuation, thus a reduced electrical input power to PA-1. No single reason can be given to explain this mismatch, but an explanation would be slightly improperly modeled components, like e.g. the responsivity of the ED or the noise figures of the amplifiers. Another possibility would be that the AWGN assumption used for calculating the BER from the SNR is not fully appropriate due to some non-Gaussian distributed noise sources. In addition, the simulation is purely scalar, which does not comprise the components' frequency responses.

However, despite the above discussed issues, the developed theoretical model shows a sufficiently good congruence with the experimental characterization.

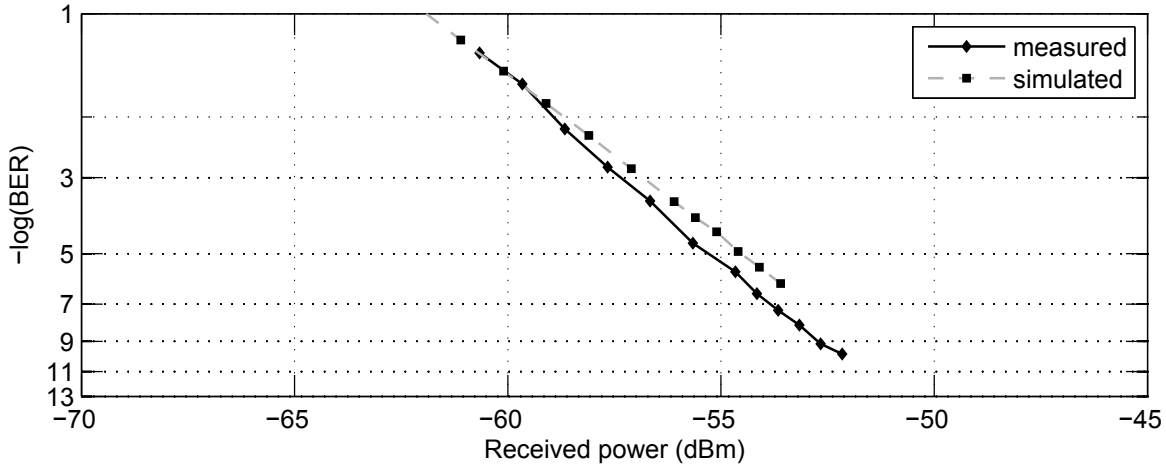

(a) 2.5 m of wireless transmission (see **Fig. 6.2**)

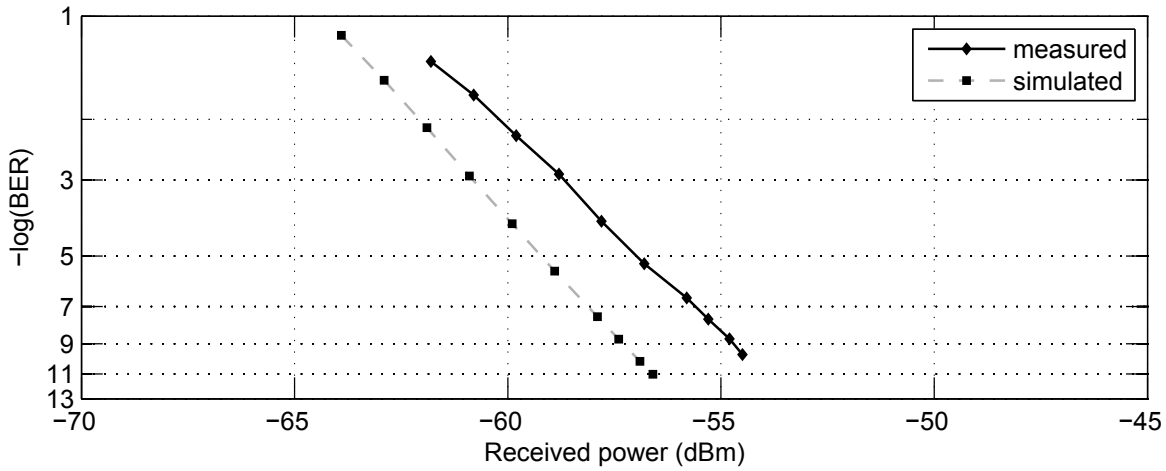

(b) 25 m of wireless transmission (see **Fig. 6.4a**)

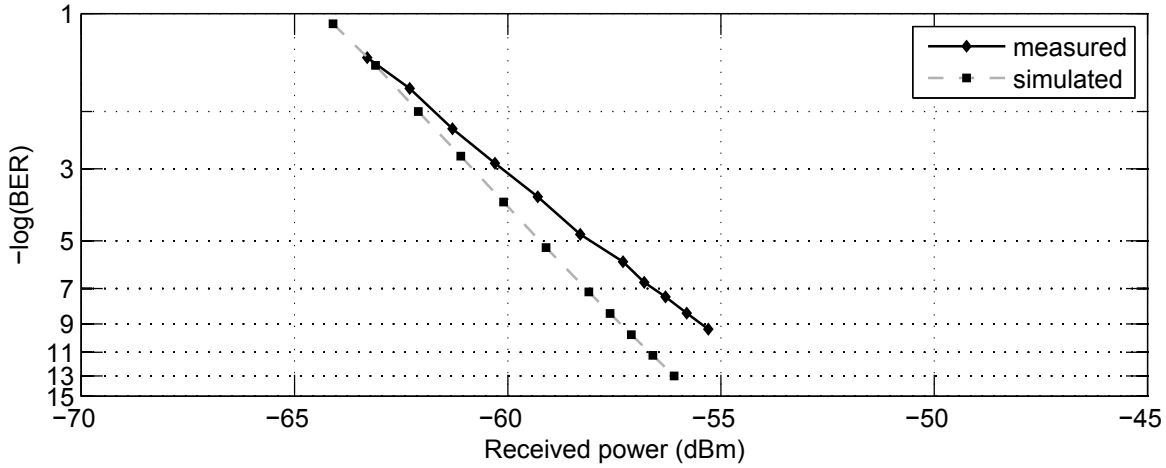

(c) 50 m of wireless transmission (see **Fig. 6.4b**)

Figure 6.6: Simulated vs. measured BER curves at 1.25 Gb/s.

6.4 Comparison with the state-of-the-art and conclusion

This system is capable of transporting data signals of up to 5 Gb/s for the case of 25 m of wireless transmission. Error-free operation has been demonstrated for 1.25 and 2.5 Gb/s-transmission. Further on, data transmission of up to 2.5 Gb/s has been achieved over 50 m of wireless span. For 1.25 Gb/s transmission rate, error-free operation has been demonstrated. Here, a good agreement between simulation and measurement and thus an adequate theoretical system description has been demonstrated. Furthermore, this allows to identify components and subsystems with need for optimization and to evaluate the system performance in advance.

Comparing this system with the previously discussed system in **5** shows that the complexity is considerably reduced by applying incoherent detection while fully supporting the required gross data rates for 1 GbE and OC-48 transmission.

Main limitations in this system with respect to achievable data rate are the applied envelope detector with a video bandwidth of approximately 2.6 GHz and the utilized carrier frequency of 55.4 GHz, as the RF amplifiers PA-1 and LNA-1 were operated at their band edges. An extension to transmit a 10 GbE-compatible data rate could be achieved by replacing the applied envelope detector by a detector with sufficient video bandwidth and operating at around 60 GHz. Such detectors are commercially available and have been applied for instance in the RoF system reported in [130]. The wireless range is as well extendable when using antennas with higher gain.

Experiments have further revealed that the fiber-optic transmission span at 1.25 Gb/s is at least 40 km, which would support extended range 1 GbE [82]. Using electronic dispersion compensation or dispersion compensating fiber would further increase the fiber-optic transmission span.

In conclusion, 5 Gb/s data transmission has been demonstrated via fiber and wirelessly over 50 m applying incoherent detection allowing a more complex system compared to coherent detection. As regards the state-of-the-art, only two RoF systems have been published where technical relevant wireless transmission spans have been realized with incoherent detectors [127, 130]. The achieved wireless transmission spans of 300 and 800 m have been achieved by utilizing high-gain antennas. However, it was already shown

in **5.4** that a wireless range extension to the km-range is feasible by replacing the applied medium-gain antennas with high-gain antennas if considering the achieved experimental sensitivities in this chapter. Other results utilizing incoherent detection are for instance reported in [42, 124, 134]. However, those systems only achieved wireless transmission over 3 m [124], 1.5 m [134] or did not comprise any wireless transmission at all [42].

7

Experimental RoF system based upon an MLLD and incoherent detection

The RoF system described in this chapter aims for a system with a minimum of complexity for applications with low-cost requirements. In detail, the system is foreseen to demonstrate uncompressed HDTV transmission. The applied subsystems are

- 58.8 GHz photonic mm-wave generation based upon a passive MLLD,
- broadband NRZ data modulation using an external modulator,
- conversion and wireless transmission using an RoF transmitter,
- an incoherent wireless receiver architecture.

Compared to the approach discussed in **5**, the coherent wireless receiver is replaced by an incoherent one, allowing photonic-wireless transmission with considerable reduced system complexity. When further compared to **6**, the photonic mm-wave generation is simplified by applying a mode-locked laser diode in the system. In sum, a very compact system with low complexity

has been realized. The structure of the system and the experimental characterization are presented in **7.1**. This system was exhibited at a booth [194], demonstrating uncompressed HDTV transmission, which is described in **7.2**. A conclusion on the system is given in **7.3**.

7.1 System setup and characterization

The system setup is shown in **Fig. 7.1**. For photonic mm-wave generation the MLLD is employed as described in **3.1**. The optical mm-wave comb is further modulated with NRZ-data of up to 5 Gb/s using a standard 10 Gb/s electro-absorption modulator. To compensate the insertion loss of the EAM, but also for the following BER analysis the data-modulated photonic mm-wave signal is coupled to an optical amplifier (EDFA-2) which is followed by an optical attenuator (OA) to control the optical input power to the photodetector and thus the o/e-converted RF power. After signal conversion, the signal is coupled to PA-1 and transmitted using AN-1. The wireless receiver is identical to the receiver discussed in **6**, consisting of a horn antenna AN-2, a low noise amplifier LNA-1 to amplify the signal before envelope detection and a Schottky detector ED to reconstruct the baseband data signal. For BER analysis, the signal is amplified by LNA-2.

Outdoor measurements have been performed at a wireless path length of 25 m and a fiber-optic transmission span of 50 m. BER characterizations for 1.25, 1.5, 3.0 and 5.0 Gb/s have been accomplished, as shown in **Fig. 7.2a**. The data rates of 1.5 and 3 Gb/s correspond to the necessary data rates to transmit an uncompressed HDTV signal, i.e. 1.485 Gb/s for 1080i and 2.97 Gb/s for 1080p.

The achieved experimental results give sensitivities of −46.4, −45.8 and −44.9 dBm for 1.25, 1.5 and 3 Gb/s-operation, respectively. For the case of 5 Gb/s, the BER curve shows an error-floor of $\approx 5 \cdot 10^{-7}$. Eye diagrams have been measured for a qualitative evaluation of the transmission quality shown in **Fig. 7.2b** to **Fig. 7.2e**. With rising data rate the eyes become more and more distorted and the eye opening of the 5 Gb/s-eye is barely visible, which is attributed to the limited video bandwidth of the applied envelope detector ED.

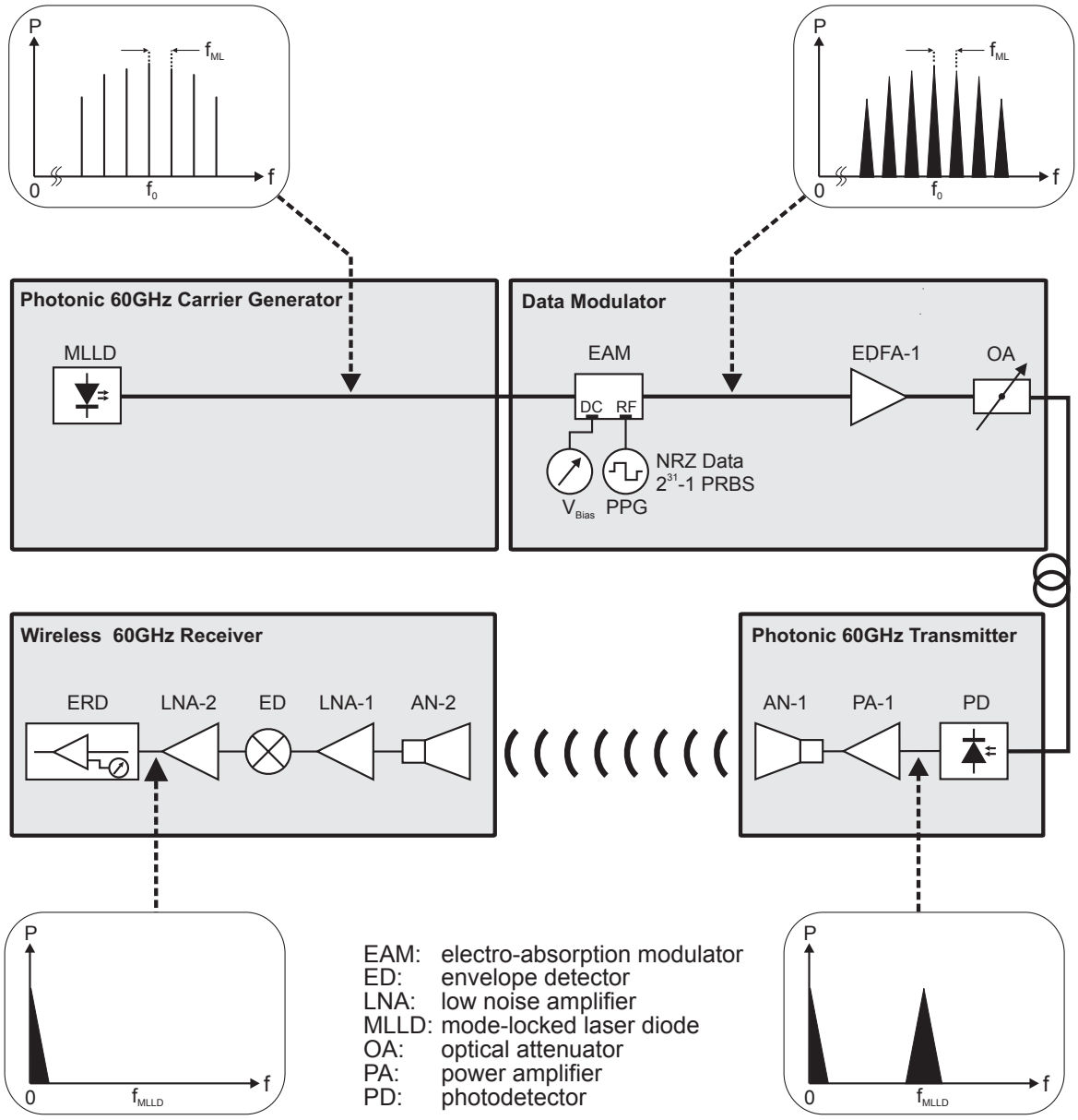

Figure 7.1: System setup showing the MLLD-based photonic 58.8 GHz carrier generator with subsequent broadband data modulation, the photonic transmitter and the wireless receiver using incoherent detection.

7.2 Realized demo system

Besides the development of advanced photonic components a further aim in IPHOBAC was a system demonstration based upon components developed within the project. In that regard, a demo was prepared and exhibited at ICT2008 in Lyon [194]. The aim of the demo was to demonstrate uncom-

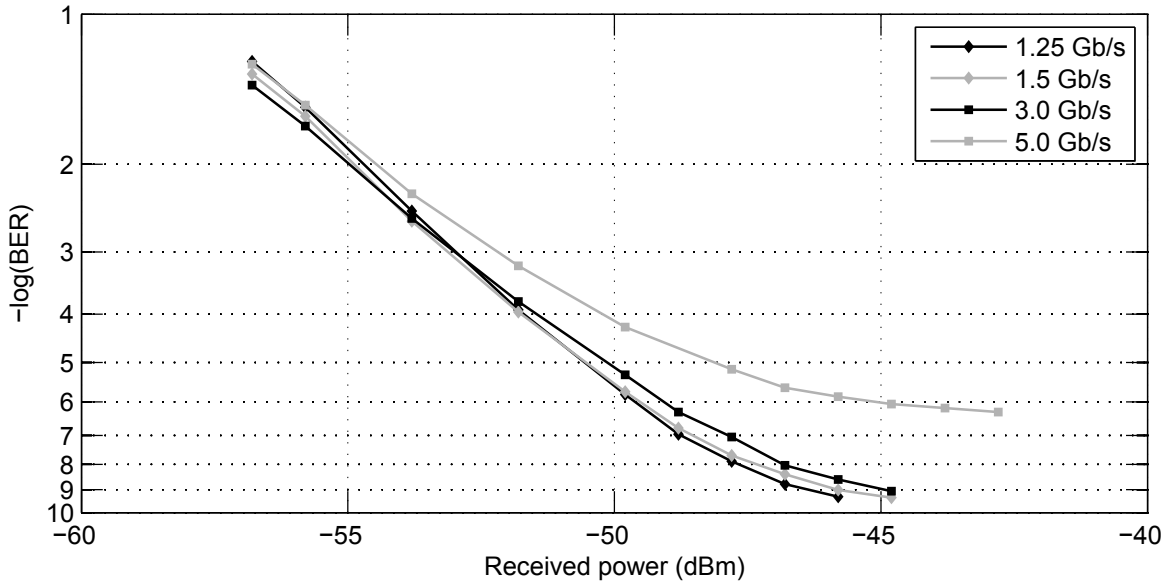

(a)

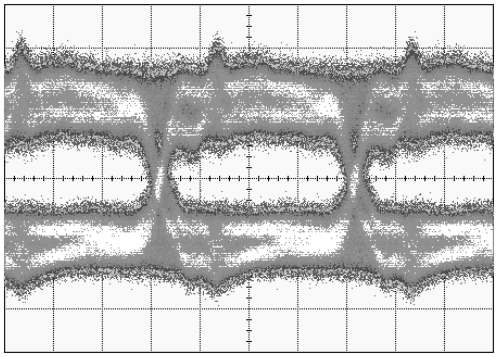

(b) 1.25 Gb/s, 100 mV/div, 200 ps/div

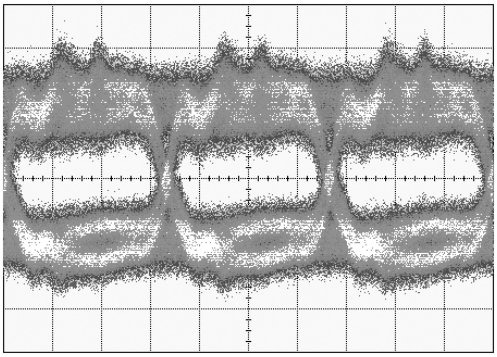

(c) 1.5 Gb/s, 100 mV/div, 200 ps/div

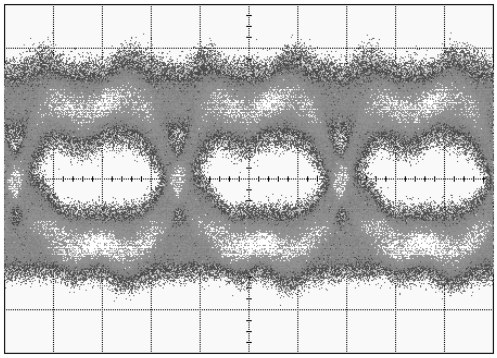

(d) 3.0 Gb/s, 100 mV/div, 100 ps/div

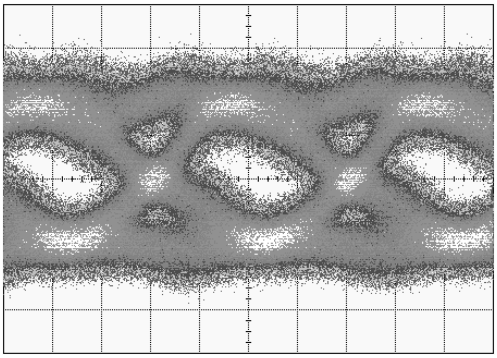

(e) 5.0 Gb/s, 100 mV/div, 50 ps/div

Figure 7.2: Outdoor measurement after 50 m of fiber-optic and 25 m of wireless transmission. (a) shows the BER characterization whereas eye diagram measurements are given in (b) to (e). The received power was set here to ≈ −45 dBm.

pressed HDTV transmission which is shown schematically in **Fig. 7.3**, based upon the system setup and the experimental results described before.

As an HDMI source, either a laptop with HDMI output or an HDTV camera with HDMI output port was applied. Using a commercial HDMI to HD-SDI converter, the data stream was converted to an NRZ signal and fed to the RF input of the EAM. Although the experiments above have shown that the transmission of a 1080p signal with a data rate of 2.97 Gb/s would be feasible, the utilized converters were only capable of transforming a 1080i signal, requiring a data rate of 1.485 Gb/s. After 50 m of fiber-optic transmission, the signal was received by the wireless receiver, back-converted from HD-SDI to HDMI and applied to an HDTV screen. The system setup was identical to

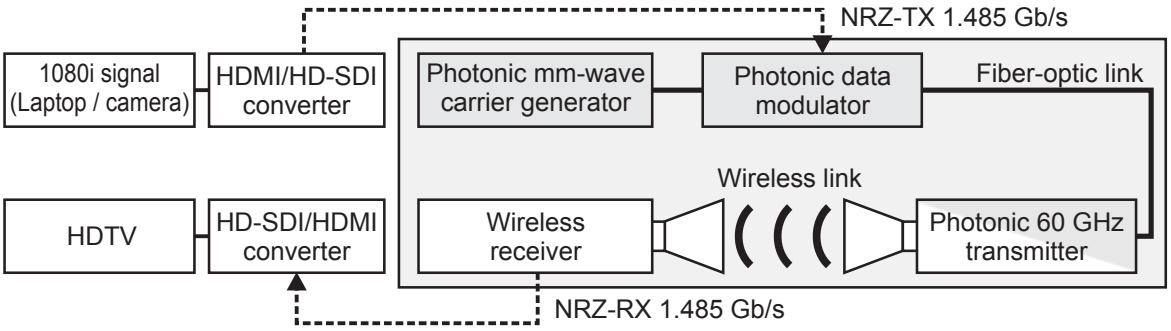

Figure 7.3: Schematics of the realized demo setup for uncompressed 1080i HDTV transmission.

the experimental setup shown in **Fig. 7.1** with the exception that the optical amplifier EDFA-2 and the optical attenuator OA have been removed from the system. This was done because the wireless path length in the demo was limited to about 3 m due to environmental limitations at the booth.

Three demonstration modules have been constructed. Photonic mm-wave generator and photonic data modulator have been packaged to one box with connectors for modulation input, optical output, DC supply, as well as temperature control for the MLLD as shown in **Fig. 7.4a** and **Fig. 7.4b**. The wireless RoF transmitter and receiver with horn antennas and connectors for DC supply, fiber input and data output are shown in **Fig. 7.4c** and **Fig. 7.4d**, respectively. **Fig. 7.4e** shows the completed demo setup with MLLD and data modulation unit, as well as the wireless transmitter. Here, a laptop is delivering a 1080i video signal to the RoF system which is connected to an HDTV screen after fiber-optic and wireless transmission. This system was

(a) MLLD and modulation unit

(b) MLLD and modulation unit

(c) wireless RoF transmitter

(d) wireless receiver

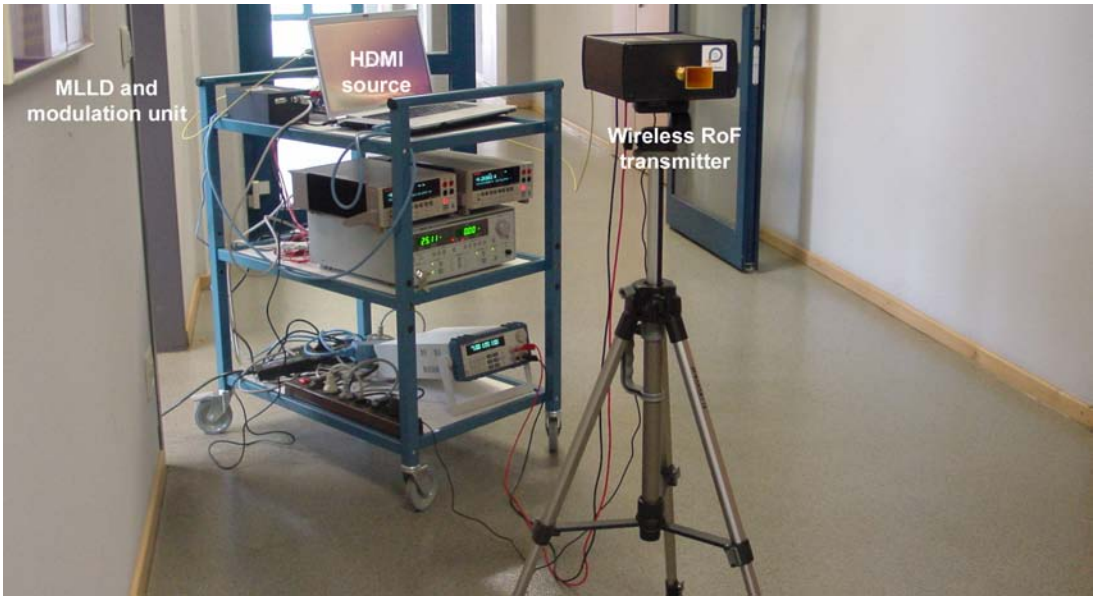

(e) demo system with a laptop delivering a 1080i signal to the transmitter

Figure 7.4: Photographs of the demo system for uncompressed HDTV transmission.

further presented at the ICT2008 in Lyon, France, and voted to one of the top 10 demonstrations among more than 200 exhibits [194].

7.3 Comparison with the state-of-the-art and conclusion

An RoF system for broadband photonic-wireless transmission of up to 5 Gb/s was presented, operating at an RF carrier frequency of 58.8 GHz. An extremely compact setup with low complexity was achieved with the applied MLLD in conjunction with the chosen incoherent receiver architecture and the simple modulation scheme. Error-free transmission of 1.5 and 3 Gb/s has been demonstrated, fully supporting the required data rates for uncompressed 1080i and 1080p HDTV. In addition, the setup was packaged to modules and exhibited at the ICT2008 in Lyon, hereby demonstrating the live transmission of an uncompressed HDTV signal.

Although applying a modulation scheme with low spectral efficiency, the consumed bandwidth of approximately 6 GHz for uncompressed 1080p transmission is lower than the specified unlicensed bandwidth around 60 GHz in most countries and regions shown in **Fig. 2.5**. The mode-locking frequency of 58.8 GHz is determined by the length of the active section and could be easily adjusted to e.g. 60 GHz, allowing regulation compliant operation with respect to the consumed bandwidth.

The achieved fiber-optic transmission length of 50 m and wireless path length of 25 m are already sufficient for indoor applications. Larger wireless path lengths could simply be achieved by applying antennas with higher gain, whereas an increased fiber-optic transmission span can be realized by applying an optical band-pass filter in the system. Hereby, the number of optical modes which participate during beating would be reduced, thus resulting in reduced chromatic dispersion power penalties. The limitation in terms of data rate is induced by the applied envelope detector. Applying a detector with sufficiently high video bandwidth could potentially allow 10 Gb/s-transmission as the other components exhibit an adequate bandwidth.

In conclusion, 5 Gb/s data transmission has been demonstrated via 50 m of fiber-optic and 25 m of wireless transmission. The applied MLLD in conjunction with incoherent detection allowed an RoF system with extremely

low complexity. The system was packaged to compact modules and further exhibited at the ICT2008 in Lyon, demonstrating uncompressed 1080i HDTV transmission and achieved a ranking under the top ten exhibitions among 200 competitors [194].

Further on, we reported a RoF system with a direct modulated 60 GHz MLLD for the first time [O20]. Here, a structurally-identical MLLD with a mode-locking frequency in the 60 GHz band was applied, thus omitting the external modulator. Error-free 3 Gb/s data transmission over 50 m of fiber and 5 m of air has been demonstrated using OFDM with QPSK subcarrier modulation.

As regards the state-of-the-art, there has been published one similar achievement by NTT, who demonstrate an RoF system also utilizing an MLLD at a carrier frequency and data rate of 240 GHz and 3 Gb/s, respectively [126]. However, in this experiment the MLLD was not operated in passive mode but was actively mode-locked at a subharmonic requiring additional RF sources as compared to this work.

8

Summary and recommendations

8.1 Summary

This thesis has investigated RoF-systems for future broadband communication, merging fiber-optic and wireless technologies together. Instead of distributing the data signals within the baseband and performing electrical up-conversion and wireless transmission, the up-conversion is achieved solely by means of photonic techniques. Furthermore, to allow data transmission rates within the multi-Gb/s range, the carrier frequency was extended to the millimeter-wave range around 60 GHz, while conventional radio systems operate at microwave frequencies.

In **2**, the key concept of RoF has been evaluated, various methods and techniques for optical up-conversion have been compared and analyzed. To achieve super-broadband data transmission rates, the unlicensed frequency range around 60 GHz was utilized, where several GHz of bandwidth are available which had required an evaluation of regulation issues. Previously achieved results within the field of RoF communication systems have been thoroughly studied and analyzed.

For developing a model to theoretically describe and analyze the realized RoF systems, each system was divided into generic subsystems. The applied subsystems have been described, experimentally characterized and modeled in **3**, further including the properties of the fiber-optic and the wireless channel. Relevant electrical and optical noise contributions have been implemented to the model as well to allow a reliable theoretical description. These results were implemented to a Matlab®-based simulation model in **4**, which allowed to calculate the system link budget and thus the SNR of the experimental RoF systems. Based upon the SNR, the BER was predicted theoretically. The extensive experimental work in this thesis was focused on the realization of broadband photonic millimeter-wave communication systems supporting different application scenarios requiring data rates within the multi-Gb/s range.

The developed system in **5** was based upon external modulation for photonic millimeter-wave generation and coherent detection of the wirelessly transmitted signal. By utilizing the concept of MZM cascading and DSB-CS modulation, multi-Gb/s data transmission was achieved via fiber and wirelessly. If compared to conventional DSB systems, the fiber-optic transmission span was significantly extended. For a data rate of 10.3125 Gb/s, fiber-optic transmission over 6000 m was successfully demonstrated. Furthermore, data transmission of up to 12.5 Gb/s was realized for the first time over relevant wireless transmission lengths. Within the experiments, the wireless path length was as high as 50 m. It was further shown that the wireless path length is extendable to the km-range while utilizing antennas with higher gain. Thus, a typical application scenario of such a system would be a fixed point-to-point link, bridging for instance fiber-optic 10 GbE networks supporting carrier-class availability.

Replacing the coherent receiver architecture with an incoherent approach shown in **6** allowed a more compact system setup. However, the applied envelope detector clearly limited the system performance. Data rates of up to 5 Gb/s have been demonstrated for a wireless path length of 25 m, while the maximum transmission rate was limited to 2.5 Gb/s applying 50 m of wireless transmission. Fiber-optic transmission over more than 40 km at a data rate of 1.25 Gb/s has further been demonstrated. In summary, the system fulfilled the data rate requirements for 1 GbE and OC-48 transmission, allowing utilization within indoor and outdoor application scenarios.

A reliable theoretical model has been deduced in **3** and **4** to predict the performance of the experimental RoF systems in **5** and **6**. A close congruence between experimental results and theoretical prediction has been demonstrated for both systems. This allows design and estimation of the system performance in preposition, as critical components and subsystems can be identified and optimized in advance. In **5**, wireless range extension to the km-range was calculated based upon parameter extraction of experimental results. Simulations utilizing the theoretical model have furthermore shown a very good agreement with these calculations, allowing adequate predictions where experimental data is not accessible.

A further RoF system was presented in **7**, aiming for uncompressed photonic-wireless HDTV transmission. Here, photonic millimeter-wave generation was performed by a purely photonic approach, i.e. by utilizing a prototype MLLD developed within the project. Compared to the previous systems based upon external modulation for photonic up-conversion, several components as for instance LO source or external modulator were no longer required. In conjunction with the applied incoherent receiver a very compact setup was realized. Experiments have been carried out, demonstrating photonic-wireless transmission of up to 5 Gb/s at a wireless path length of 25 m which fully supports the necessary data rates for uncompressed 1080i and 1080p HDTV transmission. The system was furthermore packaged to compact modules and exhibited at the ICT2008 in Lyon for demonstrating uncompressed 1080i HDTV transmission. A ranking under the top ten exhibitions among 200 competitors was achieved.

8.2 Recommendations

For the system reported in **5**, an external synchronization was used to achieve phase locking between the LO source in the external modulation unit and in the wireless receiver. Although this was sufficient for an experimental characterization, a PLL needs to be implemented for a full applicability. The systems discussed in **6** and **7** have utilized an envelope detector limiting the maximum achievable data rate. A replacement with a detector supporting a larger amount of bandwidth would allow higher data rates. For the RoF systems reported in **5** and **6**, a maximum wireless path length of 50 m has

been demonstrated which was limited due to environmental conditions and the remaining power budget as well. However, for real application scenarios longer radio distances are required. This could be achieved by replacing the utilized medium gain horn antennas with high-gain Cassegrain or Gaussian optical lens antennas which are typically designated for such point-to-point links. Further on, the systems need to be upgraded with uplink-capabilities to allow bidirectional communication.

Due to bandwidth limitations some BER characterizations have revealed insufficient physical error rates. Applying FEC techniques would allow error-free operation, depending on FEC technique and uncorrected error rate.

Consumed bandwidths within the experiments partially exceeded the allocated unlicensed frequency range around 60 GHz. Thus, in terms of legal applicability, the spectral efficiency of the systems needs to be improved. In addition, while considering the spectral path loss within the V-band due to atmospheric gaseous attenuation, multi-carrier modulation formats like OFDM may allow a partial compensation of the spectral loss figure to some degree. An experimental result targeting this scenario was recently published in [O33].

Bibliography

[1] "Internet World Stats," 2009. [Online]. Available: www.internetworldstats.com

[2] "Cisco Visual Networking Index - Forecast and Methodology, 2007 - 2012," 2008. [Online]. Available: www.cisco.com

[3] J. D'Ambrosia, "40 gigabit Ethernet and 100 gigabit Ethernet: The development of a flexible architecture," *IEEE Communications Magazine*, vol. 47, no. 3, pp. 8–14, Mar 2009.

[4] C. Cole, B. Huebner, and J. Johnson, "Photonic integration for high-volume, low-cost applications," *IEEE Communications Magazine*, vol. 47, no. 3, pp. 16–22, Mar 2009.

[5] A. Hodzic, "Investigations of high bit rate optical transmission systems employing a channel data rate of 40 Gb/s," Ph.D. dissertation, Technische Universität Berlin, Germany, 2004.

[6] P. Odling, T. Magesacher, S. Host, P. O. Borjesson, M. Berg, and E. Areizaga, "The fourth generation broadband concept," *IEEE Communications Magazine*, vol. 47, no. 1, pp. 62–69, Jan 2009.

[7] J. A. Wells, "Faster Than Fiber: The Future of Multi-Gb/s Wireless," *IEEE Microwave Magazine*, vol. 10, no. 3, pp. 104–112, May 2009.

[8] C. Lim, A. Nirmalathas, M. Bakaul, K.-L. Lee, D. Novak, and R. Waterhouse, "Mitigation strategy for transmission impairments in millimeter-wave radio-over-fiber networks," *Journal of Optical Networking*, vol. 8, no. 2, pp. 201–214, 2009.

[9] *Recommendation ITU-T G.991.2: Single-pair high-speed digital subscriber line transceivers (SHDSL)* , International Telecommunication Union Std., 2003.

[10] *Recommendation ITU-T G.992.5: Asymmetric Digital Subscriber Line (ADSL) transceivers - Extended bandwidth ADSL2 (ADSL2+)*, International Telecommunication Union Std., 2003.

[11] *Recommendation ITU-R J.222: Third-generation transmission systems for interactive cable television services - IP cable modems*, International Telecommunication Union Std., 2007.

[12] (2009) VDSL - das Breitbandnetz der Zukunft. [Online]. Available: www.telekom.com

[13] "FTTH Handbook," FTTH Council Europe, Tech. Rep., Feb 2009.

[14] *Recommendation ITU-T G.984.1: Gigabit-capable passive optical networks (GPON): General characteristics*, International Telecommunication Union Std., 2008.

[15] *IEEE 802.3ah: Ethernet in the First Mile*, Institute of Electrical and Electronics Engineers Std., 2004.

[16] *IEEE P802.3av Task Force: 10Gb/s Ethernet Passive Optical Network*, Institute of Electrical and Electronics Engineers Std., 2009.

[17] B. Skubic, J. Chen, J. Ahmed, L. Wosinska, and B. Mukherjee, "A comparison of dynamic bandwidth allocation for epon, gpon, and next-generation tdm pon," *IEEE Communications Magazine*, vol. 47, no. 3, pp. 40–48, Mar 2009.

[18] M. Kawahata, "Hi-OVIS development project," in *Proceedings of Integrated Optics and Optical Communication, IOOC1977*, 1977, pp. 467–471.

[19] P. W. Shumate, "Fiber-to-the-Home: 1977-2007," *IEEE Journal of Lightwave Technology*, vol. 26, no. 9, pp. 1093–1103, May 2008.

[20] H. Shinohara, "Broadband access in Japan: rapidly growing FTTH market," *IEEE Communications Magazine*, vol. 43, no. 9, pp. 72–78, Sep 2005.

[21] A. Umino, "Experience and Challenges in Collecting Mobile Broadband Statistics in Japan," in *7th World Telecommunication/ICT Indicators Meeting*, Cairo, Egypt, 3–5 Mar 2009.

[22] R. Montagne, "FTTH European Panorama," in *FTTH Council Europe Conference*, Copenhagen, Denmark, 11 Feb 2009.

[23] "The Advantages of Optical Access," FTTH Council Europe, Tech. Rep., 2009.

[24] M. S. Kuran and T. Tugcu, "A survey on emerging broadband wireless access technologies," *Computer Networks*, vol. 51, no. 11, pp. 3013–3046, 2007.

[25] *IEEE 802.11g-2003: Local and metropolitan area networks - Specific requirements Part 11: Wireless LAN Medium Access Control (MAC) and Physical Layer (PHY) Specifications Amendment 4: Further Higher Data Rate Extension in the 2.4 GHz Band*, IEEE Institute of Electrical and Electronics Engineers Std., 2003.

[26] *IEEE 802.11n-2009: Local and metropolitan area networks - Specific requirements Part 11: Wireless LAN Medium Access Control (MAC) and Physical Layer (PHY) specifications Amendment 5: Enhancements for Higher Throughput*, IEEE Institute of Electrical and Electronics Engineers Std., 2009.

[27] *IEEE 802.16-2005: Local and metropolitan area networks - Specific Requirements Part 16: Air Interface for Broadband Wireless Access Systems*, IEEE Institute of Electrical and Electronics Engineers Std., 2005.

[28] *ETSI HiperACCESS: Broadband Radio Access Networks (BRAN); HiperACCESS System Overview*, European Telecommunications Standards Institute Std., 2002.

[29] *ETSI HiperMAN: Broadband Radio Access Networks (BRAN); Functional Requirements for Fixed Wireless Access Systems Below 11 GHz: HIPERMAN Data Link Layer (DLC) Layer*, European Telecommunications Standards Institute Std., 2003.

[30] J. Wells, "Multigigabit wireless technology at 70 GHz, 80 GHz and 90 GHz," RFdesign, Tech. Rep., 2006.

[31] "Millimeter-Wave Communication System," 2009. [Online]. Available: www.asyrmatos.com

[32] Loea corporation, 2009. [Online]. Available: www.loeacom.com

[33] Comotech corporation, 2009. [Online]. Available: www.comotech.com

[34] Proxim Wireless, 2009. [Online]. Available: www.proxim.com

[35] ELVA-1, 2009. [Online]. Available: www.elva-1.com

[36] Rayawave Inc., 2009. [Online]. Available: www.rayawave.com

[37] Gigabeam Corporation, 2009. [Online]. Available: www.gigabeam.com

[38] F. Ivanek, "Mobile backhaul," *IEEE Microwave Magazine*, vol. 10, no. 5, pp. 10–20, Aug 2009.

[39] "Integrated Photonic Millimeter-Wave Functions For Broadband Connectivity," May 2006–Nov 2009. [Online]. Available: www.ist-iphobac.org

[40] H. B. Kim, "Radio over Fiber based Network Architecture," Ph.D. dissertation, Technische Universität Berlin, Germany, 2005.

[41] H. Al-Raweshidy and S. Komaki, Eds., *Radio over Fiber Technologies for Mobile Communication Networks*. Artech House, 2002.

[42] T. Nagatsuma, N. Kukutsu, and Y. Kado, "Photonic Generation of Millimeter and Terahertz Waves and Its Applications," *Automatika*, vol. 49, no. 1, pp. 51–59, 2008.

[43] J. Yao, "Microwave Photonics," *IEEE Journal of Lightwave Technology*, vol. 27, no. 3, pp. 314–335, Feb 2009.

[44] A. Hirata, M. Harada, K. Sato, and T. Nagatsuma, "Low-cost millimeter-wave photonic techniques for Gigabit/s wireless link," *IEICE Transactions on Electronics*, vol. 86, no. 7, pp. 1123–1128, 2003.

[45] A. Malcoci, "Photonische Lokaloszillatoren für Anwendungen in der Terahertz-Radioastronomie," Ph.D. dissertation, Universität Duisburg-Essen, Germany, 2006.

[46] A. J. Seeds and K. J. Williams, "Microwave photonics," *IEEE Journal of Lightwave Technology*, vol. 24, no. 12, pp. 4628–4641, 2006.

[47] L. Ponnampalam, C. C. Renaud, I. F. Lealman, L. Rivers, P. Cannard, M. J. Robertson, F. van Dijk, D. Moodie, A. Enard, F. Blache, M. Goix, F. Mallécot, and A. J. Seeds, "Injection-locked Integrated Twin DBR Lasers for mm-wave Generation," in *European workshop on photonic solutions for wireless, access, and in-house networks*, Duisburg, 18–20 May 2009, pp. 123–126.

[48] J. Harrison and A. Mooradian, "Linewidth and offset frequency locking of external cavity GaAlAs lasers," *IEEE Journal of Quantum Electronics*, vol. 25, no. 6, pp. 1152–1155, 1989.

[49] R. T. Ramos and A. J. Seeds, "Fast heterodyne optical phase-lock loop using double quantum well laser diodes," *Electronics Letters*, vol. 28, no. 1, pp. 82–83, 1992.

[50] U. Gliese, T. N. Nielsen, M. Bruun, E. L. Christensen, K. E. Stubkjzr, and B. Broberg, "A wideband heterodyne optical phase-locked loop for generation of 3-18 GHz microwave carriers," *IEEE Photonics Technology Letters*, vol. 4, no. 8, pp. 936–938, 1992.

[51] A. C. Bordonalli, C. Walton, and A. J. Seeds, "High-performance phase locking of wide linewidth semiconductor lasers by combined use of optical injection locking and optical phase-lock loop," *IEEE Journal of Lightwave Technology*, vol. 17, no. 2, pp. 328–342, 1999.

[52] K. J. Williams, L. Goldberg, R. D. Esman, M. Dagenais, and J. F. Weller, "6-34 GHz offset phase-locking of Nd: YAG 1319 nm nonplanar ring lasers," *Electronics Letters*, vol. 25, no. 18, pp. 1242–1243, 1989.

[53] F. Z. Fan and M. Dagenais, "Optical generation of a megahertz-linewidth microwave signal using semiconductor lasers and a discriminator-aided phase-locked loop," *IEEE Transactions on Microwave Theory and Techniques*, vol. 45, no. 8, pp. 1296–1300, 1997.

[54] H. R. Rideout, J. S. Seregelyi, S. Paquet, and J. Yao, "Discriminator-aided optical phase-lock loop incorporating a frequency down-conversion module," *IEEE Photonics Technology Letters*, vol. 18, no. 21, pp. 2344–2346, 2006.

[55] J. J. O'Reilly, P. M. Lane, and M. H. Capstick, "Optical generation and delivery of modulated mm-waves for mobile communications," *Analogue optical fibre communications*, vol. 1, pp. 229–249, 1995.

[56] A. Ngoma, "Radio-over-Fibre Technology for Broadband Wireless Communication Systems," Ph.D. dissertation, Technische Universiteit Eindhoven, Netherlands, 2005.

[57] L. N. Langley, M. D. Elkin, C. Edge, M. J. Wale, U. Gliese, X. Huang, and A. J. Seeds, "Packaged semiconductor laser optical phase-locked loop (OPLL) for photonic generation, processing and transmission of microwave signals," *IEEE Transactions on Microwave Theory and Techniques*, vol. 47, no. 7, pp. 1257–1264, 1999.

[58] L. Goldberg, H. F. Taylor, J. F. Weller, and D. M. Bloom, "Microwave signal generation with injection-locked laser diodes," *Electronics Letters*, vol. 19, no. 13, pp. 491–493, 1983.

[59] L. Goldberg, A. M. Yurek, H. F. Taylor, and J. F. Weller, "35 GHz microwave signal generation with an injection-locked laser diode," *Electronics Letters*, vol. 21, no. 18, pp. 814–815, 1985.

[60] Y. J. Wen, H. F. Liu, D. Novak, and Y. Ogawa, "Millimeter-wave signal generation from a monolithic semiconductor laser via subharmonic optical injection," *IEEE Photonics Technology Letters*, vol. 12, no. 8, pp. 1058–1060, Aug 2000.

[61] O. Kjebon, R. Schatz, S. Lourdudoss, S. Nilsson, B. Stalnacke, and L. Backbom, "30 GHz direct modulation bandwidth in detuned loaded InGaAsP DBR lasers at 1.55 μm wavelength," *Electronics Letters*, vol. 33, no. 6, pp. 488–489, 1997.

[62] S. K. Hwang, J. M. Liu, and J. K. White, "35-GHz intrinsic bandwidth for direct modulation in 1.3-μm semiconductor lasers subject to strong injection locking," *IEEE Photonics Technology Letters*, vol. 16, no. 4, pp. 972–974, 2004.

[63] X. Zhao, D. Parekh, E. K. Lau, H. K. Sung, M. C. Wu, W. Hofmann, M. C. Amann, and C. J. Chang-Hasnain, "Novel cascaded injection-locked 1.55-μm VCSELs with 66 GHz modulation bandwidth," *Optics Express*, vol. 15, no. 22, pp. 14 810–14 816, 2007.

[64] J. Buus, "Dynamic line broadening of semiconductor lasers modulated at high frequencies," *Electronics Letters*, vol. 21, no. 4, pp. 129–131, 1985.

[65] A. Sudbo, "The frequency chirp of current modulated semiconductor diode lasers," *IEEE Journal of Quantum Electronics*, vol. 22, no. 7, pp. 1006–1008, 1986.

[66] J. J. O'Reilly, P. M. Lane, R. Heidemann, and R. Hofstetter, "Optical generation of very narrow linewidth millimetre wave signals," *Electronics Letters*, vol. 28, pp. 2309–2311, 1992.

[67] J. J. O'Reilly and P. M. Lane, "Remote delivery of video services using mm-waves and optics," *IEEE Journal of Lightwave Technology*, vol. 12, no. 2, pp. 369–375, 1994.

[68] J. J. O'Reilly and P. M. Lane, "Fibre-supported optical generation and delivery of 60 GHz signals," *Electronics Letters*, vol. 30, no. 16, pp. 1329–1330, 1994.

[69] P. Shen, N. J. Gomes, P. A. Davies, W. P. Shillue, P. G. Huggard, and B. N. Ellison, "High-purity millimetre-wave photonic local oscillator generation and delivery," in *IEEE International Topical Meeting on Microwave Photonics, MWP2003*, 2003, pp. 189–192.

[70] D. Chen, H. R. Fetterman, A. Chen, W. H. Steier, L. R. Dalton, W. Wang, and Y. Shi, "Demonstration of 110 GHz electro-optic polymer modulators," *Applied Physics Letters*, vol. 70, pp. 3335–3337, 1997.

[71] L. V. Keldysh, "Behavior of non-metallic crystals in strong electric fields," *Soviet Journal of Experimental and Theoretical Physics*, vol. 6, 1958.

[72] W. Franz, "Einfluss eines elektrischen Feldes auf eine optische Absorptionskante," *Zeitschrift Naturforschung Teil A*, vol. 13, 1958.

[73] F. C. A. Pockels and F. Pockels, *Lehrbuch der Kristalloptik*. BG Teubner, 1906.

[74] H. Chen, "Development of an 80 Gbit/s InP-based Mach-Zehnder Modulator," Ph.D. dissertation, Technische Universität Berlin, Germany, 2007.

[75] T. Ohno, F. Nakajima, T. Furuta, and H. Ito, "240 GHz active mode locked laser diode," *Electronics Letters*, vol. 41, no. 19, pp. 1057–1059, 2005.

[76] K. Sato, "100 GHz optical pulse generation using Fabry-Perot laser under continuous wave operation," *Electronics Letters*, vol. 37, no. 12, pp. 763–764, 2001.

[77] F. van Dijk, A. Enard, X. Buet, F. Lelarge, and G.-H. Duan, "Phase Noise Reduction of a Quantum Dash Mode-Locked Laser in a Millimeter-Wave Coupled Opto-Electronic Oscillator," *IEEE Journal of Lightwave Technology*, vol. 26, no. 15, pp. 2789–2794, Aug 2008.

[78] J. Renaudier, G.-H. Duan, P. Landais, and P. Gallion, "Phase Correlation and Linewidth Reduction of 40 GHz Self-Pulsation in Distributed Bragg Reflector Semiconductor Lasers," *IEEE Journal of Quantum Electronics*, vol. 43, no. 2, pp. 147–156, Feb 2007.

[79] S. Arahira, S. Kutsuzawa, Y. Matsui, D. Kunimatsu, and Y. Ogawa, "Repetition-frequency multiplication of mode-locked pulses using fiber dispersion," *IEEE Journal of Lightwave Technology*, vol. 16, no. 3, pp. 405–410, Mar 1998.

[80] R. Sambaraju, V. Polo, J. L. Corral, and J. Martí, "Ten gigabits per second 16-level quadrature amplitude modulated millimeter-wave carrier generation using dual-drive Mach–Zehnder modulators incorporated photonic-vector modulator," *Optics Letters*, vol. 33, no. 16, pp. 1833–1835, 2008.

[81] "IEEE 802.15 WPAN Task Group 3c (TG3c) Millimeter Wave Alternative PHY," Institute of Electrical and Electronics Engineers, Tech. Rep., 2001.

[82] *IEEE 802.3-2008 Part 3: Carrier Sense Multiple Access with Collision Detection (CSMA/CD) Access Method and Physical Layer Specifications*, Institute of Electrical and Electronics Engineers Std., 2008.

[83] *TC GR-253: Synchronous Optical Network (SONET) Transport Systems: Common Generic Criteria*, Telcordia Technologies Std., 2005.

[84] S. K. Yong and C. C. Chong, "An overview of multigigabit wireless through millimeter wave technology: potentials and technical challenges," *EURASIP Journal on Wireless Communications and Networking*, vol. 2007, no. 1, pp. 1–10, 2007.

[85] N. Guo, R. C. Qiu, S. S. Mo, and K. Takahashi, "60-GHz Millimeter-Wave Radio: Principle, Technology, and New Results," *EURASIP Journal on Wireless Communications and Networking*, vol. 2007, no. 1, pp. 1–8, 2007.

[86] *F2009C00066: Radiocommunications (Low Interference Potential Devices) Class Licence 2000, Class Licence Variation Notice 2008 (No. 1)*, Australian Government, COMLAW Std., 2009.

[87] *RSS-210: Low-power Licence-exempt Radiocommunication Devices (All Frequency Bands)*, Industry Canada Spectrum Management and Telecommunications Std. 7, Jun 2007.

[88] *ECC Recommendation (09)01: Use of the 57-64 GHz Frequency band for Point-to-point Fixed Wireless Access*, Electronic Communications Committee (ECC) within the European Conference of Postal and Telecommunications Administrations (CEPT) Std., 2009.

[89] *ECC Recommendation (05)02: Use of the 64-66 GHz Frequency Band for Fixed Service*, Electronic Communications Committee (ECC) within the European Conference of Postal and Telecommunications Administrations (CEPT) Std., 2005.

[90] *ETSI EN 302 567: Broadband Radio Access Networks (BRAN) and 60 GHz Multiple-Gigabit WAS/RLAN Systems*, European Telecommunications Standards Institute Std., Mar 2009.

[91] *ECMA-387: High Rate 60GHz PHY, MAC and HDMI PAL*, ECMA Std., 2008.

[92] *BNA Mitteilung Nr. 217/2008: Allgemeinzuteilung für Punkt-zu-Punkt Richtfunk im Frequenzbereich 59 - 63 GHz*, Bundesnetzagentur Std., 2008.

[93] *Regulations for enforcement of the radio law 6-4-2 specified low power radio station (11) 59-66 GHz band*, Ministry of Public Management, Home Affairs, Posts and Telecommunication, Japan Std., 2000.

[94] "Frequency allocation comment of 60 GHz band," Ministry of Information and Communication of Korea, Tech. Rep., 2006.

[95] *Code of Federal Regulation, Telecommunication, title 47, chapter 1, part 15.255*, Federal Communication Comission Std., 2004.

[96] A. J. Cooper, "Fibre/radio for the provision of cordless/mobile telephony services in the access network," *Electronics Letters*, vol. 26, no. 24, pp. 2054–2056, Nov 1990.

[97] A. Kaszubowska, P. Anandarajah, and L. P. Barry, "Multifunctional operation of a fiber Bragg grating in a WDM/SCM radio over fiber distribution system," *IEEE Photonics Technology Letters*, vol. 16, no. 2, pp. 605–607, Feb 2004.

[98] G. H. Smith, D. Novak, and C. Lim, "A millimeter-wave full-duplex fiber-radio star-tree architecture incorporating WDM and SCM," *IEEE Photonics Technology Letters*, vol. 10, no. 11, pp. 1650–1652, Nov 1998.

[99] A. Stöhr, K. Kitayama, and D. Jäger, "Full-duplex fiber-optic RF subcarrier transmission using a dual-function modulator/photodetector," *IEEE Transactions on Microwave Theory and Techniques*, vol. 47, no. 7, pp. 1338–1341, Jul 1999.

[100] L. Chen, H. Wen, and S. Wen, "A Radio-Over-Fiber System With a Novel Scheme for Millimeter-Wave Generation and Wavelength Reuse for Up-Link Connection," *IEEE Photonics Technology Letters*, vol. 18, no. 19, pp. 2056–2058, Oct 2006.

[101] A. Stöhr, K. Kitayama, and T. Kuri, "Fiber-length extension in an optical 60-GHz transmission system using an EA-modulator with negative chirp," *IEEE Photonics Technology Letters*, vol. 11, no. 6, pp. 739–741, Jun 1999.

[102] G. H. Smith, D. Novak, and Z. Ahmed, "Overcoming chromatic-dispersion effects in fiber-wireless systems incorporating external modulators," *IEEE Transactions on Microwave Theory and Techniques*, vol. 45, no. 8, pp. 1410–1415, 1997.

[103] L. Noel, D. Wake, D. G. Moodie, D. D. Marcenac, L. D. Westbrook, and D. Nesset, "Novel techniques for high-capacity 60-GHz fiber-radio transmission systems," *IEEE Transactions on Microwave Theory and Techniques*, vol. 45, no. 8, pp. 1416–1423, Aug 1997.

[104] T. Kuri, K. Kitayama, and Y. Ogawa, "Fiber-optic millimeter-wave uplink system incorporating remotely fed 60-GHz-band optical pilot tone," *IEEE Transactions on Microwave Theory and Techniques*, vol. 47, no. 7, pp. 1332–1337, Jul 1999.

[105] T. Kuri, K. Kitayama, A. Stöhr, and Y. Ogawa, "Fiber-optic millimeter-wave downlink system using 60 GHz-band external modulation," *IEEE Journal of Lightwave Technology*, vol. 17, no. 5, pp. 799–806, May 1999.

[106] K. Kitayama, A. Stöhr, T. Kuri, R. Heinzelmann, D. Jäger, and Y. Takahashi, "An approach to single optical component antenna base stations for broad-band millimeter-wave fiber-radio access systems," *IEEE Transactions on Microwave Theory and Techniques*, vol. 48, no. 12, pp. 2588–2595, Dec 2000.

[107] J. Ma, C. Yu, Z. Zhou, and J. Yu, "Optical mm-wave generation by using external modulator based on optical carrier suppression," *Optics Communications*, vol. 268, no. 1, pp. 51–57, Dec 2006.

[108] A. Wiberg, P. Perez-Millan, M. V. Andres, P. A. Andrekson, and P. O. Hedekvist, "Fiber-optic 40-GHz mm-wave link with 2.5-Gb/s data transmission," *IEEE Photonics Technology Letters*, vol. 17, no. 9, pp. 1938–1940, Sep 2005.

[109] J. Yu, Z. Jia, L. Yi, Y. Su, G.-K. Chang, and T. Wang, "Optical millimeter-wave generation or up-conversion using external modulators," *IEEE Photonics Technology Letters*, vol. 18, no. 1, pp. 265–267, Jan 2006.

[110] Z. Jia, J. Yu, and G.-K. Chang, "A full-duplex radio-over-fiber system based on optical carrier suppression and reuse," *IEEE Photonics Technology Letters*, vol. 18, no. 16, pp. 1726–1728, Aug 2006.

[111] L. Chen, Y. Shao, X. Lei, H. Wen, and S. Wen, "A Novel Radio-Over-Fiber System With Wavelength Reuse for Upstream Data Connection," *IEEE Photonics Technology Letters*, vol. 19, no. 6, pp. 387–389, Mar 2007.

[112] Z. Jia, J. Yu, D. Boivin, M. Haris, and G.-K. Chang, "Bidirectional ROF Links Using Optically Up-Converted DPSK for Downstream and Remodulated OOK for Upstream," *IEEE Photonics Technology Letters*, vol. 19, no. 9, pp. 653–655, May 2007.

[113] C.-T. Lin, W.-R. Peng, P.-C. Peng, J. Chen, C.-F. Peng, B.-S. Chiou, and S. Chi, "Simultaneous Generation of Baseband and Radio Signals Using Only One Single-Electrode Mach-Zehnder Modulator With Enhanced Linearity," *IEEE Photonics Technology Letters*, vol. 18, no. 23, pp. 2481–2483, Dec 2006.

[114] U. Gliese, S. Norskov, and T. N. Nielsen, "Chromatic dispersion in fiber-optic microwave and millimeter-wavelinks," *IEEE Transactions on Microwave Theory and Techniques*, vol. 44, no. 10, pp. 1716–1724, 1996.

[115] M. Sieben, J. Conradi, and D. E. Dodds, "Optical single sideband transmission at 10 Gb/s using only electrical dispersion compensation," *IEEE Journal of Lightwave Technology*, vol. 17, no. 10, pp. 1742–1749, Oct 1999.

[116] J. Han, B.-J. Seo, Y. Han, B. Jalali, and H. Fetterman, "Reduction of fiber chromatic dispersion effects in fiber-wireless and photonic time-stretching system using polymer modulators," *IEEE Journal of Lightwave Technology*, vol. 21, no. 6, pp. 1504–1509, Jun 2003.

[117] J. Capmany, B. Ortega, A. Martinez, D. Pastor, M. Popov, and P. Y. Fonjallaz, "Multi-wavelength single sideband modulation for WDM radio-over-fiber systems using a fiber grating array tandem device," *IEEE Photonics Technology Letters*, vol. 17, no. 2, pp. 471–473, Feb 2005.

[118] A. Stöhr, R. Heinzelmann, A. Malcoci, and D. Jäger, "Optical heterodyne millimeter-wave generation using 1.55-μm traveling-wave photodetectors," *IEEE Transactions on Microwave Theory and Techniques*, vol. 49, no. 10, pp. 1926–1933, Oct 2001.

[119] A. Stöhr, R. Heinzelmann, K. Hagedorn, R. Gusten, F. Schafer, H. Stuer, F. Siebe, P. van der Wal, V. Krozer, M. Feiginov, and D. Jäger, "Integrated 460 GHz photonic transmitter module," *Electronics Letters*, vol. 37, no. 22, pp. 1347–1348, Oct 2001.

[120] A. Hirata and T. Nagatsuma, "120 GHz millimetre-wave antenna for integrated photonic transmitter," *Electronics Letters*, vol. 37, no. 24, pp. 1460–1461, Nov 2001.

[121] J. B. Georges, D. M. Cutrer, M.-H. Kiang, and K. Y. Lau, "Multichannel millimeter wave subcarrier transmission by resonant modulation of monolithic semiconductor lasers," *IEEE Photonics Technology Letters*, vol. 7, no. 4, pp. 431–433, Apr 1995.

[122] R.-P. Braun, G. Grosskopf, H. Heidrich, C. von Helmolt, R. Kaiser, K. Kruger, U. Kruger, D. Rohde, F. Schmidt, R. Stenzel, and D. Trommer, "Optical microwave generation and transmission experiments in the 12- and 60-GHz region for wireless communications," *IEEE Transactions on Microwave Theory and Techniques*, vol. 46, no. 4, pp. 320–330, Apr 1998.

[123] M. Ogusu, K. Inagaki, and Y. Mizuguchi, "400 Mbit/s BPSK data transmission at 60 GHz-band mm-wave using a two-mode injection-locked Fabry-Perot slave laser," in *IEEE International Topical Meeting on Microwave Photonics, MWP2000*, 2000, pp. 31–34.

[124] Y.-K. Seo, J.-H. Seo, and W.-Y. Choi, "60-GHz radio-on-fiber distribution of 2 x 622 Mb/s WDM channels using remote photonic-frequency upconversion," *Microwave and Optical Technology Letters*, vol. 39, no. 3, pp. 201–203, Aug 2003.

[125] A. Hirata, M. Harada, and T. Nagatsuma, "120-GHz wireless link using photonic techniques for generation, modulation, and emission of millimeter-wave signals," *IEEE Journal of Lightwave Technology*, vol. 21, no. 10, pp. 2145–2153, Oct 2003.

[126] T. Ohno, F. Nakajima, T. Furuta, and H. Ito, "A 240-GHz active mode-locked laser diode for ultra-broadband fiber-radio transmission systems," in *Optical Fiber Communication Conference, OFC2005*, Mar 2005, pp. 1–3.

[127] A. Hirata, T. Kosugi, H. Takahashi, R. Yamaguchi, F. Nakajima, T. Furuta, H. Ito, H. Sugahara, Y. Sato, and T. Nagatsuma, "120-GHz-band millimeter-wave photonic wireless link for 10-Gb/s data transmission," *IEEE Transactions on Microwave Theory and Techniques*, vol. 54, no. 5, pp. 1937–1944, May 2006.

[128] J. Yu, J. Hu, D. Qian, Z. Jia, G. K. Chang, and T. Wang, "Transmission of microwave-photonics generated 16Gbit/s super broadband OFDM signals in radio-over-fiber system," in *Optical Fiber Communication Conference, OFC2008*, Feb 2008, pp. 1–3.

[129] Q. Chang, T. Ye, and Y. Su, "Generation of optical carrier suppressed-differential phase shift keying (OCS-DPSK) format using one dual-parallel Mach-Zehnder modulator in radio over fiber systems," *Optics Express*, vol. 16, no. 14, pp. 10 421–10 426, 2008.

[130] R. W. Ridgway and D. W. Nippa, "Generation and Modulation of a 94-GHz Signal Using Electrooptic Modulators," *IEEE Photonics Technology Letters*, vol. 20, no. 8, pp. 653–655, Apr 2008.

[131] T. Taniguchi, N. Sakurai, K. Kumozaki, and T. Imai, "Full-duplex 1.0 Gbit/s Data Transmission over 60 GHz Radio-On-Fiber Access System based on the Loop-Back Optical Heterodyne Technique," *IEEE Journal of Lightwave Technology*, vol. 26, no. 13, pp. 1765–1776, 2008.

[132] A. J. Seeds, M. J. Fice, C.-P. Liu, L. Ponnampalam, F. Pozzi, C. C. Renaud, E. Rouvalis, and R. J. Steed, "New Applications for Microwave Photonics," in *IEEE LEOS annual meeting*, 2009.

[133] T. Nagatsuma, H.-J. Song, Y. Fujimoto, K. Miyake, A. Hirata, K. Ajito, A. Wakatsuki, T. Furuta, N. Kukutsu, and Y. Kado, "Giga-bit Wireless Link Using 300-400 GHz Bands," in *IEEE International Topical Meeting on Microwave Photonics, MWP2009*, Valencia, Spain, 14–16 Oct 2009.

[134] I. G. Insua, D. Plettemeier, and C. G. Schaffer, "Simple remote heterodyne RoF system for Gbps wireless access," in *IEEE International Topical Meeting on Microwave Photonics, MWP2009*, Valencia, Spain, 14–16 Oct 2009.

[135] A. Ngoma, M. Sauer, F. Annunziata, W.-J. Jiang, P.-T. Shih, C.-T. Lin, J. Chen, and S. Chi, "14 Gbps 60 GHz RoF Link Employing a Simple System Architecture and OFDM Modulation," in *IEEE International Topical Meeting on Microwave Photonics, MWP2009*, Valencia, Spain, 14–16 Oct 2009.

[136] C.-T. Lin, E.-Z. Wong, W.-J. Jiang, P.-T. Shin, J. Chen, and S. Chi, "28-Gb/s 16-QAM OFDM radio-over-fiber system within 7-GHz license-free band at 60 GHz employing all-optical up-conversion," in *Conference on Lasers and Electro-Optics, CLEO2009*, Jun 2009, pp. 1–2.

[137] A. Hirata, H. Takahashi, R. Yamaguchi, T. Kosugi, K. Murata, T. Nagatsuma, N. Kukutsu, and Y. Kado, "Transmission Characteristics of 120-GHz-Band Wireless Link Using Radio-on-Fiber Technologies," *IEEE Journal of Lightwave Technology*, vol. 26, no. 15, pp. 2338–2344, Aug 2008.

[138] C. H. Cox, *Analog optical links - Theory and practice*. Cambridge University Press, 2004.

[139] S. Dubovitsky, W. H. Steier, S. Yegnanarayanan, and B. Jalali, "Analysis and improvement of Mach-Zehnder modulator linearity performance for chirped and tunable optical carriers," *IEEE Journal of Lightwave Technology*, vol. 20, no. 5, pp. 886–891, May 2002.

[140] M. T. Abuelmaatti, "Large Signal Analysis of the Mach-Zehnder Modulator with Variable BIAS," *Proceedings of the National Science Council of ROC (Part A)*, vol. 25, no. 4, pp. 254–258, 2001.

[141] C. H. Cox, G. E. Betts, and L. M. Johnson, "An analytic and experimental comparison of direct and external modulation in analog fiber-optic links," *IEEE Transactions on Microwave Theory and Techniques*, vol. 38, no. 5, pp. 501–509, May 1990.

[142] D. Marpaung, "High dynamic range analog photonic links: design and implementation," Ph.D. dissertation, University of Twente, Netherlands, Aug 2009.

[143] G. P. Agrawal, *Lightwave Technology: Telecommunication Systems*. John Wiley & Sons, 2005.

[144] W. R. White, M. Dueser, W. A. Reed, and T. Onishi, "Intermodal dispersion and mode coupling in perfluorinated graded-index plastic optical fiber," *IEEE Photonics Technology Letters*, vol. 11, no. 8, pp. 997–999, 1999.

[145] C. D. Poole, R. W. Tkach, A. R. Chraplyvy, and D. A. Fishman, "Fading in lightwave systems due to polarization-mode dispersion," *IEEE Photonics Technology Letters*, vol. 3, no. 1, pp. 68–70, Jan 1991.

[146] L. E. Nelson, "Challenges of 40 Gb/s WDM transmission," in *Optical Fiber Communication Conference, OFC2001*, 2001.

[147] H. Sunnerud, M. Karlsson, C. Xie, and P. A. Andrekson, "Polarization-mode dispersion in high-speed fiber-optic transmission systems," *IEEE Journal of Lightwave Technology*, vol. 20, no. 12, pp. 2204–2219, 2002.

[148] G. P. Agrawal, *Nonlinear fiber optics*. Springer, 1995.

[149] J. Park, W. V. Sorin, and K. Y. Lau, "Elimination of the fibre chromatic dispersion penalty on 1550 nm millimetre-wave optical transmission," *Electronics Letters*, vol. 33, no. 6, pp. 512–513, 1997.

[150] K. Hill and G. Meltz, "Fiber Bragg grating technology fundamentals and overview," *IEEE Journal of Lightwave Technology*, vol. 15, no. 8, pp. 1263–1276, 1997.

[151] F. Ouellette, P. A. Krug, T. Stephens, G. Dhosi, and B. Eggleton, "Broadband and WDM dispersion compensation using chirped sampled fibre Bragg gratings," *Electronics Letters*, vol. 31, no. 11, pp. 899–901, 1995.

[152] M. D. Feuer, S. Y. Huang, S. L. Woodward, O. Coskun, and M. Boroditsky, "Electronic dispersion compensation for a 10-Gb/s link using a directly modulated laser," *IEEE Photonics Technology Letters*, vol. 15, no. 12, pp. 1788–1790, 2003.

[153] F. Cariali, F. Martini, P. Chiappa, and R. Ballentin, "Electronic compensation of PMD and chromatic dispersion with an IC in 10 Gbit/s transmission system," *Electronics Letters*, vol. 36, no. 10, pp. 889–891, 2000.

[154] H. Chi and J. Yao, "Frequency Quadrupling and Upconversion in a Radio Over Fiber Link," *IEEE Journal of Lightwave Technology*, vol. 26, no. 15, pp. 2706–2711, 2008.

[155] J. L. Corral, J. Marti, and J. M. Fuster, "General expressions for IM/DD dispersive analog optical links with external modulation or optical up-conversion in a Mach-Zehnder electrooptical modulator," *IEEE Transactions on Microwave Theory and Techniques*, vol. 49, no. 10, pp. 1968–1976, Oct 2001.

[156] J. M. Fuster, J. Marti, J. L. Corral, V. Polo, and F. Ramos, "Generalized study of dispersion-induced power penalty mitigation techniques in millimeter-wave fiber-optic links," *IEEE Journal of Lightwave Technology*, vol. 18, no. 7, pp. 933–940, Jul 2000.

[157] G. Ning and P. Shum, "Dispersion induced power fading for radio frequency signals and its application for fast online PMD and CD monitoring," *Applied Physics B*, vol. 88, no. 1, pp. 93–99, 2007.

[158] H. Schmuck, "Comparison of optical millimetre-wave system concepts with regard to chromatic dispersion," *Electronics Letters*, vol. 31, no. 21, pp. 1848–1849, Oct 1995.

[159] J. M. Fuster, J. Marti, and J. L. Corral, "Chromatic dispersion effects in electro-optical upconverted millimetre-wave fibre optic links," *Electronics Letters*, vol. 33, no. 23, pp. 1969–1970, Nov 1997.

[160] F. van Dijk, "Report on mode-locked laser modules for OEO and system evaluation," IPHOBAC deliverable report D334, Tech. Rep., 2009.

[161] B. Charbonnier, M. Huchard, S. Constant, S. Formont, V. Polo, and R. Sambaraju, "Report on the impact on the system applications," IPHOBAC deliverable report D222, Tech. Rep., 2007.

[162] N. Choudhury, "Optical devices for high speed optical communications," Ph.D. dissertation, The University of Connectitut, U.S.A., 2000.

[163] H. Haug and H. Haken, "Theory of noise in semiconductor laser emission," *Zeitschrift für Physik A*, vol. 204, no. 3, pp. 262–275, 1967.

[164] K. I. Kallimani and M. J. O'Mahony, "Relative intensity noise for laser diodes with arbitrary amounts of optical feedback," *IEEE Journal of Quantum Electronics*, vol. 34, no. 8, pp. 1438–1446, Aug 1998.

[165] I. Joindot, "Measurement of relative intensity noise (RIN) in semiconductor lasers," *Journal de Physique III*, vol. 2, no. 9, pp. 1591–1603, 1992.

[166] R. C. Steele, G. R. Walker, and N. G. Walker, "Sensitivity of optically preamplified receivers with optical filtering," *IEEE Photonics Technology Letters*, vol. 3, no. 6, pp. 545–547, Jun 1991.

[167] R. K. Singh, R. Srivastava, and Y. N. Singh, "AWG and EDFA based optical packet switch using feedback shared loop buffer memory," *Optical and Quantum Electronics*, vol. 39, no. 14, pp. 1153–1165, 2007.

[168] N. A. Olsson, "Lightwave systems with optical amplifiers," *IEEE Journal of Lightwave Technology*, vol. 7, no. 7, pp. 1071–1082, Jul 1989.

[169] G. R. Walker, R. C. Steele, and N. G. Walker, "Optical amplifier noise figure in a coherent optical transmission system," *IEEE Journal of Lightwave Technology*, vol. 8, no. 9, pp. 1409–1413, Sep 1990.

[170] J. Schönthier, "The 60GHz channel and its modelling," IST Broadway, Tech. Rep., 2003.

[171] C. Kopp, "TROPPO - A Tropospheric Propagation Simulator," Monash University, Australia, Tech. Rep., 2004.

[172] *Recommendation ITU-R P.840-3: Attenuation due to clouds and fog*, International Telecommunication Union Std., 1999.

[173] D. D. Hodges, R. J. Watson, and G. Wyman, "An attenuation time series model for propagation forecasting," *IEEE Transactions on Antennas and Propagation*, vol. 54, no. 6, pp. 1726–1733, Jun 2006.

[174] H. T. Friis, "A note on a simple transmission formula," *Proceedings of the IRE*, vol. 34, no. 5, pp. 254–256, 1946.

[175] H. Hashemi, "The indoor radio propagation channel," *Proceedings of the IEEE*, vol. 81, no. 7, pp. 943–968, 1993.

[176] T. Rappaport, *Wireless communications: principles and practice*. Prentice Hall, 2001.

[177] J. Detlefsen and U. Siart, *Grundlagen der Hochfrequenztechnik*. Oldenbourg Wissenschaftsverlag, 2006.

[178] A. G. Siamarou, "Wideband Propagation Measurements and Channel Implications for Indoor Broadband Wireless Local Area Networks at the 60 GHz Band," *Wireless Personal Communications*, vol. 27, no. 1, pp. 89–98, 2003.

[179] H. Yang, P. F. M. Smulders, and M. H. A. J. Herben, "Channel Characteristics and Transmission Performance for Various Channel Configurations at 60 GHz," *EURASIP Journal on Wireless Communications and Networking*, vol. 2007, no. 1, pp. 1–15, 2007.

[180] R. Janaswamy, "An indoor pathloss model at 60 GHz based on transport theory," *IEEE Antennas and Wireless Propagation Letters*, vol. 5, no. 1, pp. 58–60, 2006.

[181] *Recommendation ITU-R P.676-6: Attenuation by atmospheric gases*, International Telecommunication Union Std., 2005.

[182] *Recommendation ITU-R P.1411: Propagation Data and Prediction Methods for the Planning of Short-range Outdoor Radiocommunication Systems and Radio Local Area Networks in the Frequency Range 300 MHz to 100 GHz*, International Telecommunication Union Std., 1999.

[183] *Recommendation ITU-R P.676-4: Attenuation by atmospheric gases*, International Telecommunication Union Std., 1999.

[184] T. Maseng and P. Bakken, "A stochastic dynamic model of rain attenuation," *IEEE Transactions on Communications*, vol. 29, no. 5, pp. 660–669, 1981.

[185] E. Matricciani, "Physical-mathematical model of the dynamics of rain attenuation based on rain rate time series and a two-layer vertical structure of precipitation," *Radio Science*, vol. 31, no. 2, pp. 281–295, 1995.

[186] R. Crane, "Prediction of attenuation by rain," *IEEE Transactions on Communications*, vol. 28, no. 9, pp. 1717–1733, 1980.

[187] *Recommendation ITU-R P.838-3: Specific attenuation model for rain for use in prediction methods*, International Telecommunication Union Std., 2005.

[188] A. W. Rudge, K. Milne, A. D. Olver, and P. Knight, Eds., *The handbook of antenna design*. Institution of Electrical Engineers, 1983.

[189] G. Wade, *Signal coding and processing*. Cambridge University Press, 1994.

[190] D. Jäger, *DVB - Digitale Fernsehtechnik*. Springer, 2008.

[191] F. Xiong, *Digital Modulation Techniques*. Artech House, 2000.

[192] J. R. Barry, E. A. Lee, and D. G. Messerschmitt, *Digital Communication*, 3rd ed. Springer, 2004.

[193] K. Ikeda, T. Kuri, and K. Kitayama, "Simultaneous three-band modulation and fiber-optic transmission of 2.5-Gb/s baseband, microwave-, and 60-GHz-band signals on a single wavelength," *IEEE Journal of Lightwave Technology*, vol. 21, no. 12, pp. 3194–3202, Dec 2003.

[194] "ICT 2008," 2008, Lyon, France. [Online]. Available: http://ec.europa.eu/information_society/events/ict/2008

Own Publications

[O1] M. Weiß, A. Stöhr, A. Malcoci, A. G. Steffan, D. Trommer, A. Umbach, and D. Jäger, "Ultra-Wideband Photonic Millimeter-Wave Synthesizers with Coaxial (DC-110GHz) and Rectangular Waveguide (70-115GHz) Output Ports," in *ISIS-IPHOBAC Summer School & Workshop 2007*, Budapest, Hungary, 16–18 May 2007.

[O2] M. Weiß, A. Stöhr, A. Malcoci, A. G. Steffan, and D. Jäger, "Ultra-Wideband Photonic Millimeter-Wave Synthesizers with Coaxial (DC-110GHz) and Rectangular Waveguide (69-112GHz) Output Ports," in *33th European Conference on Optical Communication, ECOC2007*, 16–20 Sep 2007.

[O3] M. Weiß, A. G. Steffan, and L. Pavlovic, "Report on First Packages for Antenna-Integrated Photomixers," IPHOBAC deliverable report D461, Tech. Rep., Sep 2007.

[O4] A. Poloczek, M. Weiß, S. Fedderwitz, A. Stöhr, W. Prost, D. Jäger, and F.-J. Tegude, "Integrated InGaAs pin-diode on exactly oriented silicon (001) substrate suitable for 10 Gbit/s digital applications," in *20th Annual Meeting of the IEEE Lasers and Electro-Optics Society, LEOS2007*, Oct 2007, pp. 180–181.

[O5] A. Stöhr, M. Weiß, A. Malcoci, A. G. Steffan, D. Trommer, A. Umbach, and D. Jäger, "Wideband photonic millimeter-wave synthesizer using a high-power pin waveguide photodiode," in *37th European Microwave Conference, EUMC2007*, 9–12 Oct 2007, pp. 588–591.

[O6] A. Stöhr, M. Weiß, V. Polo, R. Sambaraju, J. L. Corral, J. Marti, M. Huchard, I. Siaud, S. Fedderwitz, and D. Jäger, "60GHz Radio-over-Fiber Techniques for 10Gb/s Broadband Wireless Transmission," in *20th Wireless World Research Forum, WWRF20*, Ottawa, Canada, 22–24 Apr 2008.

[O7] A. Stöhr, M. Weiß, M. Huchard, B. Charbonnier, S. Fedderwitz, and D. Jäger, "60 GHz Wireless Photonic Link System for 12.5Gb/s Data Transmission," in *ITG Fachbericht Photonische Netze*, vol. 207, Leipzig, Germany, 28–29 Apr 2008, pp. 101–104.

[O8] K. H. Tan, S. F. Yoon, W. K. Loke, S. Wicaksono, T. K. Ng, K. L. Lew, A. Stöhr, S. Fedderwitz, M. Weiß, D. Jäger, N. Saadsaoud, E. Dogheche, D. Decoster, and J. Chazelas, "High responsivity GaNAsSb p-i-n photodetectors at 1.3μm grown by

radio-frequency nitrogen plasma-assisted molecular beam epitaxy," *Optics Express*, vol. 16, no. 11, pp. 7720–7725, May 2008.

[O9] M. Weiß, A. Stöhr, M. Huchard, S. Fedderwitz, V. Rymanov, B. Charbonnier, and D. Jäger, "Broadband 60GHz Wireless Radio-over-Fibre System for up to 12.5Gb/s Wireless Transmission," in *ISIS Summer School & Workshop 2008*, Stockholm, Sweden, 2–4 Jun 2008.

[O10] V. Rymanov, A. Stöhr, S. Fedderwitz, S. Babiel, and M. Weiß, "Report on design and fabrication of antenna integrated TW-photomixer compliant with end-users requirements and package specifications provided in T4.6," IPHOBAC deliverable report D414, Tech. Rep., Jul 2008.

[O11] M. Weiß, V. Rymanov, A. G. Steffan, G. Tsianos, L. Pavlovic, and L. Naglic, "Report on First Packaged 30-300GHz Photomixers," IPHOBAC milestone report M461, Tech. Rep., Jul 2008.

[O12] S. Fedderwitz, A. Stöhr, S. F. Yoon, K. H. Tan, M. Weiß, W. K. Loke, A. Poloczek, S. Wicaksono, and D. Jäger, "Multigigabit 1.3μm GaNAsSb/GaAs Photodetectors," *Applied Physics Letters*, vol. 93, no. 3, pp. 033 509 (1–3), Jul 2008.

[O13] M. Weiß, M. Huchard, A. Stöhr, B. Charbonnier, S. Fedderwitz, and D. Jäger, "60-GHz Photonic Millimeter-Wave Link for Short- to Medium-Range Wireless Transmission Up to 12.5 Gb/s," *IEEE Journal of Lightwave Technology*, vol. 26, no. 15, pp. 2424–2429, Aug 2008, invited.

[O14] M. Huchard, M. Weiß, A. Pizzinat, S. Meyer, P. Guignard, and B. Charbonnier, "Ultra-Broadband Wireless Home Network Based on 60-GHz WPAN Cells Interconnected via RoF," *IEEE Journal of Lightwave Technology*, vol. 26, no. 15, pp. 2364–2372, Aug 2008, invited.

[O15] A. Stöhr, C. C. Renaud, D. Moodie, A. G. Steffan, L. Pavlovic, D. Jäger, A. J. Seeds, M. Robertson, A. Umbach, M. Vidmar, M. Weiß, V. Rymanov, S. Fedderwitz, G. Tsianos, and L. Naglic, "Optical Millimeter-Wave Generation using 1.55μm Photodiodes with and without Integrated Antennas," in *2008 URSI General Assembly*, Chicago, USA, 7–16 Aug 2008, invited.

[O16] M. Weiß, A. G. Steffan, S. Fedderwitz, G. Tsianos, A. Stöhr, and D. Jäger, "Highly-Compact Fibre-Optic Package for 30-300GHz Wireless Transmitter Modules," in *2nd Electronics System-Integration Technology Conference, ESTC2008*, London, UK, 1–4 Sep 2008.

[O17] M. Weiß, A. Stöhr, M. Huchard, S. Fedderwitz, B. Charbonnier, V. Rymanov, S. Babiel, and D. Jäger, "60GHz Radio-over-Fibre Wireless System for Bridging 10Gb/s Ethernet Links," in *34th European Conference on Optical Communication, ECOC2008*, Brussels, Belgium, 21–25 Sep 2008.

[O18] S. Fedderwitz, V. Rymanov, M. Weiß, A. Stöhr, D. Jäger, A. G. Steffan, and A. Umbach, "Ultra-Broadband and Low Phase Noise Photonic Millimeter-Wave Generation," in *IEEE International Topical Meeting on Microwave Photonics, MWP2008*, Gold Coast, Australia, 1–3 Oct 2008.

[O19] B. Charbonnier, P. Chanclou, J. L. Corral, G.-H. Duan, C. Gonzalez, M. Huchard, D. Jäger, F. Lelarge, J. Marti, L. Naglic, L. Pavlovic, V. Polo, R. Sambaraju, A. G. Steffan, A. Stöhr, M. Thual, A. Umbach, F. van Dijk, M. Vidmar, and M. Weiß, "Photonics for broadband radio communications at 60 GHz in access and home networks," in *IEEE International Topical Meeting on Microwave Photonics, MWP2008*, Gold Coast, Australia, 1–3 Oct 2008, plenary, invited.

[O20] M. Huchard, P. Chanclou, B. Charbonnier, F. van Dijk, G.-H. Duan, C. Gonzalez, F. Lelarge, M. Thual, M. Weiß, and A. Stöhr, "60 GHz Radio Signal Up-conversion and Transport Using a Directly Modulated Mode-Locked Laser," in *IEEE International Topical Meeting on Microwave Photonics, MWP2008*, Gold Coast, Australia, 1–3 Oct 2008.

[O21] V. Rymanov, M. Weiß, A. Stöhr, and S. Fedderwitz, "Calibration report of antenna integrated TW-photomixer," IPHOBAC deliverable report D415, Tech. Rep., Jan 2009.

[O22] V. Rymanov, M. Weiß, A. G. Steffan, S. Fedderwitz, A. Stöhr, and D. Jäger, "An Antenna-Integrated Photonic Millimeter-Wave Transmitter," in *European workshop on photonic solutions for wireless, access, and in-house networks*, Duisburg, 18–20 May 2009, pp. 77–80.

[O23] M. Weiß, A. Stöhr, S. Fedderwitz, V. Rymanov, and B. Charbonnier, "Photonic Millimeter-Wave System for Broadband Wireless Access," in *European workshop on photonic solutions for wireless, access, and in-house networks*, Duisburg, 18–20 May 2009, pp. 123–126.

[O24] V. Rymanov, S. Fedderwitz, M. Weiß, A. Stöhr, and D. Jäger, "Photonic Millimeter-Wave Generation for Ultra-Broadband and Low Phase Noise Applications," in *5th Joint Symposium on Opto- & Microelectronic Devices and Circuits, SODC 2009*, Beijing, 9–15 May 2009, pp. 77–81.

[O25] V. Rymanov, M. Weiß, A. Stöhr, and S. Fedderwitz, "Improved output power antenna integrated photomixer fabricated and ready for partners," IPHOBAC milestone report M414, Tech. Rep., May 2009.

[O26] S. F. Yoon, K. H. Tan, W. K. Loke, S. Wicaksono, K. L. Lew, T. K. Ng, Z. Xu, Y. K. Sim, A. Stöhr, S. Fedderwitz, M. Weiß, O. Ecin, A. Poloczek, A. Malcoci, D. Jäger, N. Saadsaoud, E. Dogheche, M. Zegaoui, J. F. Lampin, D. Decoster, C. Tripon-Canseliet, S. Faci, J. Chazelas, J. A. Gupta, and S. P. McAlister, "Recent Progress in Dilute Nitride-antimonide Materials for Photonic and Electronic Applications," *ECS*

Transactions on Dielectric and Semiconductor Materials, Devices, and Processing, vol. 19, no. 3, pp. 5–29, May 2009.

[O27] K. H. Tan, S. F. Yoon, S. Fedderwitz, A. Stöhr, W. K. Loke, S. Wicaksono, T. K. Ng, M. Weiß, A. Poloczek, V. Rymanov, A. S. Patra, E. Tangdiongga, and D. Jäger, "14-GHz GaNAsSb Unitraveling-Carrier 1.3μm Photodetectors Grown by RF Plasma-Assisted Nitrogen Molecular Beam Epitaxy," *IEEE Electron Device Letters*, vol. 30, no. 6, pp. 590–592, Jun 2009.

[O28] M. Weiß, V. Rymanov, A. G. Steffan, G. Tsianos, A. Stöhr, and D. Jäger, "Calibration report of packaged 300GHz photomixers," IPHOBAC deliverable report D462, Tech. Rep., Jun 2009.

[O29] S. Fedderwitz, A. Stöhr, K. H. Tan, S. F. Yoon, M. Weiß, A. Poloczek, W. K. Loke, S. Wicaksono, T. K. Ng, V. Rymanov, A. S. Patra, E. Tangdiongga, and D. Jäger, "1.3-μm GaNAsSb-GaAs UTC-Photodetectors for 10-Gigabit Ethernet Links," *IEEE Photonics Technology Letters*, vol. 21, no. 13, pp. 911–913, Jul 2009.

[O30] A. Stöhr, A. Akrout, R. Buß, B. Charbonnier, F. van Dijk, A. Enard, S. Fedderwitz, D. Jäger, M. Huchard, F. Lecoche, J. Marti, R. Sambaraju, A. G. Steffan, A. Umbach, and M. Weiß, "60 GHz Radio-over-Fiber Technologies for Broadband Wireless Services," *OSA Journal of Optical Networking*, vol. 8, no. 5, pp. 471–487, Aug 2009, invited.

[O31] J. Honecker, M. Weiß, L. Ponnampalam, and A. G. Steffan, "Calibration report of packaged 110GHz photodetectors," IPHOBAC deliverable report D452, Tech. Rep., Aug 2009.

[O32] B. Charbonnier, F. Lecoche, I. Siaud, M. Weiß, S. Fedderwitz, A. Stöhr, and R. Sambaraju, "Report on enhanced solutions and performances," IPHOBAC deliverable report D223, Tech. Rep., Sep 2009.

[O33] M. Weiß, A. Stöhr, F. Lecoche, and B. Charbonnier, "27 Gbit/s Photonic Wireless 60 GHz Transmission System using 16-QAM OFDM," in *IEEE International Topical Meeting on Microwave Photonics, MWP2009*, Valencia, Spain, 14–16 Oct 2009, post-deadline.

[O34] B. Charbonnier, F. Lecoche, M. Weiß, A. Stöhr, F. van Dijk, A. Enard, F. Blache, M. Goix, F. Mallecot, D. G. Moodie, A. Borghesani, and C. W. Ford, "Ultra-wideband radio-over-fiber techniques and networks," in *Optical Fiber Communication Conference, OFC2010*, San Diego, USA, 21–25 Mar 2010.

[O35] V. Rymanov, S. Babiel, M. Weiß, A. G. Steffan, S. Fedderwitz, L. Pavlovic, L. Naglic, A. Stöhr, and D. Jäger, "Continuous-Wave Photonic THz-Transmitter Modules employing Antenna-Integrated 1.55μm Waveguide-Photodetectors," in *International Forum on Terahertz Spectroscopy and Imaging*, Kaiserslautern, 2–3 Mar 2010.

[O36] A. Stöhr, P. Cannard, B. Charbonnier, F. van Dijk, S. Fedderwitz, D. Moodie, L. Pavlovic, L. Ponnampalam, C. C. Renaud, D. Rogers, V. Rymanov, A. J. Seeds, A. Steffan, A. Umbach, and M. Weiß, "Millimeter-Wave Photonic Components for Broadband Wireless Systems," *IEEE Transactions on Microwave Theory and Techniques*, 2010, invited, accepted.

A

Components

This annex summarizes the major applied components and test equipment used for the experiments.

ID	Component	Manufacturer & Type
AMP-1	Amplifier	Mini Circuits ZX60-14012L+
AN-1	Horn antenna	Aerowave 15-7025
AN-2	Horn antenna	Aerowave 15-7025
EAM	Electro-absorption modulator	CIP 10G-LR-EAM-1550
ECL	External cavity laser	Agilent Technologies 81680A
ED	Schottky detector	Virginia Diodes WR15 ZBD
EDFA-1	Erbium-doped fiber amplifier	IPG Photonics EAD-200-CL

EDFA-2	Erbium-doped fiber amplifier	Calmar AMP-ST15
ERD	Error detector	Anritsu MP 1764C
EPM-1	Electrical power meter	Agilent E4418B
EPM-2	V-band power sensor	Agilent V8486A
ESA-1	Electrical spectrum analyzer	Hewlett Packard 8565E
ESA-2	External mixer for ESA-1	Hewlett Packard 11970V
LNA-1	RF low noise amplifier	Terabeam HLNAV-262
LNA-2	Low noise amplifier	Miteq JSMF4-02K1500-30
LO-1	Mm-wave synthesizer	Wiltron 6769B
LO-2	Mm-wave synthesizer	Anritsu 68087B
MIX	Balanced mixer	Spacek Labs M63-6
MLLD	Mode-locked laser diode	Alcatel Thales III-V Lab IPHOBAC sample
MZM-1	Mach-Zehnder modulator	Fujitsu Limited FTM7938EZ
MZM-2	Mach-Zehnder modulator	Fujitsu Limited FTM7938EZ
OBPF	Optical band-pass filter	Tecos FC1563CQ10
OPM	Optical power meter	EXFO FPM-300
OSA	Optical spectrum analyzer	Hewlett Packard 70951B
PA-1	RF power amplifier	Terabeam HLNAV-298

PA-2	RF power amplifier	Terabeam HLNAV-250
PD	Photodetector	U2T Photonics XPDV3120R
PC-1	Polarization controller	OZ Optics HPFC-11-1300/1550
PC-2	Polarization controller	OZ Optics HPFC-11-1300/1550
PPG	Pulse pattern generator	Anritsu MP1763B
PH	Phase shifter	Aerowave 15-2310
PPG	Pulse pattern generator	Anritsu MP 1763B
SCO	Sampling oscilloscope	Agilent 86100C&86116C